MUTUALLY COUPLED SWITCHED RELUCTANCE MACHINES: FUNDAMENTALS, MODELING, AND CONTROL

MUTUALLY COUPLED SWITCHED RELUCTANCE MACHINES: FUNDAMENTALS, MODELING, AND CONTROL

BY

PETER AZER, B.Sc., M.Sc.

A THESIS

SUBMITTED TO THE DEPARTMENT OF ELECTRICAL AND COMPUTER ENGINEERING

AND THE SCHOOL OF GRADUATE STUDIES

OF MCMASTER UNIVERSITY

IN PARTIAL FULFILMENT OF THE REQUIREMENTS

FOR THE DEGREE OF

DOCTOR OF PHILOSOPHY

Doctor of Philosophy (2020)	McMaster University
(Electrical and Computer Engineering)	Hamilton, Ontario, Canada

TITLE:	Mutually Coupled Switched Reluctance Machines: Fundamentals, Modeling, and Control
AUTHOR:	Peter Azer M.Sc., (Electrical Engineering) Ain Shams University, Cairo, Egypt
SUPERVISOR:	Ali Emadi
NUMBER OF PAGES:	xxxii, 201

Abstract

Switched reluctance machines (SRMs) have gained more interest in the past decades due to their simple and robust structure. SRMs are classified into conventional SRMs (CSRMs) and mutually coupled SRMs (MCSRMs). CSRMs are based on single-phase excitation and torque is produced by the rate of change of self inductance. On the other hand, MCSRMs are based on multi-phase excitation and torque is produced by the rate of change of both self and mutual inductances. The drive system of CSRMs consists of the asymmetric half-bridge converter and the hysteresis current controller. That drive system is limiting the SRMs to be widely used since most applications are using AC motors where the standard voltage inverter and the vector control are used. Thus, in order to replace an AC motor with SRM, the converter and controller used need to be changed and not only the motor. That issue is solved in this thesis.

This thesis presents the fundamentals and operating principles of MCSRMs. A literature review of the existing modeling and control methods of MCSRMs is introduced, followed by a performance comparison for MCSRMs with different winding configurations and different control methods. After analysing the existing control and modeling methods in literature of MCSRMs, the focus of this thesis will be on MCSRMs controlled by sinusoidal currents. I preferred sinusoidal current excitation

as it enables using the standard voltage source inverter and the standard vector control with the regular modulation schemes such as sinusoidal pulse width modulation or space vector modulation.

In order to test the performance of MCSRM with sinusoidal current excitation, a dynamic model is required that can predict the phase currents and electro-magnetic torque when a given voltage is applied. Hence, a new modeling method is introduced in this thesis that is based on vector representation of motor dynamics instead of instantaneous values. The proposed modeling method reduces the size of the look-up tables and the computational steps of finite element analysis (FEA) by 50% compared to other methods. It has also the minimum error compared to other methods.

After having an accurate dynamic model, next is to apply the vector control on the MCSRM and observe the motor performance. It will be concluded in this thesis that the standard vector control could not create sinusoidal currents due to the effect of spatial harmonics. Those harmonics are due to the slotting effect of the stator and they are usually ignored in AC motors. However, they cannot be ignored in MCSRM due to the high saliency of stator and rotor poles. Thus, a simple and effective spatial harmonics compensation method is introduced to eliminate the spatial harmonics of phase currents in MCSRM.

So far we have an accurate dynamic model and we can ensure sinusoidal current excitation. The next step is how to choose the sinusoidal currents to optimize the motor performance. In order to answer that question, a comprehensive analysis of power factor, torque ripple, and efficiency of MCSRM with sinusoidal current excitation is done. That analysis is then used to optimize the motor performance in terms of power factor, efficiency, and torque ripple.

This work is dedicated to my parents, Magdy and Soad, and my brother John. Without your support and love, I would not be able to do anything.

Acknowledgements

This research was undertaken, in part, thanks to funding from the Canada Excellence Research Chairs Program and Natural Sciences and Engineering Research Council (NSERC). I would like to thank Dr. Ali Emadi for giving me the chance to be a member of his research group and the opportunity to do my Ph.D studies under his supervision.

The long meandering road of a doctorate is never possible without the support of my perfect family. I would like to thank my parents, Magdy and Soad, and my brother John for their incessant love and support. I would never achieve anything without you and the daily talks we have.

I would like to extend my profound appreciation to my committee members; Dr. Babak Nahid-Mobarakeh and Dr. Jennifer Bauman for their leadership during my research through their encouragement and the positive feedback.

I would like to thank Dr. Mehdi Narimani for giving me the chance to work with him as a teaching assistant for four semesters although I was not one of his graduate students. I also published several papers with him including my first transaction in my career, and it is the best paper I published until now. Furthermore, I would like to thank Dr. M. Marei for supervising me during my Master's study which helped me develop my skills for the Ph.D. journey.

I wish to show my gratitude to Teresa Janes, Theresa Mitchell, Paul Nguyen and Dan Manolescu for managing and coordinating the research needs.

In addition, I wish to express my deepest gratitude to Dr. Brock Howey for his unconditional and selfness help and support. I also would like to thank Dr. Alan Callegaro and Chris Mak for their help with my experimental setup. Furthermore, I would like to thank my close friends in the research group: Carin Yeghiazarian, Atriya Biswas, Sumedh Dhale, Milan Kordic, Jing Guo, Yicheng Wang, Hassan Aleian and Josh Taylor. I also want to thank my colleagues in the lab: Mohamed Ibrahim, Dr. Romina Rodriguez, Maryam Alizadeh, Niloufar Keshmiri, John Ramoul, Jacob Gareau, Deigo Valencia, Carlos Vidal, Dr. Phillip J. Kollmeyer, Jeremy Lempert, John Reimers and Jack Gillies.

I wish to express my deepest gratitude to Mina Bahaa, Rober Boshra, Ephrem Chemali, Christelle Chemali, David Nakhla and Mireille Hanna.

I want to thank my friends in my hometown in Egypt: Antwan Soliman, Ramy Maher, John Onsi, Amir Adib, Antonious Gergis, and Fady Zaki. I would like to thank Michael Adel for fixing my microphone just few hours before my defense.

I want to commemorate the cherished memory of Iman Aghabali and Mehdi Eshaghian who lost their lives in the flight crash.

Finally and above all, I would like to thank God Almighty for giving me the strength, knowledge, ability and opportunity to undertake this research study and to persevere and complete it satisfactorily. Without his blessings, this achievement would not have been possible.

Contents

List of Figures

List of Tables

Abbreviations and Symbols

Abbreviations

emf	Electromotive force
AI	Artificial intelligence
SRM	Switched Reluctance Motor
CSRM	Conventional Switched Reluctance Motor
MCSRM	Mutually Coupled Switched Reluctance Motor
SPL	Sound Pressure Level
MMF	Magnetomotive Force
N	North
S	South
SL-SP-CSRM	Single Layer - Short Pitched - CSRM
SL-SP-MCSRM	Single Layer - Short Pitched - MCSRM

DL-SP-CSRM	Double Layer - Short Pitched - CSRM
DL-SP-MCSRM	Double Layer - Short Pitched - MCSRM
SL-FP-MCSRM	Single Layer - Full Pitched - MCSRM
LCM	Least common multiple operator
LUT	Look-up tables
FEA	Finite element analysis
IPMSM	Interior permanent magnet synchronous motor
ANN	Artificial Neural Network
FF-ANN	Feedforward-Artificial Neural Network
rpm	revolution per minute
PI	proportional-integral controller
VSI	Voltage source inverter
HCC	Hysteresis current controller
SVM	Space vector modulation
SPWM	Sinusoidal pulse width modulation
RMS	Root mean square
CCC	Current chopping control
PR	proportional-resonant controller

THD	Total Harmonic Distortion
HC	Harmonic Compensation

Symbols

i_a	Phase *a* current
i_b	Phase *b* current
i_c	Phase *c* current
W_f	Field Energy
W_c	Co-energy
e	Induced emf
$d\theta$	Angular displacement
θ	Rotor position
T_e	Electro-magnetic torque
λ_a	Phase *a* flux linkage
λ_b	Phase *b* flux linkage
λ_c	Phase *c* flux linkage
L_a	Self inductance of phase *a*
L_b	Self inductance of phase *b*

L_c	Self inductance of phase c
M_{ab}	Mutual inductance between phases a and b
M_{ac}	Mutual inductance between phases a and c
M_{bc}	Mutual inductance between phases b and c
N_s	Number of stator poles
N_r	Number of rotor poles
m	Number of phases
λ_{phase}	Phase flux linkage
i_{phase}	Phase current
v_{phase}	Phase voltage
R	Phase resistance
L	Self inductance
L_n	Cosine Fourier coefficients of self inductance
n	Harmonic order
L_0	DC Fourier coefficient of self inductance
L_1	First order Fourier coefficient of self inductance
L_2	Second order Fourier coefficient for the $n^{th} order$ of self inductance
M	Mutual inductance

M_n	Cosine Fourier coefficient for the n^{th} order harmonic of mutual inductance
i_x, i_y	Currents of two excited phases
R_{sc}	Stator core reluctance
R_{rc}	Rotor core reluctance
R_{sp}	Stator pole reluctance
R_{rp}	rotor pole reluctance
R_g	Air gap reluctance
i_d	Direct-axis current
i_q	Quadrature-axis current
λ_d	Direct-axis flux linkage
λ_q	Quadrature-axis flux linkage
a_1, a_2	Subphases of phase a
b_1, b_2	Subphases of phase b
c_1, c_2	Subphases of phase c
λ	Flux linkage
i	current
λ_u	Phase u flux linkage

λ_v	Phase v flux linkage
λ_w	Phase w flux linkage
i_u	Phase u current
i_v	Phase v current
i_w	Phase w current
w	Angular frequency
I_m	Peak value of phase current
I_o	DC Fourier coefficient of phase current
I_{an}	Cosine Fourier coefficient for the n^{th} order harmonic of phase current
I_{bn}	Sine Fourier coefficient for the n^{th} order harmonic of phase current
I_n	Magnitude of the n^{th} order harmonic of phase current
ϕ_n	Angle of the n^{th} order harmonic of phase current
T_{avg}	Average value of the electro-magnetic torque
T_{an}	Cosine Fourier coefficient for the n^{th} order harmonic of electro-magnetic torque
T_{bn}	Sine Fourier coefficient for the n^{th} order harmonic of electro-magnetic torque
$i_{d,an}$	Cosine Fourier coefficient for the n^{th} order harmonic of d-axis current

$i_{d,bn}$	Sine Fourier coefficient for the n^{th} order harmonic of d-axis current
$i_{q,an}$	Cosine Fourier coefficient for the n^{th} order harmonic of q-axis current
$i_{q,bn}$	Sine Fourier coefficient for the n^{th} order harmonic of q-axis current
p	Motor pole pair
k_p	PI controller proportional gain
k_i	PI controller integral gain
v_d	Direct-axis voltage
v_q	Quadrature-axis voltage
P	Real power
Q	Reactive power
$cos(\phi)$	Power factor
θ_{on}	Turn on angle of phase current control
θ_{off}	Turn off angle of phase current control
L_d	Direct-axis inductance
L_q	Quadrature-axis inductance
λ_o	DC value of phase flux linkage
λ_{an}	Cosine Fourier coefficient for the n^{th} order harmonic of phase flux linkage

λ_{bn}	Sine Fourier coefficient for the n^{th} order harmonic of phase flux linkage
V_m	Peak value of phase voltage
V_o	DC Fourier coefficient of the phase voltage
V_{an}	Cosine Fourier coefficient for the n^{th} order harmonic of phase voltage
V_{bn}	Sine Fourier coefficient for the n^{th} order harmonic of phase voltage
$\Delta\theta$	Incremental change of rotor position at constant speed
T_s	Sample time
t_k	time instant k
v_α	alpha-axis voltage
v_β	beta-axis voltage
v_{u1}	Fundamental component of phase u voltage
v_{do}	DC Fourier coefficient of direct-axis voltage
v_{qo}	DC Fourier coefficient of quadrature-axis voltage
λ_{do}	DC Fourier coefficient of direct-axis flux linkage
λ_{qo}	DC Fourier coefficient of quadrature-axis flux linkage
$v^*_{u,v,w}$	Reference 3-phase voltages
$v^*_{\alpha,\beta}$	Reference alpha-and beta-axis voltages

i_d^*, i_q^*	Reference direct-axis and quadrature-axis currents
N_{rpm}	Motor speed in revolution per second
f_{bw}	Bandwidth frequency
θ_{dq}	Excitation angle of phase current
I_{ph}	Current phasor in space
i_P	Current component responsible for real power
i_Q	Current component responsible for reactive power
T_{6rated}	The rated 6^{th} order torque harmonic
v_{dc}	DC-link voltage
T_{ref}	Reference torque command
α	weighting coefficient of phase current magnitude
β	weighting coefficient of torque ripple T_6
γ	weighting coefficient of power factor
η	Motor efficiency

Chapter 1

Introduction

1.1 Mutually Coupled Switched Reluctance Machines

Switched reluctance machines (SRMs) are firstly introduced by Ray, Davis and Lawrenson in years 1979 and 1980 by using single-phase excitation as an extension of stepper motors [1,2]. Early work and studies used to refer to SRM as the variable reluctance stepper motor because they share the same operating principles of single-phase excitation and the minimum reluctance path in torque production [3–6]. SRMs are characterized by their simple and robust structure among other electric motors due to the absence of windings and magnets from the rotor. Rotor magnets used in synchronous motors are rare-earth elements and they consume around 53% of the motor cost. Rotor windings used in induction motor are costly as well. Thus, the advantage of SRMs over other motors is the lower cost machine due to absence of rotor windings and magnets. However, they suffer from poor performance in terms of torque ripple and acoustic noise. In the past few decades, SRMs have been gaining more attention due to the advancements in power electronics that enable the use of complicated control strategies to improve the performance of SRMs [7,8].

Barrie Mecrow tried to improve the performance of SRMs using multi-phase excitation for four phase 8/6 SRM where two phases were excited simultaneously instead of the common known single-phase excitation, with a fully pitched windings configuration instead of the common known short pitched windings. Mecrow referred to his motor as the mutually coupled SRMs (MCSRMs), because the mutual inductance contributes significantly in the torque production and to distinguish between his motor and the standard SRM that is then referred to as the conventional SRMs

(CSRMs). Mecrow trial of multi-phase excitation is extended to include unipolar and bipolar rectangular current excitation with different conduction periods trying to find the best performance of the MCSRMs.

The MCSRMs with rectangular current excitation could not compete with AC motors that are widely used and controlled by sinusoidal currents, as the performance of AC motors (in terms of efficiency and torque quality) and control (in terms of using the standard vector control) are better and more flexible than MCSRMs. As a result, most of the focus in the past decades was on CSRMs with the single-phase excitation and MCSRMs and work on MCSRMs is relatively stagnated. The performance of CSRMs is significantly improved with the current shaping techniques at low speeds when the motor speed is less than the base speed, where the current waveform is shaped in a way to improve the torque quality, acoustic noise and efficiency. That improvement lead the researchers believe that CSRMs can compete with the permanent magnet synchronous motors (PMSMs) and induction motors (IMs).

In current shaping techniques, a unique current profile is defined for each operating point where each operating point has a different current waveform than the other operating points. Those current profiles are saved as instantaneous values with respect to rotor position in a micro-controller that requires a large memory to define the current waveform at each operating point. On the other hand, AC motors are controlled by sinusoidal currents where the current profile at any operating point is defined as a vector in terms of direct-and quadrature-axis currents. Additionally, the drive system of CSRMs consists of the hysteresis current controller (HCC) and the asymmetric half-bridge converter to provide independent phase current control [9–12]. Hysteresis current controller (HCC) is the common current control method for SRMs with advantages such as fast transient response, simple implementation, and is robust to load variations. However, HCC requires high variable switching frequency to achieve lower current ripple. The variable switching frequency of HCC can also cause acoustic noise and adds difficulty in designing the electro-magnetic interference (EMI) filter [13]. The HCC and asymmetric half-bridge converter are limiting SRMs to be widely used in several application as the drive system of AC motors (which dominate the market and are widely used in many applications) consists of the standard voltage source inverter and vector control. Thus, in order to replace an AC motor with SRM, the converter and the control system need to be changed in addition to the motor. Although SRMs has lower cost compared to AC motors as I mentioned before, the unpopular drive system of SRMs has higher cost than the drive system of AC motors. Based on that, the perfect scenario to solve the high cost issue of the drive system of SRM is to control it using the same drive system of AC motors. Thus, the MCSRM will be controlled with 3-phase sinusoidal current to merge the advantages of AC motors in terms of motor control with the advantages of SRMs in terms of the simple and robust structure. The sinusoidal current excitation enables to consider the MCSRM as an AC motor where the AC motor drive system can be used such as the standard voltage source inverter (VSI) and the standard vector control with regular modulation schemes such as space vector modulation or sinusoidal pulse width modulation. Hence, the issues of the unique current waveform, the odd converter used, and the hysteresis current controller are solved.

The modeling of MCSRMs with 3-phase excitation is more complicated than the single-phase excitation. Besides, the salient structure of stator and rotor poles of SRM introduces a significant harmonics in the current waveform known by the spatial harmonics. Spatial harmonics are due to the mechanical structure unlike the time harmonics that are due to non-linear load. Spatial harmonics also exist in AC motors due to the slotting effect, however, they are usually ignored. In SRMs, stator and rotor have salient poles not slots, and those salient poles are the main source for torque production as will be explained in the next chapter. Hence, the standard vector control of AC motors cannot handle the spatial harmonics in MCSRMs. The difficulties in modeling and controlling the MCSRMs will be addressed and solved in this thesis.

1.2 Objectives and Contributions

The main objective of this thesis is to control the SRM with sinusoidal current excitation and consider it as one of the AC motors, so that we can use the same drive systems of AC motors. By doing that, we will use low cost motor and low cost motor drive. The problems associated with the sinusoidal current control of MCSRMs will be discussed and solved in details. Hence, there are four main contributions introduced:

1. A comprehensive analysis and performance comparison of the existing modeling methods and control methods that have been introduced before to MCSRMs.

2. A new dynamic modeling method is introduced, which reduces the size of the look-up tables (LUTs) and the computational steps of finite element analysis (FEA) by 50% compared to the existing modeling methods.

3. A spatial harmonics compensation method is introduced that eliminates the spatial harmonics of the current waveform without the need to use extra devices

or complex algorithms.

4. A comprehensive analysis of torque ripple and power factor of MCSRMs with sinusoidal current excitation is introduced. That analysis is used to develop an optimized control method that aims to reduce torque ripple, copper losses, and to improve the power factor.

The mechanical aspects in terms of mechanical design, mechanical vibrations, and acoustic noise will not be discussed in this thesis.

1.3 Summary of Thesis

In chapter 2, the fundamentals of MCSRM including the possible poles and windings configuration that can be used in MCSRMs are introduced. A detailed review of the existing control and modeling methods is presented in chapter 3 and chapter 4, respectively. Modeling methods of MCSRM are analytical methods such as the inductance and magnetic circuit modeling, or LUTs based models, which are more accurate. In LUTs based methods, the used LUTs and the simulated currents in the FEA model represent two quadrants of the dq frame. In chapter 5, that method is improved so that the simulated currents in the FEA model represent only a single quadrant in the dq frame. Therefore, the number of FEA steps and the size of the LUTs are reduced by 50%. The proposed method is validated by both FEA and experiments.

In chapter 6, a spatial harmonics compensation method is introduced, which calculates the required voltage harmonics to ensure sinusoidal current excitation without using additional proportional-integral (PI) and proportional-resonant (PR) controllers or extra devices. The proposed method is validated by both simulation and experimental results.

After ensuring sinusoidal current excitation through the proposed harmonic compensation method, defining the optimum operating point is introduced in chapter 7. The optimized control aims to reduce torque ripple and to increase the power factor and average torque.

Chapter 8 concludes the thesis and discusses the future work for further improvements in MCSRMs' performance.

Chapter 2

Mutually Coupled Switched Reluctance Machine (SRM): Fundamentals and Applications

2.1 Introduction

In this chapter, the fundamentals of SRMs are presented and the differences between CSRMs and MCSRMs are explained. The fundamentals include the operating concept, windings configuration, and pole configuration for both CSRMs and MCSRMs.

2.2 Operating Concept

Torque production in SRM is due to the tendency of the generated magnetic flux to have a minimum reluctance path, which in return rotates the rotor until the rotor pole becomes aligned with the excited stator pole, maximizing the inductance of the excited phase.

Considering a single phase SRM shown in figure 2.1(a) and for a linear magnetic system shown in figure 2.1(b) (i.e., inductance does not change with current) half of the input electrical energy is stored in the magnetic circuit, which is known as the field energy. The lower half is converted to mechanical energy and it is responsible for torque production. It is known as the co-energy. Equation (2.2.1) describes the energy conversion dynamics:

$$e i_a dt = dW_f + T_e d\theta \tag{2.2.1}$$

where i_a is phase a current, W_f is the field energy transferred between the source and the magnetic circuit, and is equivalent to reactive power, and T_e is the electromagnetic torque responsible for angular displacement, $d\theta$. e is the induced emf and

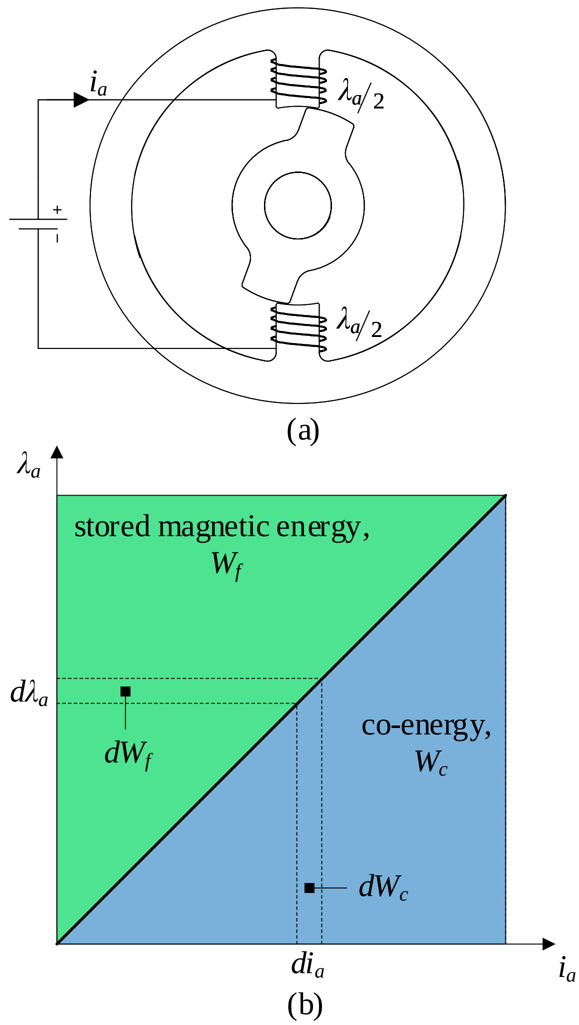

Figure 2.1: (a) single phase SRM, (b) flux linkage versus current for a linear magnetic system.

its magnitude is expressed by Faraday's law:

$$e = \frac{d\lambda_a}{dt} \tag{2.2.2}$$

where λ_a is phase a flux linkage. Using equation (2.2.2), equation (2.2.1) can be formulated as:

$$i_a d\lambda_a = dW_f + T_e d\theta \tag{2.2.3}$$

From figure 2.1(b), the summation of field energy and co-energy is:

$$\lambda_a i_a = W_c + W_f \tag{2.2.4}$$

$$d(\lambda_a i_a) = \lambda_a di_a + i_a d\lambda_a = dW_c + dW_f \tag{2.2.5}$$

From equation (2.2.3) and equation (2.2.5), co-energy can be formulated as:

$$dW_c = \lambda_a di_a + T_e d\theta \tag{2.2.6}$$

Co-energy is a function of current and rotor position. Hence, the partial derivatives of co-energy is equal to:

$$dW_c = \frac{\partial W_c}{\partial \theta}\mathrm{d}\theta\bigg|_{i_a=const} + \frac{\partial W_c}{\partial i_a}\mathrm{d}i_a\bigg|_{\theta=const} \tag{2.2.7}$$

Comparing equation (2.2.6) and equation (2.2.7), flux linkage and torque expressions can be calculated as:

$$\lambda_a = \frac{\partial W_c}{\partial i_a}\bigg|_{\theta=const}, \; T_e = \frac{\partial W_c}{\partial \theta}\bigg|_{i_a=const} \tag{2.2.8}$$

For a linear magnetic circuit shown in figure 2.1(b), co-energy is half of the input electrical energy:

$$W_c = \frac{1}{2}\lambda_a i_a \tag{2.2.9}$$

Assuming two phases are excited simultaneously (phases a and b), co-energy can be expressed as:

$$W_c = \frac{1}{2}\lambda_a(\theta, i_a, i_b)\; i_a + \frac{1}{2}\lambda_b(\theta, i_a, i_b)\; i_b \tag{2.2.10}$$

where i_b and λ_b are phase b current and flux linkage, respectively. Flux linkages include self and mutual inductances and are functions of phase currents and rotor position:

$$\lambda_a(\theta, i_a, i_b) = i_a L_a + i_b M_{ab}, \tag{2.2.11a}$$

$$\lambda_b(\theta, i_a, i_b) = i_b L_b + i_a M_{ab} \tag{2.2.11b}$$

where L_a, L_b and M_{ab} are self inductance of phase a, self inductance of phase b and mutual inductance between phases a and b, respectively. Substituting equation (2.2.11) into equation (2.2.10) results in:

$$W_c = \frac{1}{2}(L_a i_a^2 + L_b i_b^2 + 2 i_a i_b M_{ab}) \tag{2.2.12}$$

Therefore, electro-magnetic torque equals to:

$$T_e = \left.\frac{\partial W_c}{\partial \theta}\right|_{i=const} = \frac{1}{2} i_a^2 \frac{dL_a}{d\theta} + \frac{1}{2} i_b^2 \frac{dL_b}{d\theta} + i_a i_b \frac{dM_{ab}}{d\theta} \tag{2.2.13}$$

Similarly, for 3-phase excitation (phases a, b, and c) the torque equation is expressed as:

$$\begin{aligned} T_e = {} & \frac{1}{2} i_a^2 \frac{dL_a}{d\theta} + \frac{1}{2} i_b^2 \frac{dL_b}{d\theta} + \frac{1}{2} i_c^2 \frac{dL_c}{d\theta} \\ & + i_a i_b \frac{dM_{ab}}{d\theta} + i_a i_c \frac{dM_{ac}}{d\theta} + i_b i_c \frac{dM_{bc}}{d\theta} \end{aligned} \tag{2.2.14}$$

where L_c, M_{ac} and M_{bc} are phase c self inductance, mutual inductance between phases a and c, and mutual inductance between phases b and c, respectively. For CSRM where mutual coupling between phases is ignored, $M_{ab} = M_{bc} = M_{ac} = 0$. Based on equation (2.2.14), torque developed due to self inductance is dependent on the slope of the inductance profile and independent of the direction of current, similar to CSRM. While torque developed due to mutual coupling is dependent on both the direction of current and slope of the inductance.

2.2.1 Pole Configuration

Number of stator and rotor poles in MCSRM is selected to achieve balanced operation for a given number of phases. This means that stator poles which belong to the same phase should have the same electrical angle at any rotor position. In light of that, equation (2.2.15) explains the relationship between the number of stator poles, number of rotor poles and number of phases to achieve a balanced operation [1]:

$$LCM(N_s, N_r) = mN_r \tag{2.2.15}$$

where LCM represents the least common multiple operator, N_s is the number of stator poles, N_r is the number of rotor poles, and m is the number of phases. It is worth mentioning that number of stator poles per phase is always an integer number for SRMs.

2.2.2 Winding Configuration

Concentrated winding is widely utilized in SRMs, where the coils are concentrated in one slot. As CSRM has single-phase excitation, the concentrated winding provides the highest magnetomotive force (MMF) to maximize the generated electro-magnetic torque [3, 6, 14–16].

Single Layer Short Pitched SRM [17–21]

A stator slot in single layer windings has one phase coil and it is not shared by other phase coils. So, the number of coils is half of the number of stator poles. The angular displacement between poles is 180° electrical, and it is called pole span or pole pitch. If the coil span is less than the pole span (180° electrical), then it is called a short pitched winding as shown in figure 2.2(a).

Single layer short pitched winding can be CSRM or MCSRM. In CSRM, each two consequent stator poles of the same phase has different polarities. These poles create a single flux path. Therefore, the magnetic flux path in CSRM is within the stator poles of the excited phase only and negligible flux flows through the stator poles of

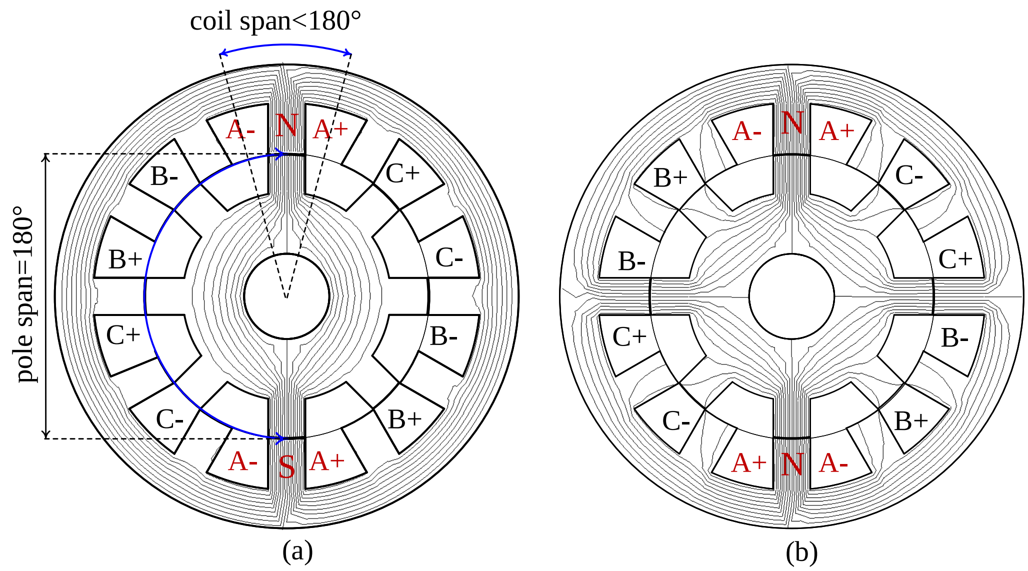

Figure 2.2: Winding configuration of 3-phase 12/8 SRM and flux distribution when phase a is excited (a) single layer short pitched CSRM, (b) single layer short pitched MCSRM.

an unexcited phase. This can be seen in figure 2.2(a). The consequent stator poles of phase a have different polarities of North (N) and South (S). All flux paths are through the excited phase a poles and there is almost no flux paths within the poles of the other phases. This is why the mutual coupling in CSRM can be ignored.

In MCSRM, to enhance the mutual coupling between phases, the stator poles of the same phase have the same polarity. Thus, flux generated by one phase have flux paths through the poles of the other phases. As it can be seen from figure 2.2(b), the flux generated by the excited phase a have flux paths through other phases which creates mutual coupling between phases.

Equation (2.2.15) can result in odd number of stator poles, for instance, 9/12 3-phase SRM. The odd number of stator poles is only valid for MCSRM as CSRM requires even number of stator poles [22], so that each two consequent stator poles provide one flux path.

Double Layer Short Pitched SRM [17–19, 21, 23, 24]

The difference between the double layer short pitched winding with that of single layer one is that two coils of different phases share the same slot in the double layer winding. Thus, the number of coils is equal to the number of stator poles. Similar to single layer short pitched winding, double layer short pitched winding can be CSRM or MCSRM.

figure 2.3(c) and figure 2.3(d) show the winding diagrams for double layer short pitched 12/8 CSRM (DL-SP-CSRM) and MCSRM (DL-SP-MCSRM), respectively. The flux paths are also shown when phase a is excited. It can be observed that the polarity of the coils define whether the motor is a CSRM or MCSRM. As shown in figure 2.3(d), the coils of the same phase in MCSRM have the same polarity. Therefore, the magnetic path is through the poles of the other phases, enhancing the mutual coupling. As shown in figure 2.3(c), the coils of the same phase in CSRM have opposite poles. Therefore, the flux paths only use the stator poles of phase a.

Single Layer Full Pitched SRM [16, 19, 21, 25–30]

In full pitched winding, the coil span is equal to pole span (180° electrical). Figure 2.4(e) shows single layer full pitched 12/8 MCSRM (SL-FP-MCSRM). In a full pitched configuration, single-phase excitation is not enough to magnetize any stator pole. Therefore, at least two phases should be excited simultaneously. This is why single layer full pitched winding can only work as a MCSRM.

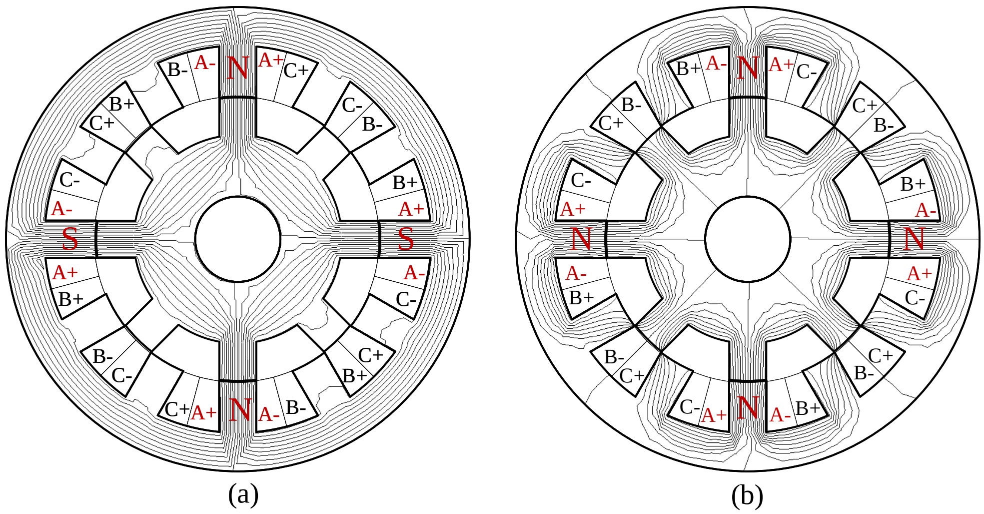

Figure 2.3: Winding configuration of 3-phase 12/8 SRM and flux distribution when phase a is excited (c) double layer short pitched CSRM, (d) double layer short pitched MCSRM.

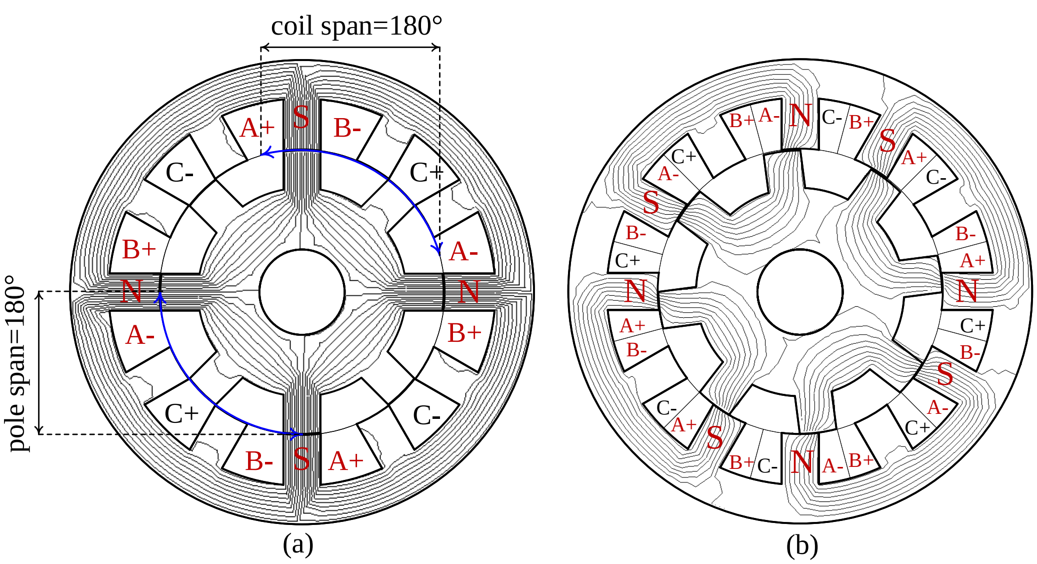

Figure 2.4: Winding configuration of 3-phase 12/8 SRM and flux distribution when phase a is excited (e) single layer full pitched MCSRM, (f) double layer fractional pitched MCSRM.

Double Layer Fractional Pitched SRM [31]

The fractional pitched winding is similar to the short pitched winding but with different coil span as shown in figure 2.4(f). This winding configuration is not commonly applied. The single layer full pitch winding that was described earlier, provides constant self inductance when applied to MCSRM. Hence, torque production relies on the variation of the mutual inductance only [16]. On the other hand, the double layer fractional pitched winding can utilize both self and mutual inductance in torque production [31].

2.3 Applications

Technically, the MCSRM can replace any AC motor since the MCSRM controlled by sinusoidal currents utilizes the standard voltage source inverter (VSI) and the standard vector control with the conventional modulation methods such as Space Vector Modulation (SVM) and the Sinusoidal Pulse Width Modulation (SPWM). However, most of MCSRM designs are for traction applications such as electric vehicles [30, 32, 33] or electric bikes [34].

SRMs are also considered as a good candidate for the applications where noise or torque ripple are not an important factor to consider. For example, we all know that noise or sound waves in general require a medium to transfer. Thus, SRMs will not generate noise in space due to the absence of the medium such as air or water. On the other hand, SRMs can be also used in noisy environments where the noise from the SRMs become negligible. For instance, SRMs can be used by digging equipments in construction sites, or by electrified war tanks.

2.4 Summary

SRMs are classified into conventional SRMs (CSRMs) and mutually coupled SRMs (MCSRMs). CSRMs are based on single-phase excitation and torque is produced by the rate of change of self inductance. In CSRM, the commutation happens when two phases have current at the same time. That overlapping occurs when one phase is excited while the other phase is not fully demagnetized. The mutual coupling during commutation is usually negligible in CSRM. This is because the winding configuration in SRM minimizes the mutual flux path and the phase currents are small during commutation. MCSRMs are based on multi-phase excitation and torque is produced by the rate of change of both self and mutual inductances. SRMs which have odd number of stator poles can only operate as MCSRM. Winding configurations of MCSRM can be single layer short pitched, double layer short pitched, double layer fractional pitched, and single layer full pitched. The single layer full pitched SRM can only operate as MCSRM, as at least two phases are needed to be excited to magnetize a single stator pole.

Chapter 3

Current Waveforms and Control Methods for Mutually Coupled SRMs

3.1 Introduction

The standard current waveform of CSRMs is unipolar rectangular waveform. In order to improve the performance of CSRMs, advanced control techniques, such as current profile shaping, are applied to reduce the torque ripple and acoustic noise [35–38]. On the other hand, current waveform of MCSRMs can be unipolar rectangular waveforms, bipolar rectangular waveforms or sine waveform [20, 21, 26].

In electric motors, the motor speed is regulated by controlling the electro-magnetic torque, which is controlled through the phase currents. Current control in MCSRMs can be classified into dependent phase current control where the phase currents are related together and independent phase current control where the phase currents are not related in any way. Section 3.2 presents the dependent phase current control methods, section 3.3 introduces the independent phase current control methods, and section 3.5 presents the summary of the chapter.

3.2 Dependent Phase Current Control

Dependent phase current control is referred to the case when the sum of phase currents at any time instant is zero. In this control strategy, MCSRM can be considered as an AC motor where the standard voltage source inverter (VSI) shown in figure 3.1 can be used. Phase current can be any waveform, such as sinusoidal or bipolar rectangular (alternating between positive and negative half cycles) so that the sum of the phase currents is zero.

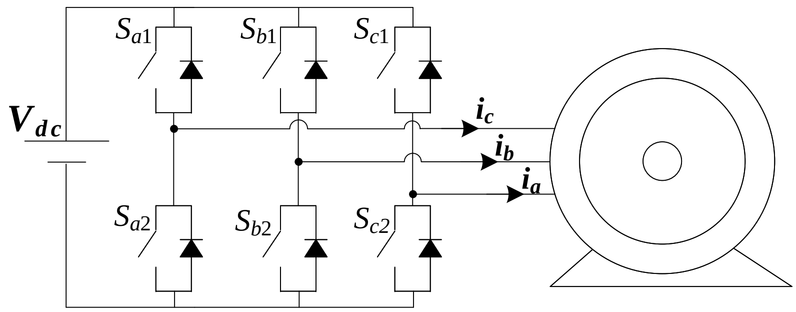

Figure 3.1: 2-level voltage source inverter for dependent phase current control.

Sinusoidal Current Excitation [17–19, 21, 30, 39, 40]

Figure 3.2(a) shows 3-phase sinusoidal currents, which is the most common way for motor control. The system parameters for sinusoidal excitation can be calculated as [41]:

$$T_{avg} = \frac{3}{2}p(\lambda_d i_q - \lambda_q i_d) \tag{3.2.1}$$

$$v_d = i_d R - \lambda_q w \tag{3.2.2}$$

$$v_q = i_q R + \lambda_d w \tag{3.2.3}$$

$$P = \frac{3}{2}(v_d i_d + v_q i_q) \tag{3.2.4}$$

$$Q = \frac{3}{2}(v_q i_d - v_d i_q) \tag{3.2.5}$$

$$cos(\phi) = \frac{P}{\sqrt{P^2 + Q^2}} \tag{3.2.6}$$

where T_{avg} is the output average torque, w is the electrical angular frequency, p is the number of pole pairs and is equal to half of the number of rotor poles. λ_d and λ_q are dq components of phase flux linkage, v_d and v_q are the dq components of the phase voltage, and i_d and i_q are the dq components of the phase current. R is the phase resistance, and P and Q are active and reactive power, respectively. $cos(\phi)$ is the power factor of the three-phase load.

Equation (3.2.1) to equation (3.2.6) describe the average torque calculation, active power, reactive power, and power factor. Sinusoidal current control is the only control method that provides these direct formulas for system parameters calculation, which is an advantage. Another advantage of the sinusoidal current excitation is that the vector control (dq-current control) can be applied with space vector modulation (SVM) or sinusoidal pulse width modulation (SPWM) like in AC motors. Thus, there is no need to use hysteresis current controller (HCC) which is commonly used in CSRMs. HCC has the advantages of fast dynamic response, maximum current limitation, and simple implementation. Since the sum of phase currents is zero in a balanced 3-phase system (referred as inter-phase dependency), a major drawback of HCC is the high switching frequency operation as each phase is controlled separately without the coordination with other phases [45–47]. The inter-phase dependency is considered in SVM since the 3-phase currents are controlled by one vector representing the line voltage. Additional advantage of the sinusoidal current control, MCSRM has better performance than CSRM regarding vibration and acoustic noise. Authors in [48] have shown that the 3-phase 6/4 MCSRM has radial forces half that of 6/4 CSRM for the same output torque. In [17], it was demonstrated that the 3-phase 12/8 MCSRM has lower vibration and lower sound pressure level (SPL) than the the 3-phase 12/8 CSRM, when both motors have the same geometry and are supplied by the same sinusoidal current.

Four Quadrants Operation: Motor control by 3-phase sinusoidal currents is classified into scalar control and vector control. In scalar control, only the magnitude

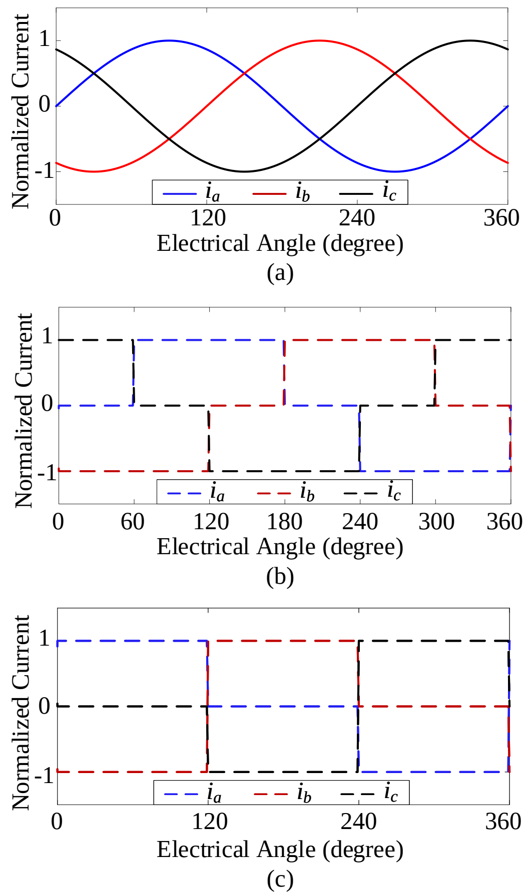

Figure 3.2: Dependent phase current control (a) Sinusoidal current excitation, symmetric bipolar current (b) 240° conduction period [16, 18, 26, 27, 40, 42–44] (60° zero current + 120° positive current + 60° zero current + 120° negative current), (c) 240° conduction period [18, 20, 31] (120° positive current + 120° zero current + 120° negative current).

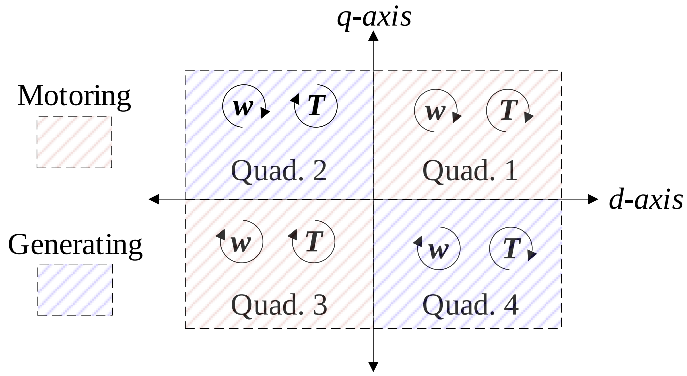

Figure 3.3: The four quadrants operation in the dq frame

of phase voltage and phase current are controlled as scalar values. While in vector control, phase voltage and phase current are considered as vector quantities which have a magnitude and an angle. The magnitude and the angle of that vector is defined by d-axis and q- axis components as:

$$X_m = \sqrt{{x_d}^2 + {x_q}^2} \tag{3.2.7a}$$

$$\theta_{dq} = tan^{-1}\left(\frac{x_q}{x_d}\right) \tag{3.2.7b}$$

where x_d and x_q are the d-axis and q-axis components, X_m is the vector magnitude and θ_{dq} is angle of the vector. The d-axis and q-axis define the dq rotating frame where there are four quadrants of operation based on torque and speed directions of the motor. Figure 3.3 shows the operation at the four dq quadrants; the dq quadrant is defined as motoring mode of operation when torque and speed directions are similar, while it is defined as generating mode of operation when torque and speed have different directions. Thus, there are two quadrants correspond to the motoring mode which are the first and third quadrants, and the other two quadrants correspond to the generating mode which are the second and fourth quadrants. In generating

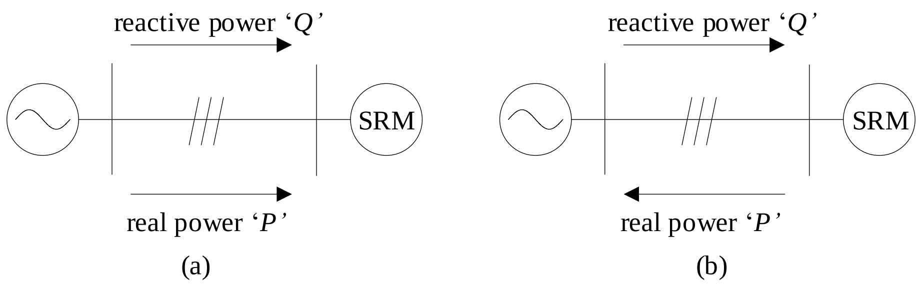

Figure 3.4: Real power flow and reactive power flow directions: (a) motoring mode, (b) generating mode

mode, the SRM has an input of mechanical power and outputs real power to the electrical source, and in motoring mode, the SRM has an input of real power and outputs mechanical power. Since SRMs have no source for reactive power such as field windings or magnets, SRMs always consume reactive power from the electrical source in either motoring mode or generating mode. Figure 3.4 shows the real power flow and reactive power flow directions at generating and motoring modes.

Symmetric Bipolar Current Excitation [16, 18, 20, 23, 26, 27, 31, 40, 42]

Bipolar current excitation is when the current waveform alternates between the positive and negative half cycles. Figure 3.2(b) and figure 3.2(c) show two rectangular current waveforms where the sum of the instantaneous values of the phase currents is zero. Usually two phases are excited simultaneously; one phase current has positive magnitude and the other phase current has the same magnitude, but with negative polarity. The phase shift between phase currents is $360/m$ (m is the number of phases), which is 120° electrical for a 3-phase MCSRM. HCC is usually used in symmetric bipolar excitation to regulate the current.

3.3 Independent Phase Current Control

In the independent phase current control, the sum of the instantaneous values of the phase currents is not zero and, hence, the standard VSI cannot be used. If phase currents are unipolar, then an asymmetric half bridge converter is used to control each phase separately as shown in figure 3.5(a) [7, 8]. If phase currents are bipolar, then a single-phase full bridge inverter is used for each phase as shown in figure 3.5(b) [49]. As phase currents are not sinusoidal, SVM and SPWM cannot be used and HCC is usually utilized to control the current. The single-phase full bridge inverter can also be used for dependent current control to increase the motor drive reliability since the number of legs of the full-bridge converter is double the number of legs of the VSI. However, this will increase the cost and volume of the motor drive. In this thesis, we will use the VSI similar to AC drive systems.

Unipolar Current Excitation

Unipolar current excitation in MCSRM is similar to CSRM, but the conduction period is increased to provide overlapping between phase currents. For instance, conduction period for a 3-phase MCSRM is larger than 120° electrical. Figure 3.6(a) shows unipolar current excitation for 180° electrical conduction period [20, 42] and figure 3.6(b) shows unipolar current excitation for 240° electrical conduction period [16, 26, 27, 32, 42, 50] for a 3-phase MCSRM.

Non-symmetric Bipolar Current Excitation

Non-symmetric bipolar phase current is when the positive and negative current half cycles are not identical. Non-symmetric bipolar current excitation is introduced

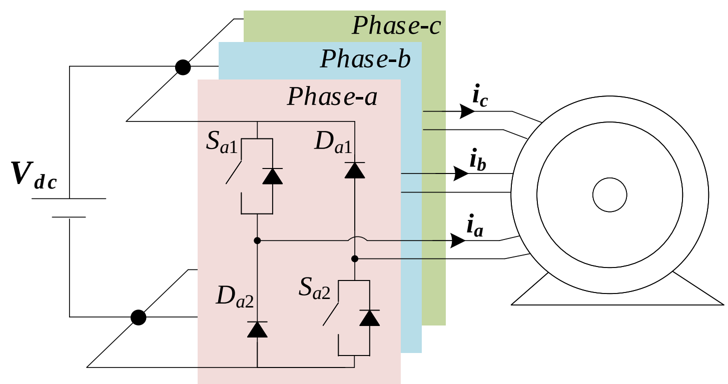

(a)

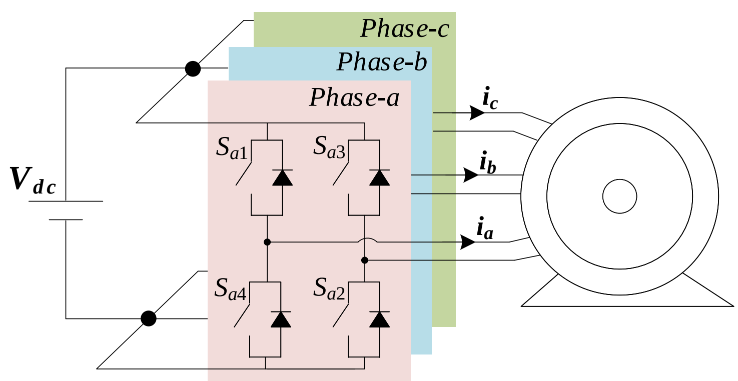

(b)

Figure 3.5: Converters used for independent phase current control (a) Asymmetric half-bridge converter for unipolar excitation, (b) Symmetric full-bridge converter for bipolar excitation.

in [18, 20, 51], and [52] to increase the torque generated from mutual inductance. Figure 3.7(a) and figure 3.7(b) show current waveforms for a 3-phase MCSRM for 180° [20, 51, 52] and 360° [18] electrical conduction periods, respectively.

Symmetric Bipolar Current Excitation [16, 26, 42]

The conduction period is the main difference between the symmetric bipolar excitation for independent phase current control and for dependent phase current control discussed in section 3.2. The symmetric current in dependent phase control has

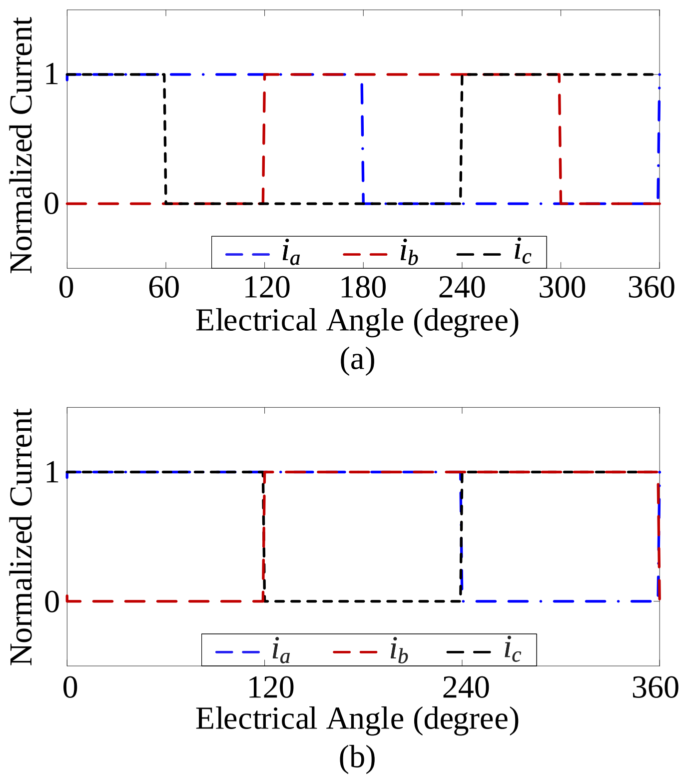

Figure 3.6: Independent phase current control: Unipolar current excitation of (a) 180° conduction period (180° positive current + 180° zero current), (b) 240° conduction period (240° positive current + 120° zero current).

a conduction period of 240° electrical (see figure 3.2(b)), while the bipolar current for independent control has a conduction period of 360° electrical as shown in figure 3.7(c).

It should be noted that the currents shown in figure 3.2, figure 3.6, and figure 3.7 (except for the sinusoidal current) are applicable only at low speed operation, generally when the motor speed is lower than the base speed. When the motor speed is higher than the base speed, the phase current has a different waveform at different operating speeds. For instance, figure 3.8 shows unipolar current excitation waveforms at low speed and high speed operation. It can be seen from figure 3.8 that, at

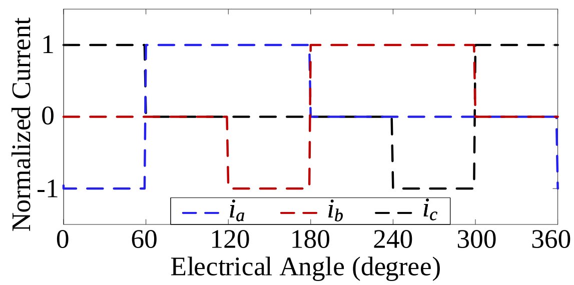

(a)

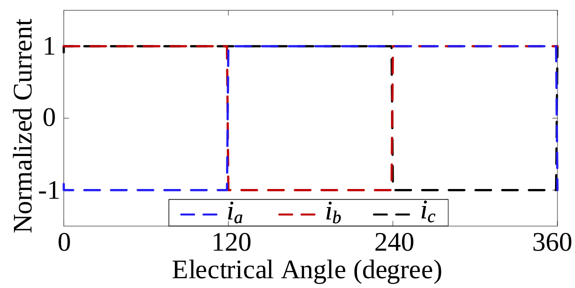

(b)

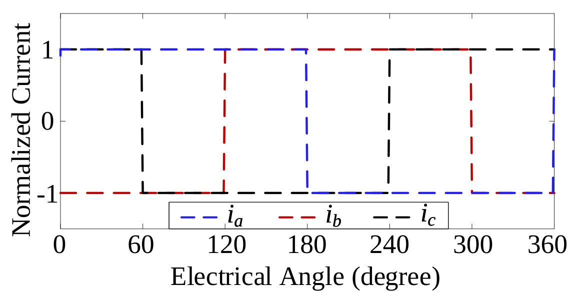

(c)

Figure 3.7: Independent phase current control: Non-symmetric bipolar current excitation of (a) 180° conduction period (60° negative current + 120° positive current + 180° zero current), (b) 360° conduction period (120° negative current + 240° positive current), (c) symmetric bipolar current excitation for 360° conduction period (180° positive current + 180° negative current).

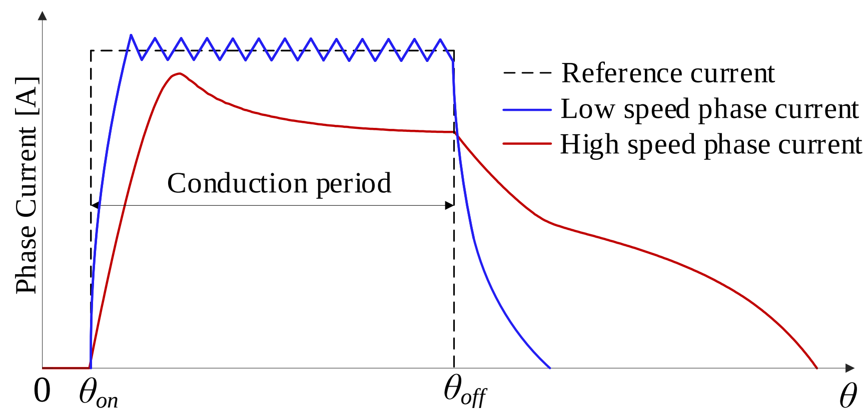

Figure 3.8: Unipolar current excitation at low speed operation where current control is applicable and high speed operation where current control is not applicable.

low speed, the phase current waveform reaches the reference value where switching action takes place. This is defined as current chopping control (CCC) which results in a phase current waveform close to the rectangular waveform. At high speed (i.e., when motor speed exceeds the base speed), the induced emf is higher than the DC link voltage. Thus, phase current might not reach the reference value. This is defined as the single pulse control where a duty ratio of one is applied to the switching device (phase voltage is equal to the DC link voltage). When the rotor position reaches θ_{off}, the duty cycle is zero (phase voltage is equal to the negative DC link voltage). At high speed operation, when current control is not available, different motor speeds result in different values of induced emf, which in turn creates different phase current waveforms. The same issue also exists in CSRMs.

Sinusoidal phase currents do not have the high rate-of-change as in the rectangular waveforms shown in figure 3.2, figure 3.6, and figure 3.7. Therefore, the current waveform can be maintained as sinusoidal or close to sinusoidal even at high speeds [53, 54]. This is another advantage for sinusoidal excitation.

Table 3.1: Motor Specifications

Stator pole number	12	Number of turns per phase	132
Rotor pole number	8	Stator outer diameter	90
Phase number	3	Rotor outer diameter	53
Rated RMS current (A)	10	Rotor inner diameter	31.4
Current density (A_{rms}/mm^2)	5.68	Air-gap length (mm)	0.5
Active length (mm)	60		

3.4 Performance Comparison

In this section, a performance comparison for different winding configurations for a 3-phase 12/8 MCSRM with different control methods is presented. The motor dimensions and parameters used in the comparison are shown in table 3.1 [18, 20, 21].

Sinusoidal Current Control [21]

The performance of the 3-phase 12/8 MCSRM controlled by sinusoidal current excitation at the rated phase current is analyzed for three different winding configurations: full pitched, double layer short pitched, and single layer short pitched. Performance comparison is shown in figure 3.9(a), and it includes the maximum achievable base speed with the same DC link voltage, power factor and iron loss at that base speed, copper loss, maximum achievable efficiency, torque density, and torque ripple. The SL-FP-MCSRM has the highest copper loss because it has the largest end winding length compared to other winding configurations. The SL-SP-MCSRM has two coils per phase, while the DL-SP-MCSRM has four coils per phase. In order to keep the number of turns per phase the same in both configurations, SL-SP-MCSRM has twice the number of turns per coil which results in higher mean length per turn compared to

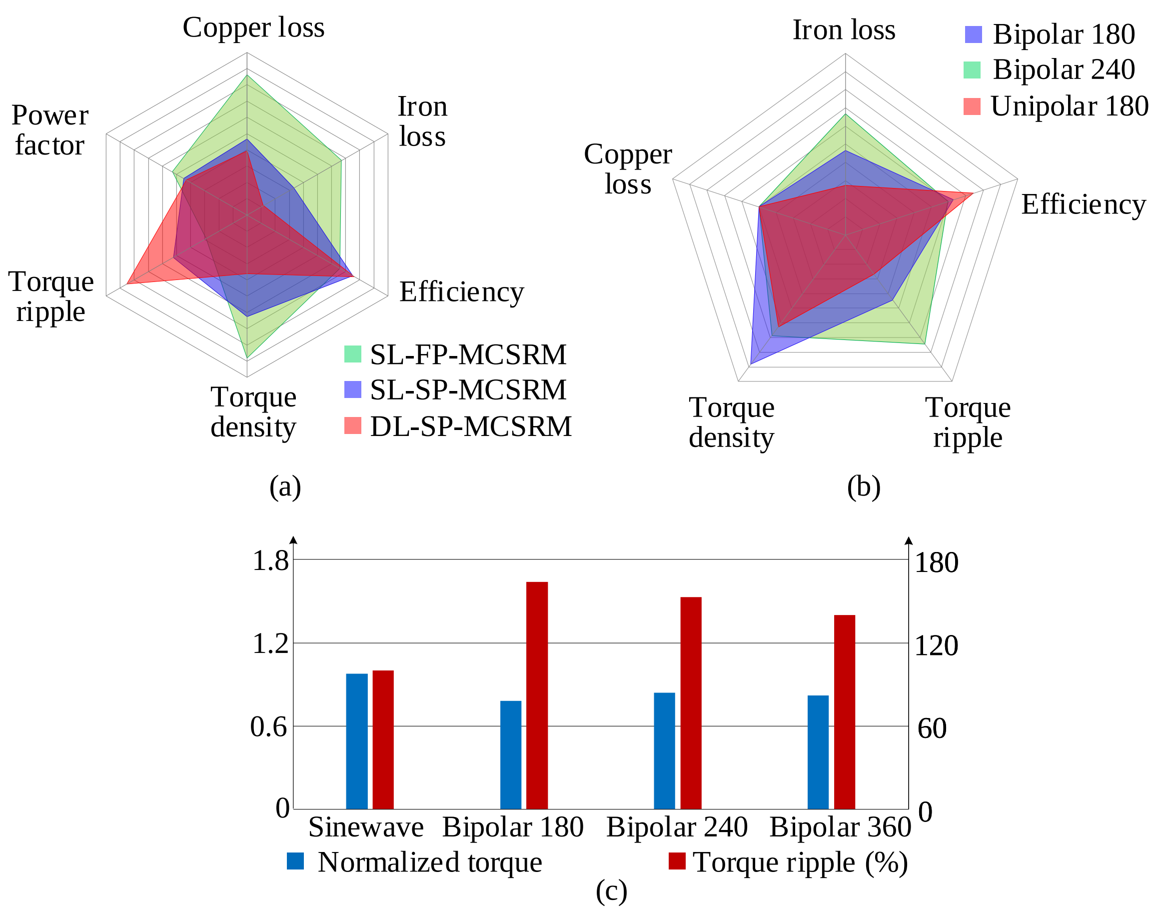

Figure 3.9: 12/8 MCSRM performance comparison (at the rated current) for (a) different winding configurations with 3-phase sinusoidal current excitation, (b) different control methods for SL-SP-MCSRM, (c) different control methods for DL-SP-MCSRM.

the DL-SP-MCSRM. Therefore, SL-SP-MCSRM has a slightly higher copper length than DL-SP-MCSRM and, hence, higher copper loss.

SL-FP-MCSRM has the highest variation in stator and rotor flux density compared to other winding configurations, so it has the highest iron loss [21]. DL-SP-MCSRM has the lowest iron loss. The efficiency of DL-SP-MCSRM is slightly higher than SL-SP-MCSRM. This is because the copper loss is more dominant than iron loss in the low-power 12/8 MCSRM used in this comparison. Since, SL-FP-MCSRM has the highest copper loss, it has the lowest efficiency.

Single layer winding configurations (SL-FP-MCSRM and SL-SP-MCSRM) have double the number of turns per coil compared to the double layer winding (DL-SP-MCSRM), and they can generate higher level of saturation. Among the single layer winding configurations, SL-FP-MCSRM can generate higher saturation for the same MMF compared to SL-SP-MCSRM. With saturation, the effective inductance and the required reactive power decrease. So the machine can achieve higher power factor. Therefore, SL-FP-MCSRM has the highest power factor and DL-SP-MCSRM has the lowest power factor.

The difference between the torque performances with sinusoidal current control can be analyzed based on the motor inductances. The electro-magnetic torque in equation (3.2.1) can be expressed in terms of inductance components:

$$T_{avg} = \frac{3}{2}p(L_d - L_q)i_d i_q \tag{3.4.1}$$

where L_d and L_q are dq inductances, and I_d and I_q are dq currents. $(L_d - L_q)$ is maximum for SL-FP-MCSRM and minimum for DL-SP-MCSRM. Therefore, SL-FP-MCSRM and DL-SP-MCSRM have the highest and lowest torque density, respectively. Figure 3.9(a) also shows that DL-SP-MCSRM has the highest torque ripple, while SL-FP-MCSRM has the lowest torque ripple.

SL-SP-MCSRM [20]

The 3-phase 12/8 SL-SP-MCSRM can also be controlled by unipolar current excitation of 180° conduction period (see section 3.3), bipolar current excitation of 180° conduction period (see section 3.3), and bipolar current excitation of 240° conduction period (see section 3.2). Figure 3.9(b) compares the performance of these excitations. The three excitation currents have the same RMS value and they are applied to the same winding configuration with the same resistance. Hence, they generate the same copper loss. The bipolar current excitations (180° and 240° conduction periods) have higher iron loss than unipolar current excitation due to the change in the polarity of the magnetic flux density.

The torque components generated by self and mutual inductances differ for each current excitation. The torque component by self inductance depends on the rate of change of the self inductance and the torque component by mutual coupling (see equation (2.2.14)) depends on both the direction of the phase current and the slope of mutual inductance profile. The generated electro-magnetic torque is the summation of these torque components. Figure 3.9(b) shows that bipolar current excitation of 180° conduction period and unipolar current excitation of 180° conduction period have the highest and lowest total torque, respectively. Figure 3.9(b) also shows that the bipolar current excitation of 240° conduction period and the unipolar current excitation of 180° conduction period has the highest and lowest torque ripples, respectively. As the three current excitations have the same copper loss, the efficiency difference at the given rotor speed depends on the iron loss. Thus, unipolar current excitation of 180° and bipolar current excitation of 240° have the maximum and minimum efficiencies, respectively.

DL-SP-MCSRM [18]

The 3-phase 12/8 DL-SP-MCSRM can be controlled by sinusoidal excitation, bipolar current excitation of 180° conduction period (see section 3.3), bipolar current excitation of 240° conduction period (see section 3.2), and bipolar current excitation of 360° conduction period (see section 3.3). Performance comparison presented in figure 3.9(c) is based on average torque and torque ripple. Although the bipolar current excitation of 360° conduction period generates the highest torque component by mutual coupling [18], it also generates negative torque by the self inductance. This results in lower total torque as compared to the sinusoidal excitation. As it can be seen from figure 3.9(c), sinusoidal excitation achieves balanced self and mutual torque components ending up with higher total torque than the other bipolar current excitation types. The sinusoidal excitation has the minimum torque ripples as it provides smoother change in the current waveform. The other bipolar rectangular currents have a higher rate-of-change of current.

3.5 Summary

The phase current waveforms of MCSRMs can be unipolar rectangular waveforms, bipolar rectangular waveforms or sinusoidal waveforms [20, 21, 26]. For sinusoidal current excitation, the MCSRM can be considered as an AC motor where the standard voltage source inverter and vector control can be used. The performance of a low-power 3-phase 12/8 MCSRM with different winding configurations and different control methods has been compared. The comparison reveals that for the sinusoidal current excitation, the single layer full pitched winding shows better performance in terms of torque density, torque ripple, and power factor. The double layer short pitched winding has the highest efficiency. For single layer short pitched winding, the bipolar phase current of 180° electrical conduction period has the highest torque density. The unipolar phase current of 180° electrical conduction period has the highest efficiency and the lowest torque ripple. For double layer short pitched winding, sinusoidal current excitation has the maximum torque density and the minimum torque ripple.

Chapter 4

Modeling of Mutually Coupled SRMs

4.1 Introduction

Modeling establishes a relationship between the phase currents, phase flux linkages (or inductances), and rotor position, which is necessary to analyze the performance of the motor. Only the modeling methods that consider mutual coupling are discussed in this chapter. Modeling methods can be either a derivative model or an integral model. In the derivative model, the phase current is calculated from the derivative of the flux linkage as:

$$i_{phase} = \frac{v_{phase} - \dfrac{d\lambda_{phase}}{dt}}{R} \tag{4.1.1}$$

where λ_{phase}, i_{phase}, and v_{phase} are the phase flux linkage, phase current, and phase voltage, respectively. Then, the phase current is used to obtain the phase flux linkage by a non-linear relation that can be a look-up table or a non-linear equation such as an exponential function. Afterwards, the phase flux linkage is substituted in equation (4.1.1) to calculate the phase current and so on.

In the integral model, the phase flux linkage is calculated:

$$\lambda_{phase}(i, \theta) = \int (v_{phase} - i_{phase}R)dt \tag{4.1.2}$$

Then, the phase flux linkage is used to obtain the phase current by a non-linear relation. The integral model in equation (4.1.2) is more accurate than the derivative model in equation (4.1.1), as the flux linkage derivative amplifies the noise in the model [55]. For instance, if there is a 5^{th} order harmonic noise, its derivative has a magnitude which equals to the magnitude of this 5^{th} order harmonic multiplied by the angular frequency and a constant of five.

In this chapter, the existing modeling methods for the mutual couplting between phases are analysed. Section 4.2 presents the discussion of the analytical methods including inductance modeling and magnetic circuit modeling. The LUT based modeling methods are investigated in section 4.3. Modeling of MCSRM using different software environments such as MATLAB/Simulink and JMAG are referred by Co-simulation and is discussed in section 4.4. Section 4.5 provides the summary of the chapter and the conclusion of the most accurate modeling method for MCSRM.

4.2 Analytical Methods

Analytical modeling methods are based on non-linear equations to describe the non-linear relationship between the phase current, phase flux linkage, and rotor position.

Inductance Modeling

The self and mutual inductance profiles are expressed by Fourier series in this method [56–63]. If the first three harmonic orders are considered, the self inductance is expressed as:

$$L(i,\theta) = \sum_{n=0}^{\infty} L_n(i)cos(n\theta) \tag{4.2.1}$$

$$L(i,\theta) = L_0(i) + L_1(i)cos(n\theta) + L_2(i)cos(2n\theta) \tag{4.2.2}$$

where $L_0(i)$, $L_1(i)$ and $L_2(i)$ are Fourier coefficients of the DC value, first order and second order harmonics. In order to solve $L_0(i)$, $L_1(i)$ and $L_2(i)$, the inductance values at three different rotor positions are calculated by finite element analysis (FEA) or measured from experiments for single-phase excitation. For more accurate modeling of self inductance, the first five harmonic orders can be considered instead of three. In this case, five rotor positions will be required to solve for the five Fourier coefficients [64, 65].

Similarly, the mutual coupling of the excited phase on the unexcited phase can be expanded by Fourier series as [57]:

$$M(i,\theta) = \sum_{n=0}^{\infty} M_n(i)cos(n\theta) \tag{4.2.3}$$

where $M_n(i)$ represents the Fourier series coefficients. For 2-phase excitation, the mutual inductance is a function of the two phase currents [56, 66]:

$$M(i_x, i_y, \theta) = \sum_{n=0}^{\infty} M_n(i_x, i_y)cos(n\theta) \tag{4.2.4}$$

where i_x and i_y are the currents of the excited phases. Solving equation (4.2.4) is complicated as it is a function of two phase currents unlike the case for the self inductance. Authors in [67] mentioned that solving equation (4.2.4) requires at least 4 rotor positions and 10 steps of each phase current, resulting in 400 measurements. This explains why equation (4.2.4) was mentioned in [56] and [66] without solving it. Equation (4.2.4) is for 2-phase excitation, thus, the complexity of the inductance model increases as the number of excited phases increases. As a result, it can be concluded that the inductance model can successfully model the self inductance in linear and saturation regions like the case in CSRMs where single-phase excitation dominates. However, it is more complicated to model the MCSRMs using the inductance model.

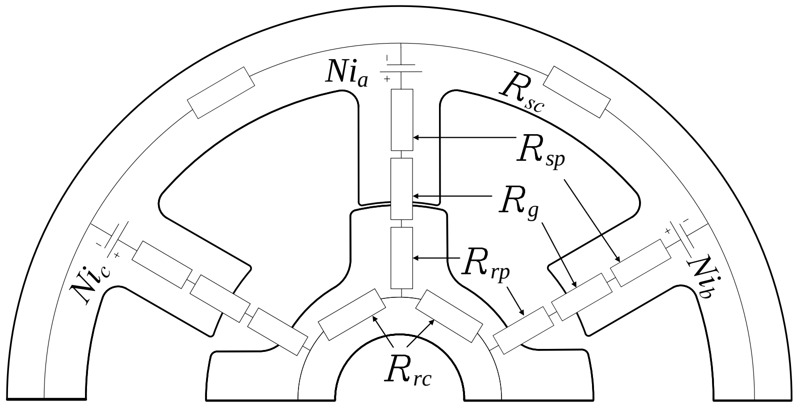

Figure 4.1: Magnetic circuit model for 3-phase 6/4 SRM.

Magnetic Circuit Modeling

The least common analytical modeling method for MCSRMs is the magnetic circuit modeling due to its high level of complexity. The equivalent magnetic circuit of SRM can be modeled with a number of reluctance elements. There is no standard way to model the equivalent magnetic circuit like the case in inductance modeling. Several approaches have been proposed to increase the model accuracy at the expense of model complexity and simulation time [25, 68–70]. It can be generalized that there are five main reluctances describing stator core R_{sc}, rotor core R_{rc}, stator pole R_{sp}, rotor pole R_{rp} and air gap R_g as shown in figure 4.1.

It is worth mentioning that magnetic circuit models which include the mutual coupling effect are either for CSRMs to model the mutual coupling during commutation [69, 70] or for MCSRMs with two phases of equal current excitation [25, 68] where the excited phases have the same current waveform without phase shift. Authors in [71] and [72] show that the variation of the mutual inductance with current in CSRM is very small even during saturation. This simplifies the mutual coupling model as an inductance which varies only with rotor position. Thus, models in [70] and [69] cannot be used for MCSRMs modeling. In MCSRM, the 2-phase equal current excitation is equivalent to single-phase excitation [27] as the two phases carry the same current, which also simplifies the modeling of the mutual coupling. Therefore, the models in [68] and [25] cannot accurately model the mutual coupling if the two excited phases have different current values.

Other Methods

In [73], the single-phase excitation magnetic characteristics are used to predict the two-phase excitation magnetic characteristics. As mentioned earlier, mutual inductance in CSRM is almost linear and does not strongly depend on phase currents. This simplifies the modeling of mutual coupling in CSRMs, but it cannot be used for modeling it in MCSRMs. Mutual coupling is modeled in [72] for 2-phase excitation in CSRMs and it is dependent on rotor position and independent on current which ease the modeling approach. This assumption is not valid for MCSRM, and hence, this method cannot be used for MCSRMs modeling.

An analytical model is introduced in [28] to SL-FP-MCSRM close to the magnetic circuit modeling, where the pole flux linkage is decoupled into main and fringe flux linkage and they depend on rotor position and MMF. Results of [28] only show two phases have equal current excitation. Therefore, it cannot be used for MCSRM with different excited phase current values. Besides results comparing that model with FEA have a relatively high error even at linear magnetic operation.

4.3 Look-up Table Based Models

Modeling methods which use LUTs have higher accuracy compared to the analytical models which use empirical formulas. For single-phase excitation like the case in CSRMs, a 2D LUT is obtained from FEA or experimentally. This LUT has single phase current and rotor position as inputs, and phase flux linkage as the output, and it can be represented as $\lambda_{phase} = f(i_{phase}, \theta)$. For the integral model, which is less prone to errors and noise amplification as compared to the derivative model, the LUT should be inverted to obtain the phase current from the phase flux linkage: $i_{phase} = f(\lambda_{phase}, \theta)$ [55]. In order to model the instantaneous torque, another 2D LUT is required which expresses the relationship between the phase current, rotor position, and electro-magnetic torque: $T_e = f(i_{phase}, \theta)$. For CRSMs, since mutual coupling is negligible, a 2D LUT for one phase can be used to model the operation of the motor. For multi-phase excitation, such as for a 3-phase motor, since mutual coupling cannot be ignored, four 4D LUTs would be needed to describe the relationship between phase currents, phase flux linkages, and torque: $\lambda_{a,b,c} = f(i_a, i_b, i_c, \theta)$ and $T_e = f(i_a, i_b, i_c, \theta)$. The mutual coupling between phases is modeled by considering the total phase flux linkages (λ_{abc}) into account, instead of separately calculating the self and mutual inductance. This increases the accuracy and simplifies the calculations.

Dependent Phase Current Modeling

As discussed in section 3.2, in dependent phase current control, the sum of phase currents is zero at any instant (such as in a balanced 3-phase system). In this case, the dimensions of the LUTs can be reduced from 4D to 3D by transforming the system variables from *abc* stationary frame ($\lambda_{a,b,c} = f(i_a, i_b, i_c, \theta)$) to *dq* rotating frame

($\lambda_{d,q} = f(i_d, i_q, \theta)$). Reducing the size of the LUTs results in faster simulation time and provides more flexibility in obtaining the inverted LUTs for the integral model. The mutual coupling between phases is modeled by considering the total phase flux linkages ($\lambda_{a,b,c}$) into account, instead of separately calculating the self and mutual inductance. This increases the accuracy and simplifies the calculations. By transforming the stationary frame variables into rotating frame variables, a MCSRM can be modeled similar to an AC motor. Saturation and spatial harmonics are included in the model by obtaining the LUTs of the flux linkages and the instantaneous torque as a function of *dq* currents and rotor position. Spatial harmonics is due to the slotting effect of stator teeth which generates a non-uniform magnetic field. In other words, the stator of MCSRM can be considered as a stator of an AC motor with more salient teeth. A dynamic model of an interior permanent magnet synchronous motor (IPMSM) considering spatial harmonics and saturation was introduced in [74] to a 3-phase 12-slot/8-pole IPMSM. In [75], the same method has been used to model a 3-phase 12/8 MCSRM.

Figure 4.2 shows the bock diagram of the dynamic models in [74] and [75] for dependent phase current control. First, a range of *dq* currents that covers two quadratures in the *dq* frame is defined. The *dq* currents are then transferred to *abc* currents for the characterization of the motor in FEA. When *d*-axis is aligned with phase *a* at the initial rotor position, *abc* to *dq* transformation is known as cosine-based Park transformation. In this case, the *d*-axis is defined as the position where the stator poles of phase *a* are at the aligned position as shown in figure 4.3(a). If the *d*-axis is defined to be 90° behind the aligned position for phase *a* (see figure 4.3(b)), it is referred as sine-based Park transformation. In this case, the stator poles of phase *a*

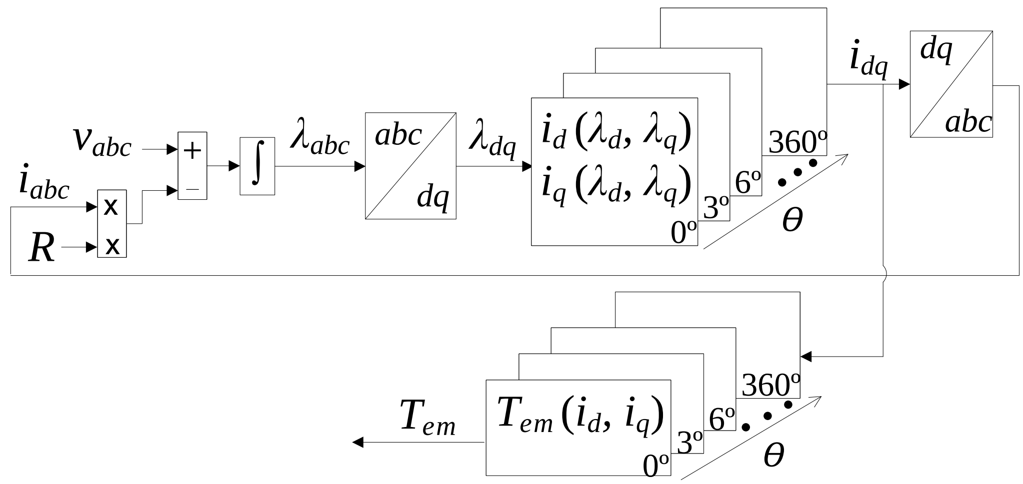

Figure 4.2: Dynamic model of a 3-phase MCSRM for dependent phase current control.

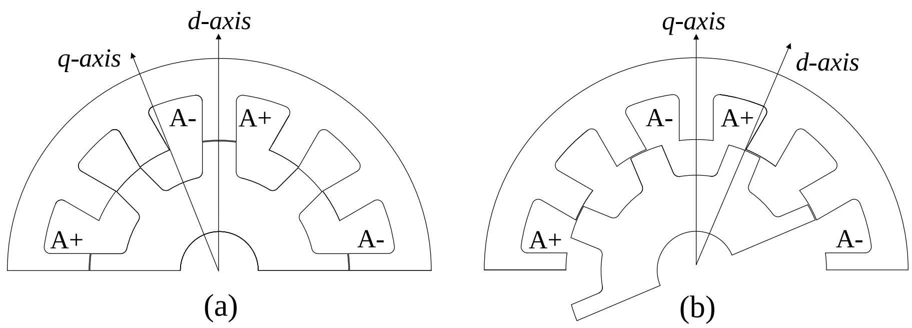

Figure 4.3: Initial rotor position of 12/8 MCSRM when (a) d-axis is aligned with phase a, (b) d-axis is 90° behind phase a.

are at the unaligned position at the initial rotor position.

The two 3D LUTs $\lambda_d = f(i_d, i_q, \theta)$ and $\lambda_q = f(i_d, i_q, \theta)$ are then inverted to $i_d = f(\lambda_d, \lambda_q, \theta)$ and $i_q = f(\lambda_d, \lambda_q, \theta)$. The 3D LUTs can be considered as multiples of 2D LUTs ($\lambda_d = f(i_d, i_q)$) at different rotor positions. Therefore, the 2D LUTs $\lambda_d = f(i_d, i_q)$ and $\lambda_q = f(i_d, i_q)$ are inverted to $i_d = f(\lambda_d, \lambda_q)$ and $i_q = f(\lambda_d, \lambda_q)$ at each rotor position.

Expressing the dq currents as a function of dq flux linkages possess some inversion complexity. In order to solve this problem, *gridfit* function [76] from Matlab Central is used in [74]. In [75], *contourc* function from Matlab is used. To our experience, the *gridfit* function in [76] is more flexible than *contourc* for LUTs inversion. For modeling the torque, the 4D LUT ($T_e = f(i_a, i_b, i_c, \theta)$) is reduced to a 3D LUT ($T_e = f(i_d, i_q, \theta)$). An inversion is not needed for the torque LUT.

Independent Phase Current Modeling

This type of modeling is applied to independent phase current control, which was discussed in section 3.3. For 2-phase excitation, the same procedures are applied as for the single-phase excitation. However, 3D LUTs are obtained instead of 2D LUTs: $\lambda_{a,b} = f(i_a, i_b, \theta)$ and $T_e = f(i_a, i_b, \theta)$. Then, the flux linkage LUTs are inverted to $i_{a,b} = f(\lambda_a, \lambda_b, \theta)$ [77]. Inverting the LUTs is similar to the method described in section 4.3. The same approach can be applied for any multi-phase excitation. Figure 4.4 shows the modeling diagram for independent 3-phase current control. Please note that if the independent three phases are transformed into the dq synchronous rotating frame, the transformed components will be the d-axis, q-axis, and zero-sequence component. Thus, the advantage of reducing the dimensions of the LUTs does not exist because of the existence of the zero-sequence component and, hence, there is no need for the dq transformation.

Other Methods

The disadvantage of the LUT based methods is the large number of finite element simulations required to build the LUTs and the complexity in the inversion of LUTs, especially for multi-phase excitation. Authors in [78] tried to reduce FEA steps by

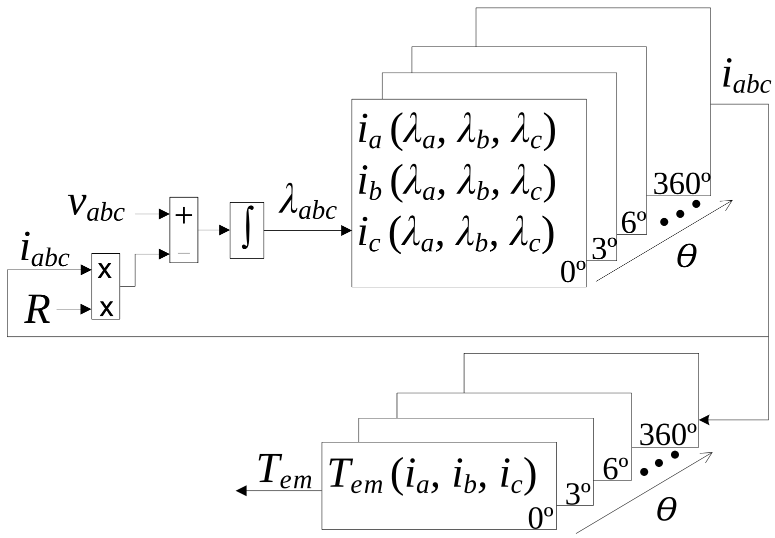

Figure 4.4: Dynamic model of a 3-phase MCSRM for independent phase current control.

using a more coarse phase current range. However, that resulted in considerable errors in the model when compared to FEA results.

Authors in [67] and [79] used feed-forward artificial neural network (FF-ANN) to model the mutual coupling with reduced FEA steps for CSRM and SL-FP-MCSRM, respectively. In [79], FEA results were for 2-phase excitation with keeping one phase current as a constant and assuming linear mutual effect of the constant phase current on the other phase. Results obtained from FEA are applied to ANN through a back-projective training. Keeping one phase current constant value reduced the FEA steps significantly. However, the results did not account for saturation and an experimental validation was not provided [79].

In [67], FF-ANN was used to calculate the mutual flux linkage with 2-phase excitation in CSRM. The data used to train the ANN is obtained from FEA for 2-phase excitation with 25 current cases, which is a relatively low number. No experimental results have been provided to validate the feasibility of this method to model mutual coupling.

Comparing figure 2.3(c) and figure 2.4(e), it can be observed that SL-FP-MCSRM and DL-SP-CSRM have the same flux distribution. As a result, a SL-FP-MCSRM with 2-phase equal current excitation can be considered as a DL-SP-CSRM with single-phase excitation. Based on that, authors in [80] developed a model for a 3-phase SL-FP-MCSRM considering the two excited phases as single phase having the same current waveform. Symmetric bipolar current excitation was used with a phase shift of 120° electrical. However, the assumption that the two excited phases have equal current magnitude in symmetric bipolar current excitation is not valid during commutation. This assumption is not valid either at high speed operation when current control is not applicable and current waveforms deviate from the rectangular shape. Thus, the use of this modeling method is limited.

In [29], a dynamic model was introduced to CSRM and SL-FP-MCSRM. Both models use a LUT that describes the relationship between flux per tooth and MMF. The flux per tooth is calculated from the phase flux linkages, and the phase currents are calculated from the MMF. Since both models have the same LUT, the SL-FP-MCSRM model was valid only for 2-phase excitation with equal currents. Therefore, this approach also has limitations in modeling.

In another modeling approach, the authors in [81] and [82] divided each phase of a 12/8 CSRM into two subphases, and each subphase compromises two coils. For instance, phase a is divided into two subphases a_1 and a_2, and both a_1 and a_2 have two coils each. Similarly, phases b and c were divided into b_1, b_2, c_1 and c_2. Two asymmetric half bridge converters were used to supply the 12/8 CSRM, which has four coils per phase, so that one converter is responsible for the subphases a_1, b_1 and c_1, and the other converter is responsible for the subphases a_2, b_2 and c_2. It was claimed that the 12/8 CSRM supplied by two converters instead of one was a new MCSRM, and it was called dual channel MCSRM (DL-MCSRM).

In [81], a dynamic model was introduced to this DL-MCSRM based on decoupling of the subphase flux linkage (λ_{a1}) into self and mutual flux linkages. Since the two subphases a_1 and a_2 have the same current, their self and mutual flux linkage LUTs have a single phase current input. This model is updated in [82], so that LUTs describe the total flux linkage of a_1 and a_2 without decoupling them. This is similar to CSRM modeling. Since the DC-MCSRM is a CSRM supplied by two converters, the models in [81] and [82] cannot be used in MCSRM modeling.

4.4 Modeling Through Co-simulation

The electro-magnetic model of a MCSRM in an FEA software such as JMAG [83] can be used in simulation tools such as Saber [84] or Matlab [85]. This is called co-simulation. It provides the highest accuracy as compared to other methods as it utilizes the FEA model of the motor. However, co-simulation usually requires much longer simulation time, which limits its practicality in the design of a MCSRM drive.

4.5 Summary

Modeling methods for SRMs are either analytical methods or look-up table (LUT) based methods. Analytical methods include inductance modeling and magnetic circuit modeling. Inductance modeling is used to model the self-inductance by the

Fourier expansion of the first three [56,58,59] or the first five harmonic orders [64,65]. However, this method cannot be used to model the mutual coupling between phases due to the complexity and large number of measurements required [56, 66, 67]. In the magnetic circuit modeling, the SRM is modeled by a number of reluctance elements. For CSRM, two phases can be excited simultaneously during commutation, magnetic circuit modeling methods that consider the mutual coupling in CSRM during commutation cannot be used in MCSRM, as the mutual coupling in CSRM is dependent on rotor position only but not the phase current, since the current values during commutation are small, in addition to the windings configuration of CSRM that minimizes the mutual flux paths [71,72]. The existing magnetic circuit modeling methods for MCSRM can model the mutual inductance for two phases of equal instantaneous current [25,68], which can be considered as a single-phase excitation. No magnetic circuit modeling method in the literature accounts for the mutual coupling in MCSRM where the currents of the excited phases differ instantaneously, such as the 3-phase sinusoidal current excitation.

LUT based methods are typically more accurate than the analytical methods. For the CSRM, two 2D LUTs are obtained from finite element analysis (FEA) which are $\lambda = f(i, \theta)$ and $T_e = f(i, \theta)$. Here λ is the phase flux linkage, i is the phase current, θ is the rotor position, and T_e is the instantaneous phase torque. The first LUT represents the non-linear relationship between the phase current, rotor position, and the phase flux linkage. The second LUT represents the non-linear relationship between the phase current, rotor position, and the phase torque [22]. In order to avoid error amplification in the model, phase current is found by inverting the flux linkage LUT as $i = f(\lambda, \theta)$ [55]. This inversion allows the calculation of phase flux linkage by integration. Then, the calculated flux linkage is applied to the inverted LUT to estimate the phase current [55].

For 3-phase MCSRM where the three phases are excited simultaneously, the conventional LUT-based modeling methods require four 4D LUTs from FEA [22]. Three LUTs describe the phase flux linkages as $\lambda_u = f(i_u, i_v, i_w, \theta)$, $\lambda_v = f(i_u, i_v, i_w, \theta)$ and $\lambda_w = f(i_u, i_v, i_w, \theta)$, where i_u, i_v, i_w are the 3-phase currents and $\lambda_u, \lambda_v, \lambda_w$ are the 3-phase flux linkages. The last LUT describes the instantaneous torque as $T_e = f(i_u, i_v, i_w, \theta)$. The 4D LUTs of the phase flux linkages are inverted similar to the single-phase excitation case. However, the inversion of a 4D LUT is more complicated in multi-phase excitation compared to single-phase excitation. For balanced current operation, in which the sum of the 3-phase currents is equal to zero, the 3-phase *uvw* stationary frame can be transformed into the *dq* rotating frame without the zero sequence component. Therefore, the 4D LUTs are simplified into 3D LUTs: $\lambda_d = f(i_d, i_q, \theta)$, $\lambda_q = f(i_d, i_q, \theta)$ and $T_e = f(i_d, i_q, \theta)$, where λ_d, λ_q are the *dq* flux linkages and i_d, i_q are the *dq* currents. These procedures are introduced in [74] to a 12-slot/8-pole interior permanent magnet (IPM) synchronous motor. The same method in [74] is applied in [75] for a 3-phase 12/8 MCSRM with sinusoidal current excitation. The 3D LUT is inverted in [74] by *gridfit* tool from Matlab Central [76], while in [75], *contourc* function in Matlab is used. The *gridfit* tool is simpler to apply than the *contourc* function to invert the LUTs.

Chapter 5

Dynamic Vector Modeling of Three-Phase Mutually Coupled SRMs with Single dq-Quadrant Look-up Tables

5.1 Introduction

As concluded from the previous chapter, the LUT based models are the most accurate among the other modeling methods. Authors in [75] presented a dynamic model to a 3-phase MCSRM where the LUTs used in that model represent two quadrants of the *dq* synchronous reference frame. In this chapter, a dynamic model is introduced to a 3-phase MCSRM, where the required LUTs represent a single quadrant of the *dq* frame, hence, the size of the LUTs and the required FEA steps are reduced by 50%. The dimensions of the LUTs obtained from the FEA model are reduced from 4D to 3D by transforming the system from the 3-phase stationary reference frame to the *dq* synchronous reference frame. Afterwards, the dimensions of the LUTs are further reduced from 3D to 2D by using the vector representation of phase current and electro-magnetic torque instead of instantaneous values. Therefore, rotor position does not need to be an input to the LUTs. The advantages of the proposed dynamic model are:

1. LUTs are independent of rotor position so the dimensions of LUTs decreases from 3D to 2D.

2. The LUTs required in the proposed method represent a single *dq* quadrant, so the size of the LUTs and the number of the required FEA steps are reduced by 50% compared to the two-quadrant based method in [75].

Starting from this chapter, the 3-phase stationary reference frame will be referred to as *uvw* instead of *abc* to avoid the confusion between the three phases (I_{abc}) and their Fourier coefficients (I_{an} and I_{bn}). The rest of the chapter is organized as follows. Section 5.2 explains the proposed dynamic modeling method. Section 5.3 validates the

Table 5.1: The Specifications of the MCSRM Used in This Thesis

Parameter	Value	Parameter	Value
Phase Number	3	Rotor inner radius	30.5 mm
Stator poles	12	Shaft radius	12.5 mm
Rotor poles	8	Air-gap length	0.3 mm
Axial length	70 mm	Turns per phase	28
Stator outer radius	68 mm	Rated power	2 kW
Stator inner radius	56.7 mm	Rated torque	3 Nm
Rotor outer radius	41.5 mm	Peak current	21.21

proposed method with FEA, and section 5.4 validates it with experiments. Finally, section 5.5 presents the summary of the chapter.

5.1.1 Investigated Motor

The motor used in this thesis is 12/8 3-phase SRM and it was designed to operate as a CSRM. I changed the windings configuration to make it operate as a MCSRM. Figure 5.1 shows the updated windings configuration of the MCSRM used in this thesis. Table 5.1 shows the parameters of the MCSRM and figure 5.2 shows the motor itself. The FEA analysis, simulation and experimental results in this thesis are conducted on that motor.

The base speed of the SRM is 6000 rpm at 300 DC-link voltage when it operates as a CSRM. At the base speed, the induced electromotive force (emf) of the motor is equal to the DC-link voltage. Hence, the current control can be applied as long as motor speed is less than or equal to the base speed, since the induced emf which opposes current will be lower than the DC-link voltage. After changing the windings configuration of the SRM to make it operate as a MCSRM, the induced emf characteristics due to the 3-phase sinusoidal current excitation is different than the CSRM

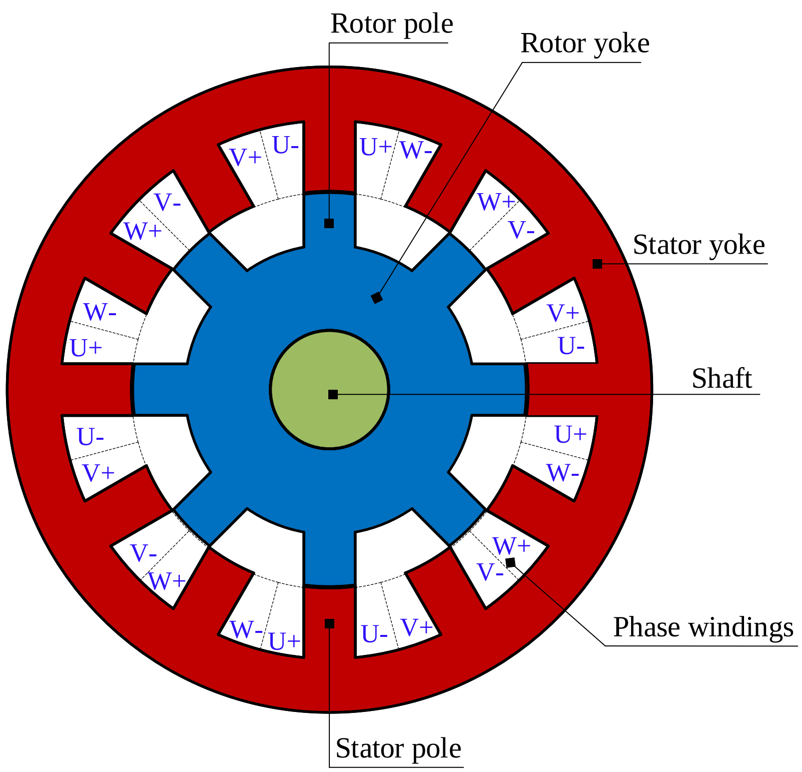

Figure 5.1: Winding configuration for the 12/8 mutually coupled SRM

with single-phase excitation. Hence, the base speed is different as well. Table 5.2 shows the corresponding base speed at different DC-link voltages when the motor operates as MCSRM with sinusoidal current excitation.

Table 5.2: The corresponding rated speed at a given DC-link voltage.

DC-link Voltage	Rated speed
300V	2500 rpm
250V	2200 rpm
200V	1800 rpm

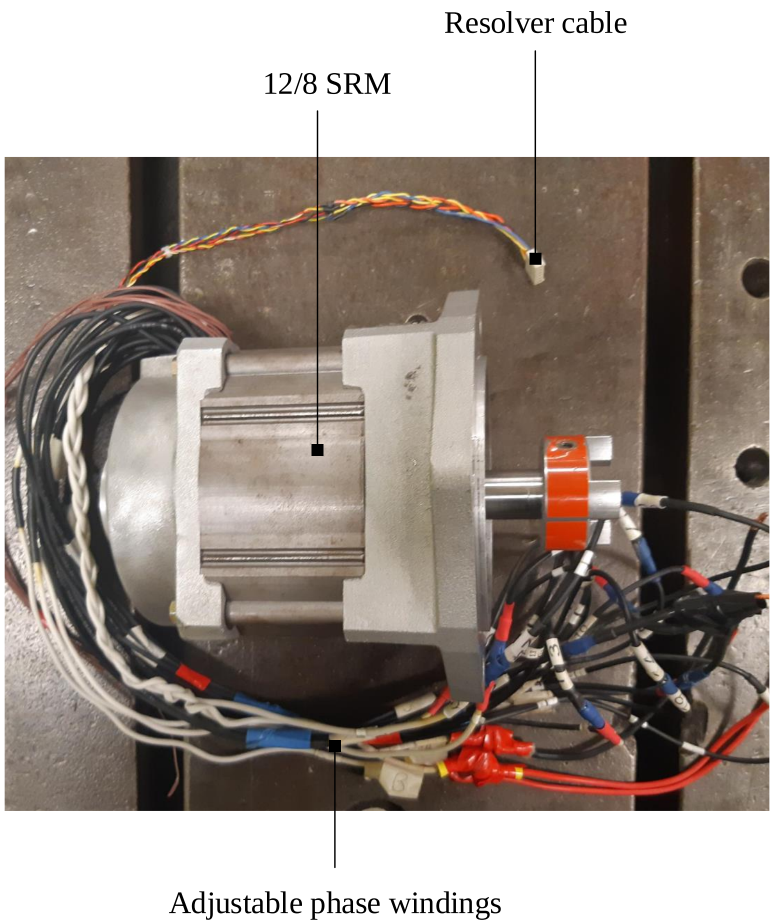

Figure 5.2: The 12/8 SRM used in this thesis

5.1.2 Direct-and Quadrature-axis Locations

The location of d- and q- axis for the 3-phase 12/8 MCSRM at initial rotor position is shown in figure 5.3. As mentioned earlier in section 4.3, the initial position can be aligned with phase u, or 90° behind phase u (see figure 4.3). It can be noticed from figure 5.3 that the initial position is assumed to be aligned with phase u and, hence, the cosine-based Park transformation will be used. The reason behind making the initial position as the alignment position is practically easier to align the rotor with

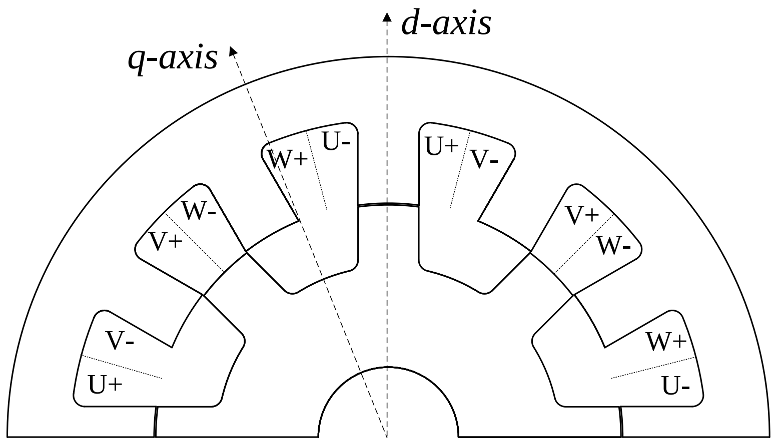

Figure 5.3: Windings configuration of a 3-phase 12/8 MCSRM

phase u versus the alignment of the rotor midway between the phases u and v. The location of q-axis is 90° electrical phase shifted from the d-axis. Since the MCSRM I am using has four pole pair, the location of q-axis is 22.5° mechanical phase shifted from d-axis.

5.1.3 Clarke-Park Transformation and Fourier Expansion

The Clarke-Park transformation can be power variant or power invariant. In power variant transformation, the resultant vector of d- and q- axis currents has the same magnitude as the phase current magnitude. However, the power calculations from the dq synchronous reference frame are not similar to the power calculations from the 3-phase stationary reference frame. In power invariant transformation, the power calculations from the 3-phase stationary frame and the dq synchronous frame are the same. However, the magnitude of phase current is different from the magnitude of the resultant vector of d- and q-axis currents. The power variant transformation is used in this thesis, equations (5.1.1) and (5.1.2) show the power variant transformation matrix at a given rotor position, θ:

$$\begin{pmatrix} d \\ q \\ 0 \end{pmatrix} = \frac{2}{3} \begin{bmatrix} cos(\theta) & cos(\theta - \frac{2\pi}{3}) & cos(\theta + \frac{2\pi}{3}) \\ -sin(\theta) & -sin(\theta - \frac{2\pi}{3}) & -sin(\theta + \frac{2\pi}{3}) \\ \frac{1}{2} & \frac{1}{2} & \frac{1}{2} \end{bmatrix} \begin{pmatrix} u \\ v \\ w \end{pmatrix} \tag{5.1.1}$$

$$\begin{pmatrix} u \\ v \\ w \end{pmatrix} = \begin{bmatrix} cos(\theta) & -sin(\theta) & 1 \\ cos(\theta - \frac{2\pi}{3}) & -sin(\theta - \frac{2\pi}{3}) & 1 \\ cos(\theta + \frac{2\pi}{3}) & -sin(\theta + \frac{2\pi}{3}) & 1 \end{bmatrix} \begin{pmatrix} d \\ q \\ 0 \end{pmatrix} \tag{5.1.2}$$

On the other hand, any signal can be represented by Fourier series as:

$$f(\theta) = \frac{a_o}{2} + \sum_{n=1}^{\infty} [a_n cos(n\theta) + b_n sin(n\theta)] \tag{5.1.3}$$

where a_o is the signal DC offset, a_n and b_n are the cosine and sine Fourier coefficients for the n^{th} order harmonic. For a sinusoidal wave with zero DC offset (a_o=0), equation (5.1.3) is updated to:

$$f(\theta) = a_1 cos(\theta) + b_1 sin(\theta) \tag{5.1.4}$$

Comparing phase u in equation (5.1.2) by equation (5.1.4), it can be concluded that the d-axis component is equal to the cosine Fourier coefficient, and the q-axis component is equal to the negative value of the sine Fourier coefficient. Hence, to make the sine Fourier coefficient similar to the q-axis component, Fourier series will be represented in this thesis as:

$$f(x) = \frac{a_o}{2} + \sum_{n=1}^{\infty}[a_n cos(nx) - b_n sin(nx)] \tag{5.1.5}$$

5.2 The proposed Dynamic Model

The MCSRM used in this thesis is simulated in FEA with sinusoidal current excitation. The next sections discuss how to build the required LUTs for the modeling of phase currents and electro-magnetic torque.

5.2.1 Modeling of the phase currents

The 3-phase flux linkages output from the FEA model have the same waveform and are shifted by 120° electrical from each other. Figure 5.4(a) shows the 3-phase flux linkages when $[i_d, i_q]$=$[4, 16]$A. It can be observed that the sinusoidal current excitation results in a distorted phase flux linkage waveform due to the effect of spatial harmonics. Figure 5.5 shows the flux distribution at the alignment rotor position, θ=0, when $[|i_d|, |i_q|]$=$[4, 16]$A among the four quadrants of the synchronous reference frame. Figure 5.5 reveals that for the same magnitude of dq currents, the dq flux linkages also have the same magnitude. Moreover, the sign of the d-axis flux linkage follows the sign of d-axis current, and the sign of q-axis flux linkage follows the sign of q-axis current. Thus, the resultant flux linkage vectors from the dq flux linkages in the four quadrants have the same magnitude and are shifted 90° from each other. The symmetry of the flux linkage is due to the absence of rotor magnets and rotor winding in MCSRMs. Exploiting this symmetry in the flux distribution for the same

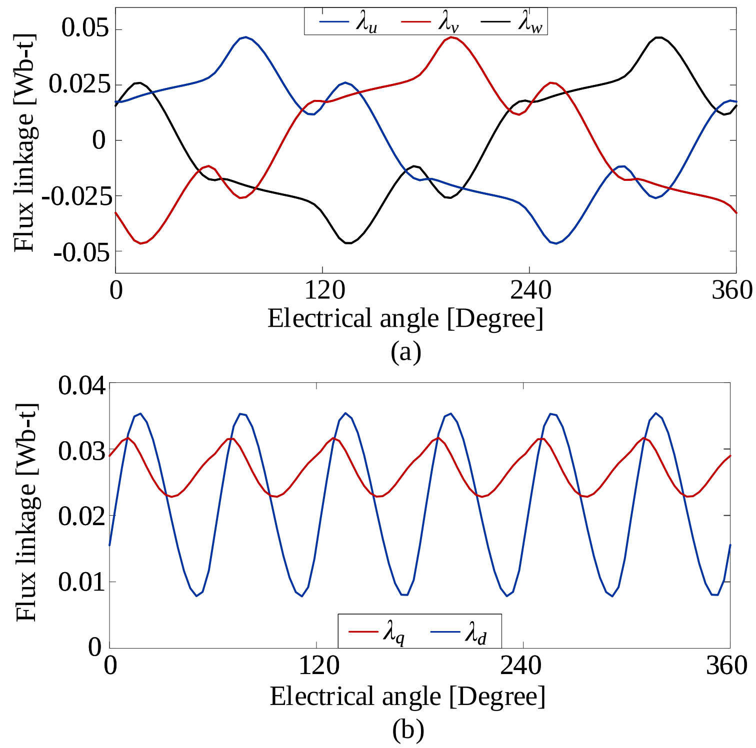

Figure 5.4: (a) 3-phase flux linkages from the FEA model for sinusoidal current excitation when $[i_d, i_q]$ = [4, 16]A, (b) dq flux linkages when $[i_d, i_q]$ = [4, 16]A

magnitude of dq currents, the MCSRM can be simulated in FEA with sinusoidal currents which represent the 1^{st} quadrant of the synchronous reference frame. This is the first Step in figure 5.6, which shows the block diagram for LUTs generation from the FEA model.

In AC motors (such as synchronous motors and induction motors), there is a symmetry between the first and third quadrants as they represent the motoring mode of operation. There is also a symmetry between the second and fourth quadrants as they represent the generating mode of operation. This symmetry is used in the modeling of synchronous motors in [74] and it is also used in the modeling of MCSRMs in [75]. In SRMs, there is a symmetry between the four quadrants (see figure 5.5)

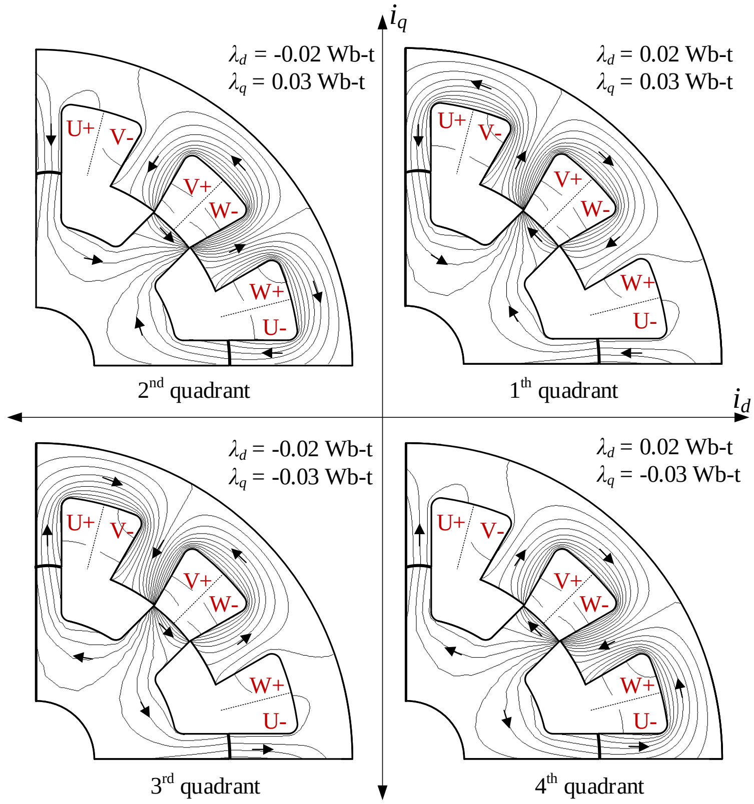

Figure 5.5: Flux distribution at the alignment rotor position ($\theta = 0$) when dq currents magnitude is $[|i_d|, |i_q|]$=$[4, 16]$A among the four quadrants of the synchronous reference frame

and this symmetry is used in the proposed dynamic model.

After Step 1, the 3-phase flux linkages from the FEA model are represented in 3D LUTs: $\lambda_u = f_u(i_d, i_q, \theta)$, $\lambda_v = f_v(i_d, i_q, \theta)$ and $\lambda_w = f_w(i_d, i_q, \theta)$. As shown in the second Step in figure 5.6, the 3-phase flux linkages are transformed into synchronous reference frame using Clarke and Park transformations:

$$\lambda_d = f(i_d, i_q, \theta) \tag{5.2.1a}$$

$$\lambda_q = f(i_d, i_q, \theta) \tag{5.2.1b}$$

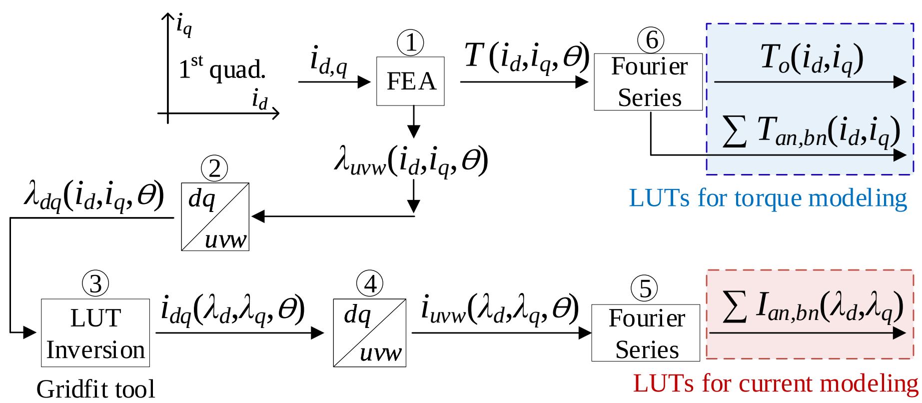

Figure 5.6: LUTs generation from the FEA model

Figure 5.4(b) shows the dq flux linkages transformed from the 3-phase flux linkages in figure 5.4(a). The dq flux linkages are not constant with rotor position due to the distortion in the 3-phase flux linkages caused by the spatial harmonics.

Next, we need to invert the flux linkage LUTs into current LUTs to allow the calculation of the phase flux linkage by integration. At each rotor position, the 3D LUTs of the dq flux linkages in equation (5.2.1) can be expressed as 2D LUTs: $\lambda_d = f(i_d, i_q)$ and $\lambda_q = f(i_d, i_q)$. The *gridfit* tool from Matlab Central [76] is used to invert the LUTs at each rotor position, as shown in Step 3 in figure 5.6. Hence, two 3D LUTs are obtained which describe the dq currents as a function of dq flux linkages and rotor position:

$$i_d = f_d(\lambda_d, \lambda_q, \theta) \tag{5.2.2a}$$

$$i_q = f_q(\lambda_d, \lambda_q, \theta) \tag{5.2.2b}$$

Table 5.3: Relationship Between Phase Current Fourier Coefficients and dq Flux Linkages

dq quadrant	$[\lambda_d, \lambda_q \text{Wb-T}]$	$[I_{a1}, I_{b1}]$A	$[I_{a5}, I_{b5}]$A	$[I_{a7}, I_{b7}]$A	$[I_{a11}, I_{b11}]$A	$[I_{a13}, I_{b13}]$A
first	$[0.04, 0.02]$	[7.763, 12.402]	[2.274, 1.421]	[-0.753, 0.299]	[-0.392, -0.098]	[-0.098, 0.115]
second	$[-0.04, 0.02]$	[-7.763, 12.402]	[-2.274, 1.421]	[0.753, 0.299]	[0.392, -0.098]	[0.098, 0.115]
third	$[-0.04, -0.02]$	[-7.763, -12.402]	[-2.274, -1.421]	[0.753, -0.299]	[0.392, 0.098]	[0.098, -0.115]
fourth	$[0.04, -0.02]$	[7.763, -12.402]	[2.274, -1.421]	[-0.753, -0.299]	[-0.392, 0.098]	[-0.098, -0.115]

The size of the current LUTs in equation (5.2.2) can be reduced significantly if they are independent of rotor position. This can be accomplished by representing the phase currents as a vector in terms of Fourier coefficients.

Authors in [75] represented the current harmonics in the synchronous reference frame but the symmetry between the currents and flux linkages in the four quadrants could not be utilized in that case. Hence, when the LUTs in equation (5.2.2) are used in [75], they represent two dq quadrants. The required currents to be simulated in the FEA model represent two dq quadrants as well.

In order to utilize the symmetry between the phase flux linkage and phase current in the four quadrants, the harmonics of the current waveform are described in the stationary reference frame in the proposed method. This way, the currents simulated in the FEA model and LUTs represent a single dq quadrant. Therefore, the output currents from equation (5.2.2) are transformed into the stationary reference frame as shown in Step 4 in figure 5.6. The transformed uvw currents are instantaneous current values as they are a function of rotor position:

$$i_u = f_u(\lambda_d, \lambda_q, \theta) \tag{5.2.3a}$$

$$i_v = f_v(\lambda_d, \lambda_q, \theta) \tag{5.2.3b}$$

$$i_w = f_w(\lambda_d, \lambda_q, \theta) \tag{5.2.3c}$$

The phase current can be represented as a vector in terms of Fourier coefficients as shown in Step 5 in figure 5.6. In order to find the Fourier coefficients, phase u current is expressed by Fourier series as:

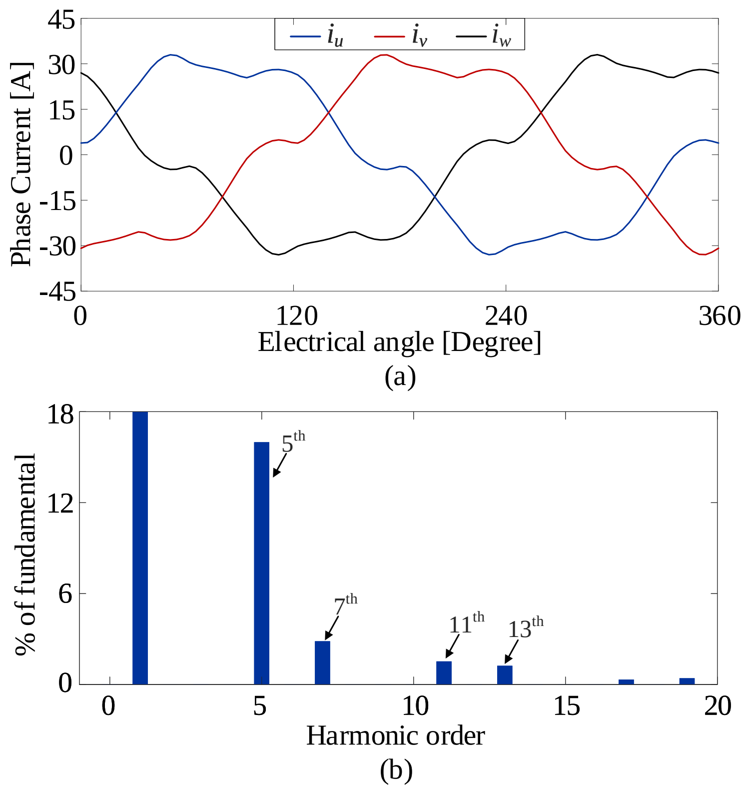

Figure 5.7: (a) 3-phase currents from equation (5.2.3) when $[\lambda_d, \lambda_q]$=[0.1, 0.03]Wb-T and (b) harmonic content

$$i_u(t) = \frac{I_o}{2} + \sum_{n=1}^{\infty}[I_{an}cos(n\theta) - I_{bn}sin(n\theta)] \tag{5.2.4}$$

where I_o is the DC component and is equal to zero for balanced current operation, ω is the angular frequency, and I_{an} and I_{bn} are the cosine and sine Fourier coefficients, respectively. These coefficients represent the magnitude and the angle of the n^{th} harmonic vector:

$$I_n = \sqrt{{I_{an}}^2 + {I_{bn}}^2} \tag{5.2.5a}$$

$$\phi_n = tan^{-1}\left(\frac{I_{bn}}{I_{an}}\right) \tag{5.2.5b}$$

where I_n and ϕ_n are the magnitude and angle of that vector. Figure 5.7 shows phase u current and its harmonic content when [λ_d, λ_q]=[0.1, 0.03]Wb-T. From figure 5.7(b), the first five dominant harmonics are considered. Thus, phase u current is expressed as:

$$\begin{aligned} I_u(t) = I_{a1}cos(\theta) + I_{a5}cos(5\theta) + I_{a7}cos(7\theta) \\ + I_{a11}cos(11\theta) + I_{a13}cos(13\theta) - I_{b1}sin(\theta) \\ - I_{b5}sin(5\theta) - I_{b7}sin(7\theta) - I_{b11}sin(11\theta) \\ - I_{b13}sin(13\theta) \end{aligned} \tag{5.2.6}$$

Hence, the relationship between the Fourier coefficients of phase current (I_{an}, I_{bn}) and the dq flux linkages (λ_d, λ_q) is represented in a 2D LUT as:

$$\sum_{n=1,5,7,11,13} I_{an} = f_{an}(\lambda_d, \lambda_q) \tag{5.2.7a}$$

$$\sum_{n=1,5,7,11,13} I_{bn} = f_{bn}(\lambda_d, \lambda_q) \tag{5.2.7b}$$

As mentioned earlier in Step 1 in figure 5.6, the flux linkage LUTs $\lambda_{dq} = f(i_d, i_q, \theta)$ and the inverted current LUTs $i_{dq} = f(\lambda_d, \lambda_q, \theta)$ are defined in the first quadrant of the synchronous reference frame, where the dq currents and the dq flux linkages have positive values. If the simulated currents in Step 1 represent the four quadrants of the synchronous reference frame, the variation of the phase current Fourier coefficients (I_{an}, I_{bn}) with the dq flux linkages (λ_d, λ_q) would be as shown in table 5.3. It can be observed that for the same magnitude of the dq flux linkages, the phase current Fourier coefficients have the same magnitude. Furthermore, the sign of I_{an} depends of the sign of λ_d and the sign of I_{bn} depends of the sign of λ_q. This is due to the symmetry between the currents and flux linkages as described earlier. This symmetry can be observed from figure 5.8, which shows the first order Fourier coefficients of the phase current with respect to dq flux linkages. The symmetry exists for other harmonics as well and they are shown at the end of this thesis in the Appendix. Therefore, equation (5.2.7) can be modified to represent all dq quadrants as:

$$\sum_{n=1,5,7,11,13} I_{an} = f_{an}(|\lambda_d|, |\lambda_q|)\ sign(\lambda_d) \tag{5.2.8a}$$

$$\sum_{n=1,5,7,11,13} I_{bn} = f_{bn}(|\lambda_d|, |\lambda_q|)\ sign(\lambda_q) \tag{5.2.8b}$$

After calculating the Fourier coefficients of phase u current, the 3-phase currents are expressed as:

$$i_u = \sum_{\substack{n=1,5,\\7,11,13}} \left[I_{an}cos(n\theta) - I_{bn}sin(n\theta)\right] \tag{5.2.9}$$

$$i_v = \sum_{\substack{n=1,5,\\7,11,13}} \left[I_{an}cos(n(\theta - \frac{2\pi}{3})) - I_{bn}sin(n(\theta - \frac{2\pi}{3}))\right] \tag{5.2.10}$$

$$i_w = \sum_{\substack{n=1,5,\\7,11,13}} \left[I_{an}cos(n(\theta + \frac{2\pi}{3})) - I_{bn}sin(n(\theta + \frac{2\pi}{3}))\right] \tag{5.2.11}$$

In the proposed method, there are 5 harmonic orders considered in the stationary frame which are the 1st, 5th, 7th, 11th, and 13th where each component requires two LUTs independent of the rotor position: one LUT for the sine coefficient and another LUT for the cosine coefficient. Hence, the total number of LUTs is 10. If the LUTs described the current harmonics in the synchronous reference frame as in [25], then the 1st order harmonic will be transformed into the DC value, the 5th and 7th order

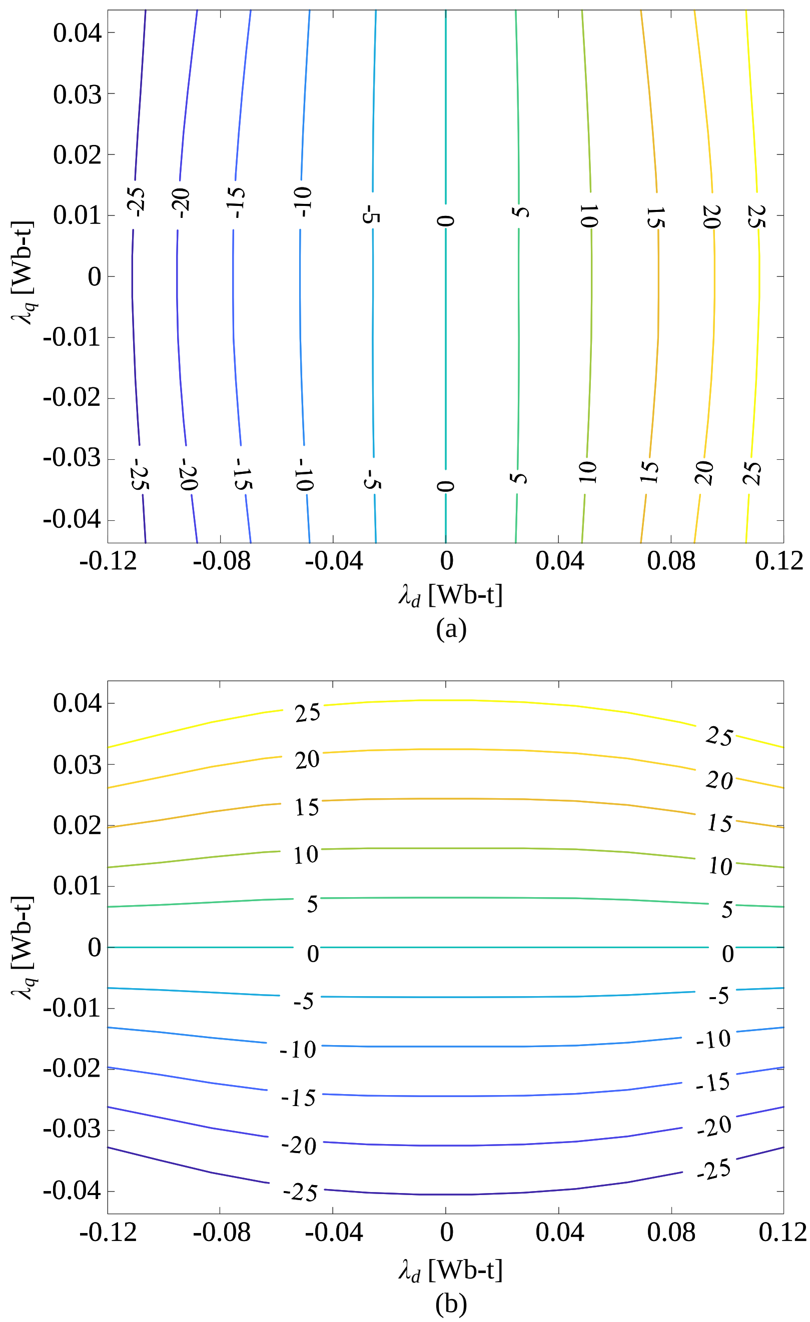

Figure 5.8: Symmetry of the first order Fourier coefficients of phase current with respect to dq flux linkages among the four quadrants of the synchronous reference frame: (a) I_{a1} and (b) I_{b1}.

harmonics will be transformed into the 6th order harmonic, and finally the 11th and 13th order harmonics will be transformed into the 12th order harmonic:

$$i_d(t) = i_{do} + i_{d,a6}cos(6\theta) - i_{d,b6}sin(6\theta) + i_{d,a12}cos(12\theta) - i_{d,b12}sin(12\theta) \tag{5.2.12}$$

$$i_q(t) = i_{qo} + i_{q,a6}cos(6\theta) - i_{q,b6}sin(6\theta) + i_{q,a12}cos(12\theta) - i_{q,b12}sin(12\theta) \tag{5.2.13}$$

Where $i_{d,a6}$ and $i_{d,b6}$ are the cosine and sine Fourier coefficients of the 6^{th} order harmonic of d-axis current, and likewise for $i_{d,a12}$, $i_{d,b12}$, $i_{d,a18}$ and $i_{d,b18}$. Similarly, $i_{q,a6}$ and $i_{q,b6}$ are the cosine and sine Fourier coefficients of the 6^{th} order harmonic of q-axis current, and likewise for $i_{q,a12}$, $i_{q,b12}$, $i_{q,a18}$ and $i_{q,b18}$. Those Fourier coefficients can be represented in 2D LUTs as [75]:

$$i_{d,o} = f_{d,o}(\lambda_d, \lambda_q) \tag{5.2.14a}$$

$$i_{q,o} = f_{q,o}(\lambda_d, \lambda_q) \tag{5.2.14b}$$

$$\sum_{n=6,12} i_{d,an} = f_{d,an}(\lambda_d, \lambda_q) \tag{5.2.14c}$$

$$\sum_{n=6,12} i_{d,bn} = f_{d,bn}(\lambda_d, \lambda_q) \tag{5.2.14d}$$

$$\sum_{n=6,12} i_{q,an} = f_{q,an}(\lambda_d, \lambda_q) \tag{5.2.14e}$$

$$\sum_{n=6,12} i_{q,bn} = f_{q,bn}(\lambda_d, \lambda_q) \tag{5.2.14f}$$

Hence, the total number of LUTs in [75] is 10 (identical to the proposed method). However, by describing the current harmonics in the synchronous reference frame as in [75], the symmetry between the four quadrants in SRM cannot be utilized, thus, the size of the LUTs and FEA characterization have to cover two quadrants in the synchronous reference frame. In contrast, the proposed method requires a single quadrant only

5.2.2 Modeling of the electro-magnetic torque

In Step 1 in figure 5.6, a 3D LUT is generated from the FEA model representing the electro-magnetic torque as a function of the dq currents and rotor position, $T_e = f(i_d, i_q, \theta)$. Unlike the flux linkage LUTs, there is no need to invert the torque LUT. The torque LUT describe the instantaneous values of the electro-magnetic torque as it is a function of rotor position. Similar to the phase current LUTs, the torque LUT can be simplified significantly if it is independent of rotor position. For this purpose, the Fourier coefficients of the torque waveform are found as shown in Step 6 in figure 5.6. Figure 5.9 shows the FEA results of the torque waveform and its harmonic content when $[i_d, i_q] = [4, 16]$A. Based on figure 5.9(b), the torque waveform can be expressed as:

$$T_e(t) = T_o + \sum_{\substack{n=6,12,\\18,24,30}} [T_{an}cos(n\theta) - T_{bn}sin(n\theta)] \tag{5.2.15}$$

$$\begin{aligned} T_e(t) = T_o &+ T_{a6}cos(6\theta) + T_{a12}cos(12\theta) \\ &+ T_{a18}cos(18\theta) + T_{a24}cos(24\theta) \\ &+ T_{a30}cos(30\theta) - T_{b6}sin(6\theta) \\ &- T_{b12}sin(12\theta) - T_{b18}sin(18\theta) \\ &- T_{b24}sin(24\theta) - T_{b30}sin(30\theta) \end{aligned} \tag{5.2.16}$$

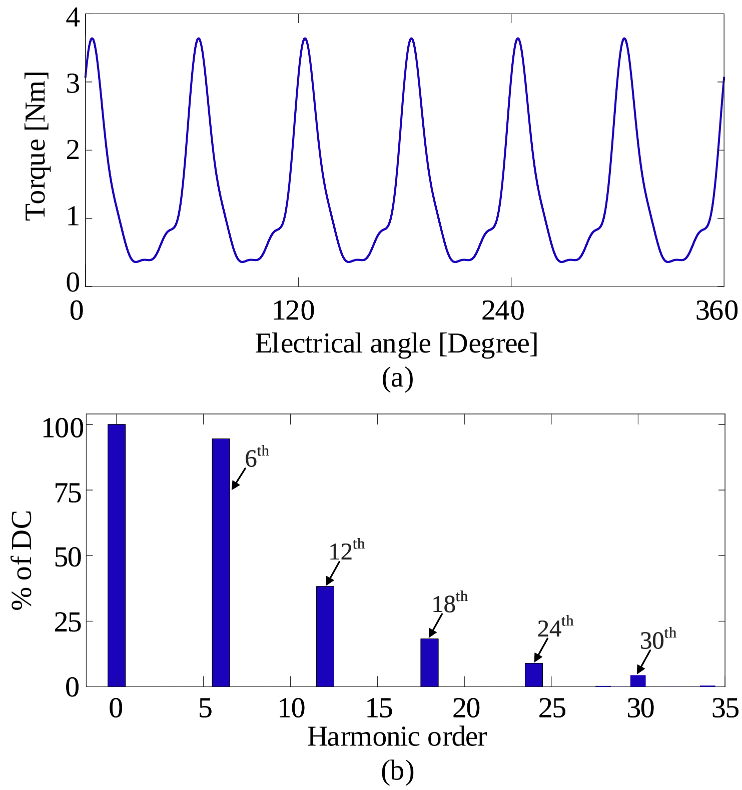

Figure 5.9: (a) electro-magnetic torque waveform when $[i_d, i_q]$=$[4, 16]$A and (b) its harmonic content

where T_o is the average torque value, and T_{a6} and T_{b6} are the Fourier coefficients of the 6^{th} order harmonic. T_{a12} and T_{b12} are the Fourier coefficients of the 12^{th} order harmonic, and likewise for the 18^{th}, 24^{th}, 30^{th} order harmonics. T_o can be calculated analytically as:

$$T_o = \frac{3}{2}p(\lambda_{do}i_q - \lambda_{qo}i_d) \tag{5.2.17}$$

where p is the number of pole pairs, i_d and i_q are the dq currents, λ_{do} and λ_{qo} are the fundamental d- and q- axis flux linkages. However, the calculation of the average torque by equation (5.2.17) requires two LUTs of the fundamental d- and q- axis flux linkages as a function of dq currents: $\lambda_{do} = f(i_d, i_q), \lambda_{qo} = f(i_d, i_q)$. Instead, the average torque can be found through a single LUT that has dq currents as inputs:

$$T_o = f(i_d, i_q) \tag{5.2.18}$$

The 6^{th}, 12^{th}, 18^{th}, 24^{th} and 30^{th} order harmonics in equation (5.2.16) are responsible for torque ripple and they are also modeled as a function of dq currents as:

$$\sum_{\substack{n=6,12,18,\\24,30}} T_{an} = f_{an}(i_d, i_q) \tag{5.2.19a}$$

$$\sum_{\substack{n=6,12,18,\\24,30}} T_{bn} = f_{bn}(i_d, i_q) \tag{5.2.19b}$$

Table 5.4 shows the variation of the average torque and torque Fourier coefficients in the four dq quadrants for the same magnitude of dq currents.

Table 5.4: Relationship Between Torque Fourier Coefficients and dq Currents

dq quadrant	$[i_d, i_q]$A	T_o Nm	$[T_{a6}, T_{b6}]$Nm	$[T_{a12}, T_{b12}]$Nm	$[T_{a18}, T_{b18}]$Nm	$[T_{a24}, T_{b24}]$Nm	$[T_{a30}, T_{b30}]$Nm
first	$[4, 16]$	1.44	[1.228, -0.590]	[0.304, -0.460]	[0.179, -0.235]	[0.056, -0.117]	[0.031, -0.060]
second	$[-4, 16]$	-1.44	[-1.228, -0.590]	[-0.304, -0.460]	[-0.179, -0.235]	[-0.056, -0.117]	[-0.031, -0.060]
third	$[-4, -16]$	1.44	[1.228, -0.590]	[0.304, -0.460]	[0.179, -0.235]	[0.056, -0.117]	[0.031, -0.060]
fourth	$[4, -16]$	-1.44	[-1.228, -0.590]	[-0.304, -0.460]	[-0.179, -0.235]	[-0.056, -0.117]	[-0.031, -0.060]

It reveals that the average torque has the same magnitude in the four dq quadrants. Additionally, the average torque is positive in the first and third dq quadrants (i.e., when i_d and i_q have the same sign) since they represent the motoring mode of operation. The average torque is negative in the second and fourth quadrants (i.e., when the i_d and i_q have different signs) as they represent the generating mode. The symmetry of the average torque for the entire operating range of dq currents is shown in figure 5.10, that figure also shows that the average torque is zero when i_d or i_q is zero, or both of them are zeros.

It can also be concluded from table 5.4 that the torque Fourier coefficients T_{an} and T_{bn} have the same magnitude for the same magnitudes of dq currents. Additionally, the sign of T_{an} depends on the sign of both d- and q- axis currents, while the sign of T_{bn} does not depend on the sign of either d- or q- axis currents. Figure 5.11 shows the symmetry of the 6^{th} order Fourier coefficients for the operating range of dq currents among the four dq quadrants. The symmetry also applies to the other Fourier coefficients of the torque harmonics and they are shown in the chapter B. Therefore, equation (5.2.18) and equation (5.2.19) are updated to represent the four dq quadrants as:

$$T_o = f(|i_d|, |i_q|)\ sign(i_d i_q) \tag{5.2.20a}$$

$$\sum_{\substack{n=6,12,18,\\24,30}} T_{an} = f_{an}(|i_d|, |i_q|)\ sign(i_d i_q) \tag{5.2.20b}$$

$$\sum_{\substack{n=6,12,18,\\24,30}} T_{bn} = f_{bn}(|i_d|, |i_q|) \tag{5.2.20c}$$

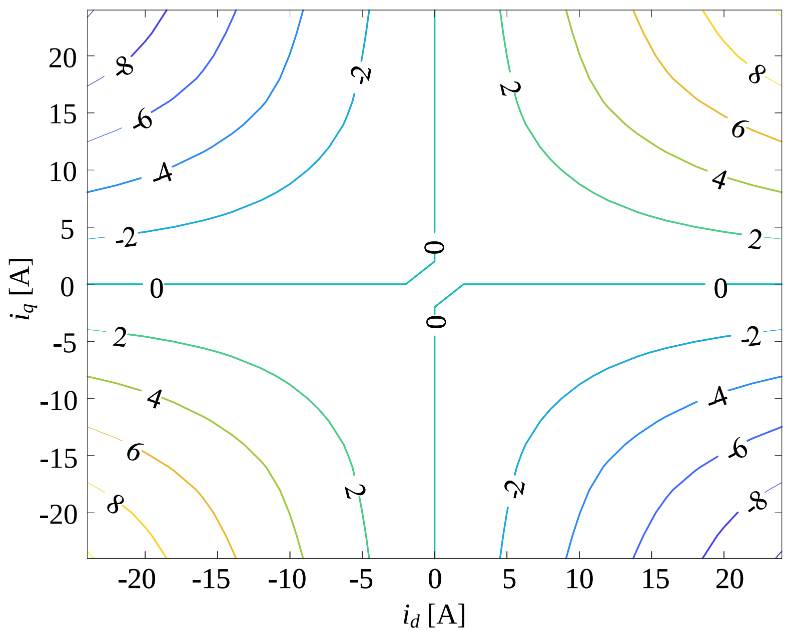

Figure 5.10: Symmetry of the average torque T_o with respect to dq currents among four quadrants of the synchronous reference frame

5.2.3 Final Model

that is based on 3-phase sinusoidal current excitation. The proposed dynamic model can describe sinusoidal and non-sinusoidal current waveforms as long as the summation of phase currents is zero, or the zero-sequence component is zero. Figure 5.12 shows the block diagram of the proposed dynamic model. The 3-phase flux linkages are calculated and transformed into synchronous reference frame. Then, the dq flux linkages are input to the current LUTs in equation (5.2.8) to estimate the phase current Fourier coefficients. The rotor position θ, and phase current Fourier coefficients are input to equation (5.2.9), equation (5.2.10) and equation (5.2.11) to calculate the instantaneous 3-phase currents. In order to model the instantaneous electro-magnetic torque, the 3-phase currents are transformed into synchronous reference frame to estimate the torque Fourier coefficients from their respective LUTs in equation (5.2.20).

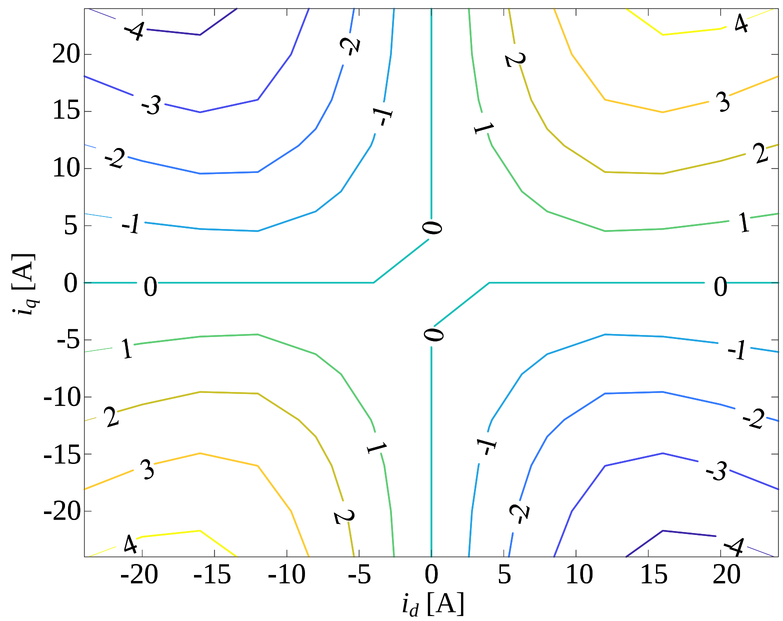

(a)

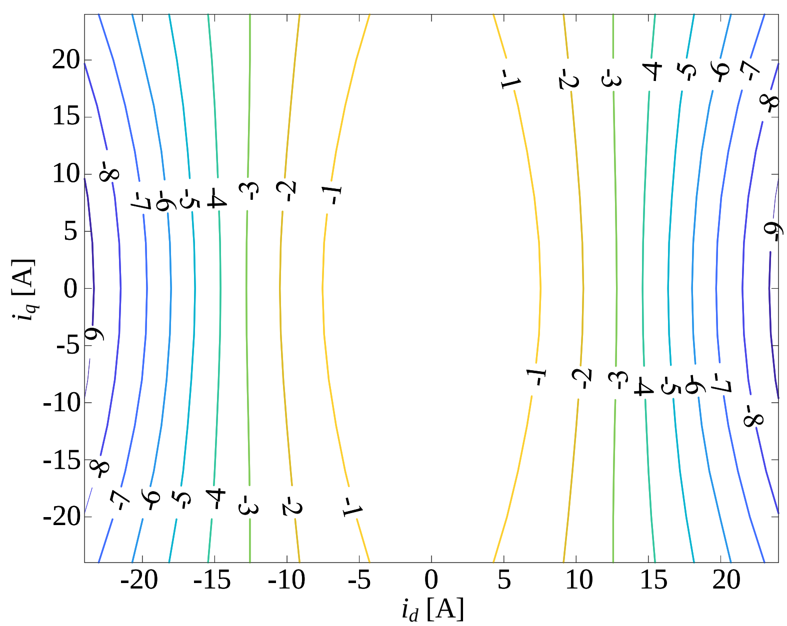

(b)

Figure 5.11: Symmetry of the 6^{th} order Fourier coefficients of electro-magnetic torque with respect to dq currents among the four quadrants of the synchronous reference frame: (a) T_{a6} and (b) T_{b6}.

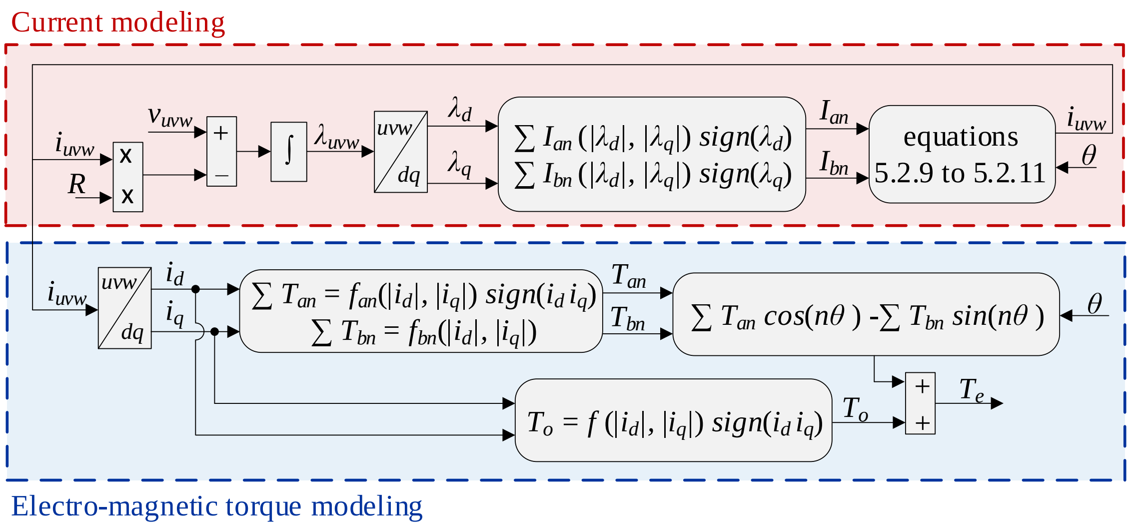

Figure 5.12: Block diagram of the proposed dynamic modeling method

The instantaneous torque is then calculated by adding the average torque and the torque harmonics together at a given rotor position as shown in equation (5.2.16).

5.3 FEA Validation

The FEA model is used to validate that the proposed method can model the operation in all dq quadrants by using the information from a single dq quadrant. Three different approaches are considered for FEA validation. In the first approach, the output 3-phase currents from the proposed dynamic model are obtained for constant dq flux linkages, for instance $[\lambda_d, \lambda_q] = [-0.04, -0.02]$Wb-T, which indicate sinusoidal phase flux linkages. These output 3-phase currents are essentially the currents required to generate sinusoidal flux linkages as the dq flux linkages are constant values. Then, the 3-phase currents from the proposed dynamic model are applied to the FEA model and the resulting flux linkage is compared with the sinusoidal flux linkage which was input to the proposed dynamic model. The comparison between the input and the output flux linkages are shown in figure 5.13(b). The sinusoidal flux linkages from the FEA model and the ones input into the dynamic model are in a good agreement. figure 5.13(c) compares the electro-magnetic torque from the FEA model and the proposed dynamic model. The electro-magnetic torque waveforms are also in good agreement. This validation shows that the proposed dynamic model accurately predicts the spatial harmonics of the current and torque waveforms.

In the second approach, constant dq currents are applied to the FEA model, for instance $[i_d, i_q] = [-10, 8]$A, and the corresponding phase flux linkages are obtained which are distorted waveforms. The flux linkage from the FEA model is then applied to the proposed dynamic model. If the proposed dynamic model is accurate, it should output the same current waveform which was applied to the FEA model. Figure 5.14(b) compares the sinusoidal current input to the FEA model and the current output from the proposed dynamic model. The results show a good match. Figure 5.14(c) compares the electro-magnetic torque from the FEA model and the proposed dynamic model. The electro-magnetic torque waveforms are in good agreement as well. This shows that the proposed method can accurately predict the current and torque for a distorted flux linkage input.

As mentioned before, the proposed method can model sinusoidal and non-sinusoidal current waveforms as long as the summation of phase currents is zero. In the third approach, the proposed method is validated by using trapezoidal phase current excitation. In this approach, the output 3-phase voltages from the dynamic model are applied to the FEA model. Figure 5.15 shows a good agreement between the phase currents, phase flux linkages, and electro-magnetic torque from the proposed dynamic

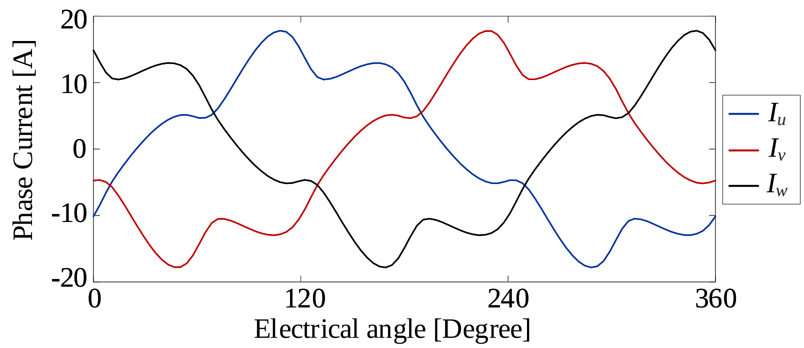

(a)

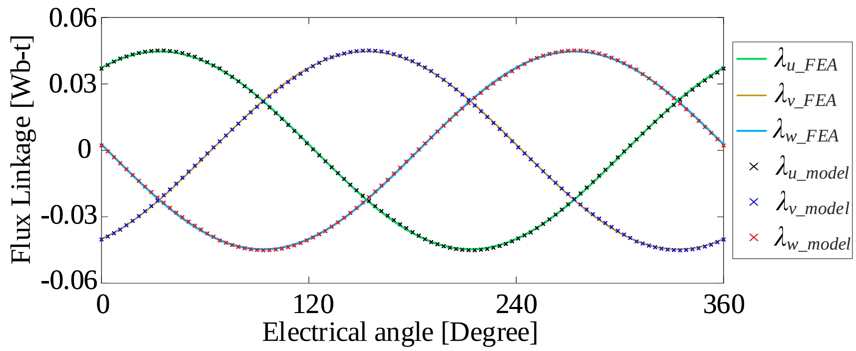

(b)

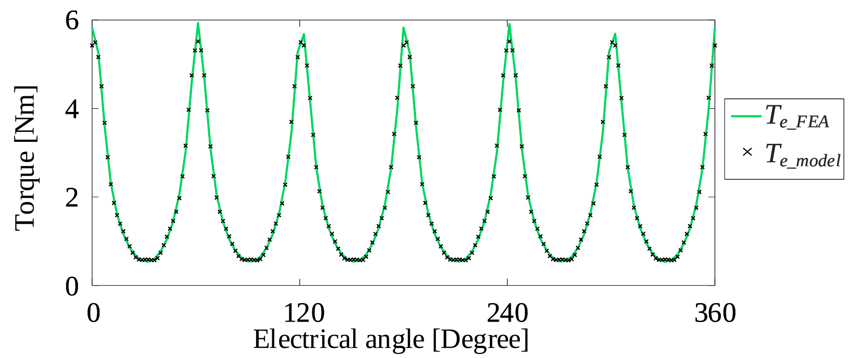

(c)

Figure 5.13: First validation approach: (a) Phase current output from the proposed dynamic model and input to the FEA model, (b) sinusoidal flux linkages from the FEA model and the proposed dynamic model, (c) electro-magnetic torque from the FEA model and the proposed dynamic model

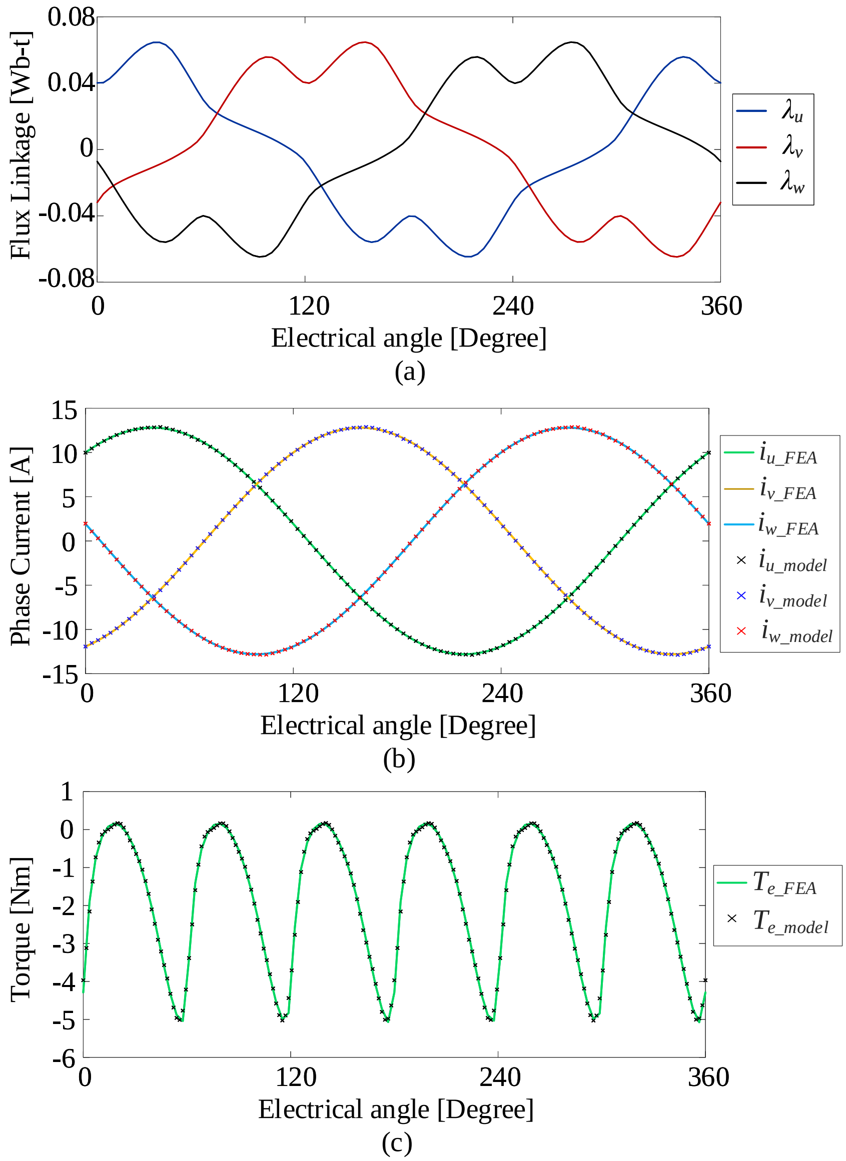

Figure 5.14: Second validation approach: (a) distorted flux linkage output from the FEA model and input to the proposed dynamic model, (b) Phase current from the FEA model and the proposed dynamic model, (c) electro-magnetic torque from the FEA model and the proposed dynamic model

model and the FEA model. It also reveals that the proposed method can model the steady state, transient, and switching dynamics. Figure 5.16 shows the distorted d- and q- axis currents corresponding to the trapezoidal current excitation shown in figure 5.15. This approach validates that the proposed method can accurately describe motor dynamics for non-sinusoidal current excitation.

It is worth mentioning that the high torque ripple in figures 5.13 to 5.15 is due to the MCSRM used in this thesis since it is designed to operate as a CSRM with single-phase excitation. SRMs which are designed to operate as MCSRM can have much lower torque ripple [30, 33, 34]

5.4 Experimental Validation

Figure 5.17 shows the experimental setup, the MCSRM is connected to an interior permanent magnet (IPM) motor, which is used as a dynamometer. Both motors are controlled using vector control and space vector modulation (SVM). The control algorithm is applied through a Texas Instrument TMS320F28377D Digital Signal Processor (DSP). The experimental drive parameters are given in table 5.5. The phase current waveforms are measured and recorded by an oscilloscope. The proposed dynamic model is validated by comparing the phase current waveforms from the experiments with those from the proposed dynamic model. The operation in the four quadrants of the synchronous reference frame are validated at different dq currents and different motor speeds. The experiments are conducted under the peak current conditions to ensure that MCSRM operates under saturation.

Figure 5.18 compares phase current waveforms in the first quadrant of the synchronous reference frame at 500 rpm for $[i_d, i_q] = [15, 10]$A. The results show a good

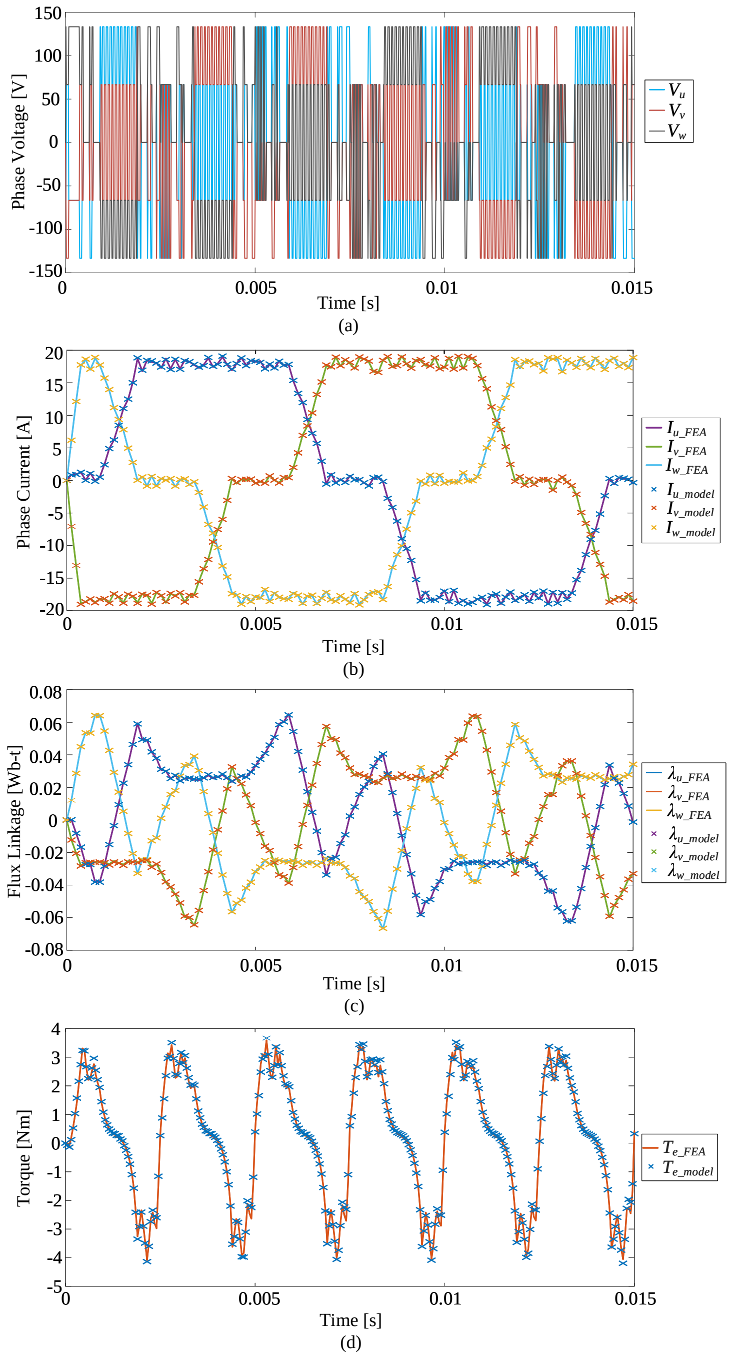

Figure 5.15: Third validation approach: (a) 3-phase voltages output from the dynamic model and input to the FEA model (b) Phase current from the FEA model and the proposed dynamic model, (c) phase flux linkage from the FEA model and the proposed dynamic model, (d) electro-magnetic torque from the FEA model and the proposed dynamic model

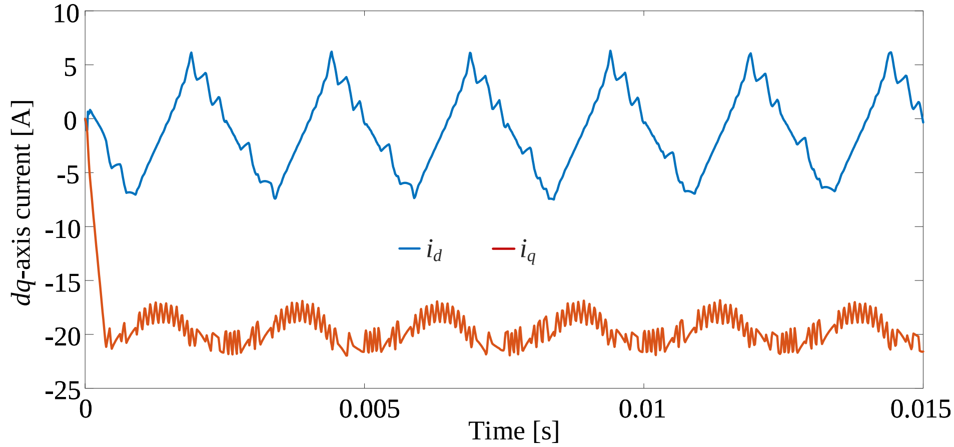

Figure 5.16: d- and q- axis currents corresponding to the trapezoidal current excitation shown in figure 5.15

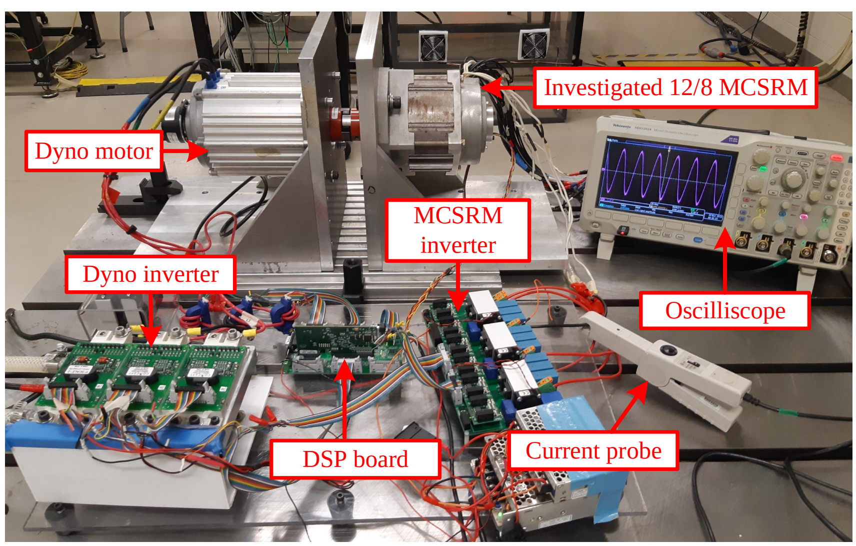

Figure 5.17: Experimental setup for the 12/8 MCSRM.

Table 5.5: Experimental drive parameters

Parameter	Value
DC link voltage	200 V
Current sampling frequency	10 kHz
Switching frequency	10 kHz
Modulation used	SVM
MCSRM current controller parameters	$K_p = 15$, $K_i = 0.1$

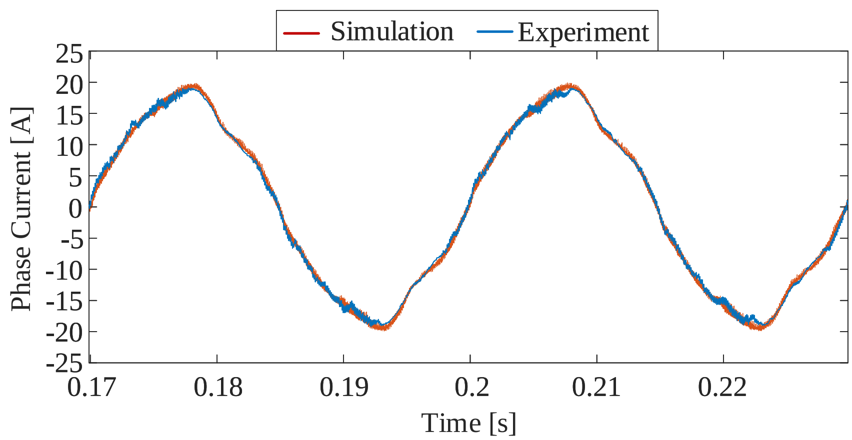

Figure 5.18: Comparison between phase current waveforms from the experiments and the proposed dynamic model when $[i_d, i_q] = [15, 10]$A at 500 rpm

match and validate that the proposed method can model the effect of saturation and spatial harmonics of the phase current.

The second quadrant operation is validated at 500 rpm for $[i_d, i_q] = [-12, 14]$A. Figure 5.19 reveals that the proposed dynamic model closely matches the experiment results. Figure 5.20 compares the phase current waveforms in the third quadrant at 1000 rpm. The dq currents in figure 5.20 are $[i_d, i_q] = [-6, -8]$A. As it can be concluded from figure 5.20, the proposed dynamic model can effectively model the operation at the third quadrant. The operation in the fourth quadrant of the synchronous reference frame is validated in figure 5.21. Again, the results show that the

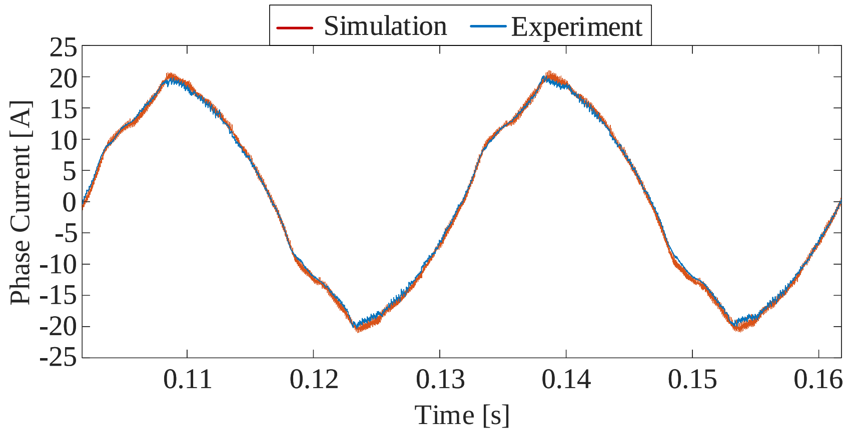

Figure 5.19: Comparison between the phase current waveforms from experiments and the proposed dynamic model when $[i_d, i_q] = [-12, 14]$A at 500 rpm

proposed dynamic model can accurately model the spatial harmonics and saturation.

Figures 5.22 and 5.23 present the validation of the proposed method at 1500 rpm. Figure 5.22(a) compares the phase current from the proposed model and experiments when $[i_d, i_q] = [-10, -5]$A and it shows a good agreement between experimental and simulation results. Figure 5.22(b) shows the distortion in the d- and q- axis currents due to the spatial harmonics. Figure 5.23(a) compares the phase current waveforms when $[i_d, i_q] = [3, 12]$A and it proves that the proposed dynamic model can describe the motor dynamics properly. Figure 5.23(b) shows the current distortion in the synchronous reference frame.

Finally, table 5.6 compares the proposed method and other methods mentioned in the literature. Table 5.6 shows the limitations of each method, the motor topology used, the maximum error in the current and torque modeling, and the validation method used. Table 5.6 reveals that the proposed method has the minimum error in current and torque modeling compared to other methods. It also shows that the

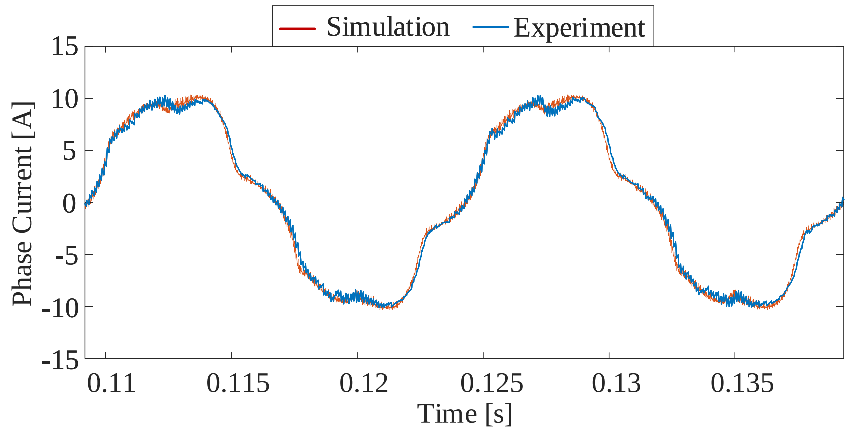

Figure 5.20: Comparison between the phase current waveforms from experiments and the proposed dynamic model when $[i_d, i_q] = [-6, -8]$A at 1000 rpm

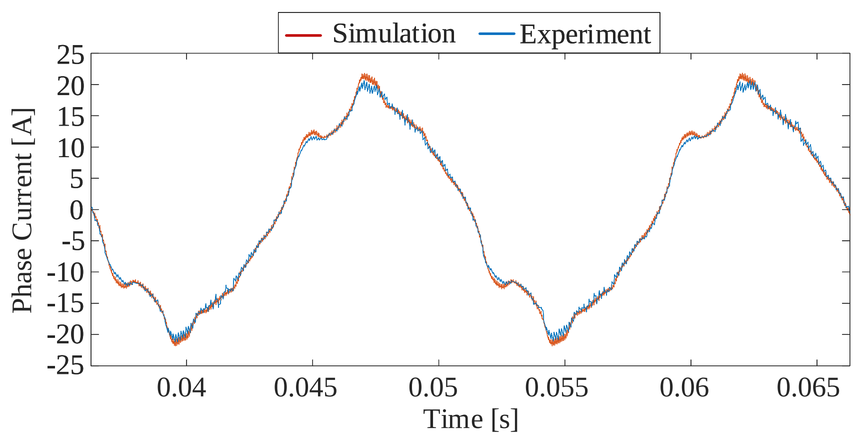

Figure 5.21: Comparison between the phase current waveforms from experiments and the proposed dynamic model when $[i_d, i_q] = [10, -15]$A at 1000 rpm

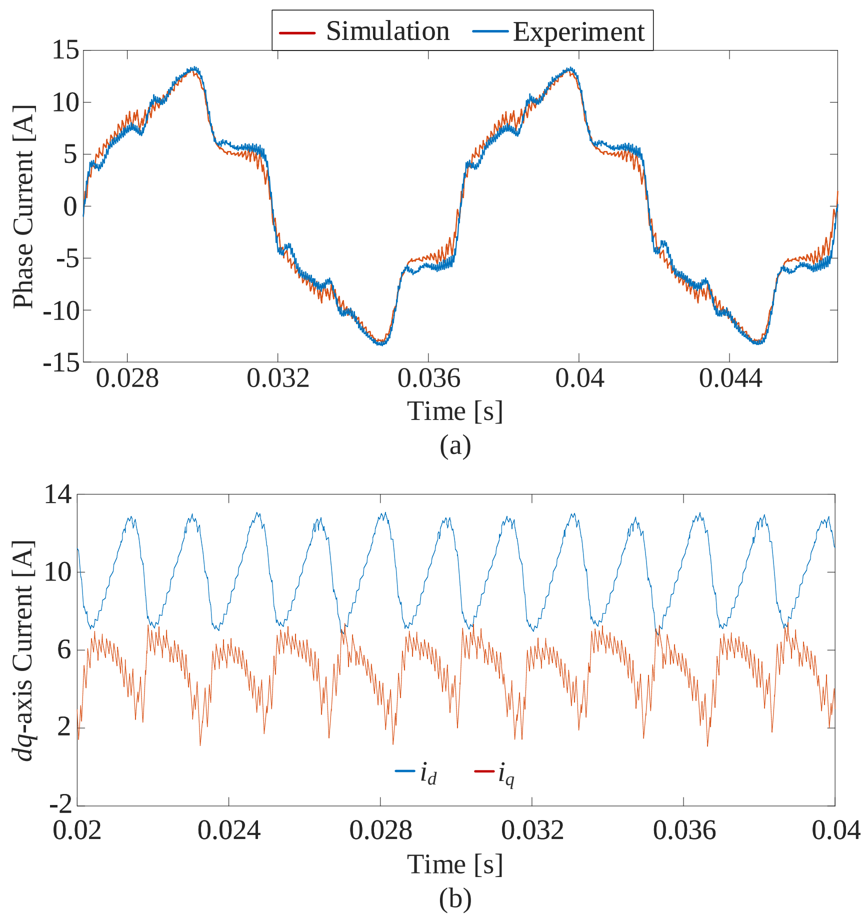

Figure 5.22: (a) Comparison between the phase current waveforms from experiments and the proposed dynamic model when $[i_d, i_q] = [-10, -5]$A at 1500 rpm, (b) the corresponding d- and q- axis currents

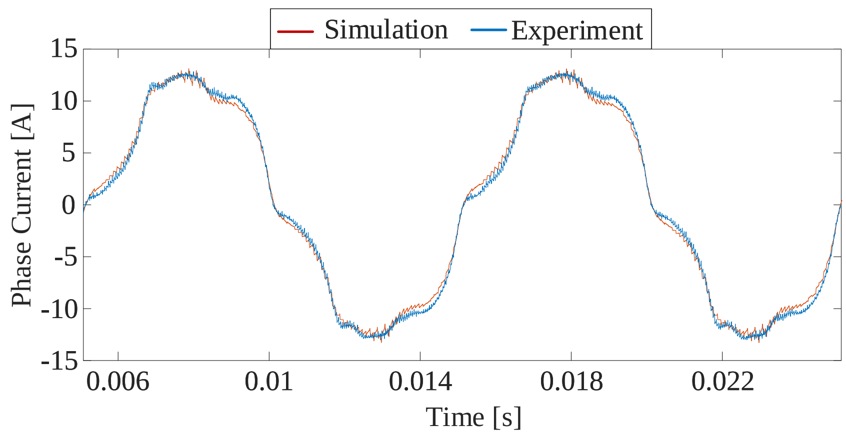

(a)

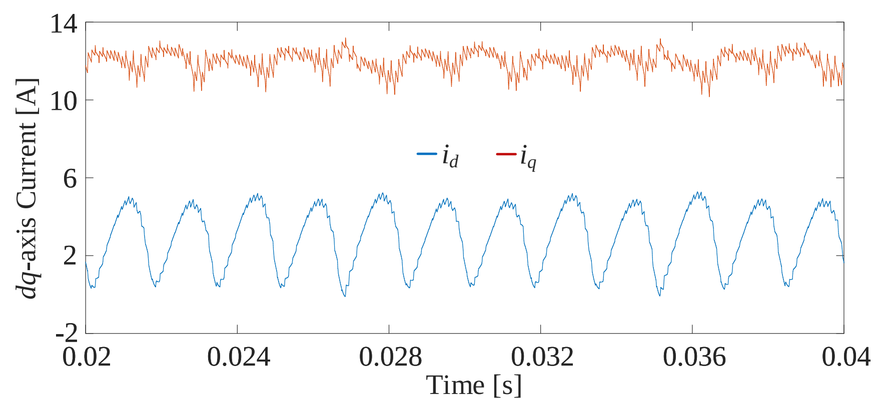

(b)

Figure 5.23: (a) Comparison between the phase current waveforms from experiments and the proposed dynamic model when $[i_d, i_q] = [3, 12]$A at 1500 rpm, (b) the corresponding d- and q- axis currents

proposed method is novel as it uses the vector representation to describe the motor dynamics.

Table 5.6: Performance Comparison Between the Proposed Method and Other Methods in Literature

Article	Modeling Method	excited phases	Method limitation	Applied motor	Current error* /Validation method	Torque error* /Validation method
[28]	Magnetic circuit modeling	2	Excited phases have equal currents	3-phase FP 6/4 MCSRM	10% /Experiments	12% /Experiments
[25]	Magnetic circuit modeling	2	Excited phases have equal currents	3-phase FP 6/4 MCSRM	23% /FEA	N/A
[80]	Instantaneous values LUT-based	2	Excited phases have equal currents	3-phase FP 12/8 MCSRM	N/A	96% /Experiments
[29]	Instantaneous values LUT-based	2	Excited phases have equal currents	3-phase FP 6/4 MCSRM	12% /Experiments	N/A
[79]	FF-ANN	2	Saturation effect is not considered	3-phase FP 6/4 MCSRM	N/A	N/A
[78]	Instantaneous values LUT-based	3	High noise in phase currents	3-phase FP 6/4 MCSRM	N/A	7% /FEA
[75]	Instantaneous values LUT-based	2 or 3	Summation of currents is zero	3-phase SP 12/8 MCSRM	27% /Experiments	N/A
Proposed method	Vector components LUT-based	2 or 3	Summation of currents is zero	3-phase SP 12/8 MCSRM	5% /Experiments	≈0% /FEA

*the current error and torque error are the maximum error and they are calculated from the simulation or experimental results of the corresponding article.

5.5 Summary

A dynamic model for mutually coupled switched reluctance machines is presented in this chapter. The proposed method utilizes two-dimensional look-up tables (LUTs), which describe a single quadrant of the *dq* synchronous reference frame. LUTs used in the proposed method represent the phase current and electro-magnetic torque as vectors in terms of Fourier coefficients. Hence, the LUTs are independent of the rotor position. Due to the absence of rotor magnets and rotor winding in MCSRMs, the magnetic flux distribution posses symmetry among the four *dq* quadrants. By utilizing this symmetry, LUTs constituting only single *dq* quadrant information need to be obtained from the FEA model. This reduces the size of the LUT and the number of FEA steps by 50%, compared to two-quadrant based models. The proposed dynamic model is validated by both FEA results and experiments, for the operations in the four *dq* quadrants at different current values and different speeds. The error in current and torque modeling between the proposed method and FEA is almost zero. Thus, the proposed method offers time efficient and accurate results that can be used to replace FEA when analysing motor performance.

Chapter 6

Model-Based Spatial Harmonics Vector Compensation Method for Three-Phase Mutually Coupled Switched Reluctance Machine With Sinusoidal Current Excitation

6.1 Introduction

Vector control is widely used in AC motors, such as synchronous and induction motors for sinusoidal current excitation where the spatial harmonics are ignored [86,87]. The spatial harmonics are due to slotting and winding distribution of the stator [88]. Vector control is usually implemented using Proportional-Integral (PI) controllers where the 3-phase sinusoidal currents are transformed into the dq synchronous reference frame as DC values (i.e., direct-and quadrature-axis currents). These DC values are controlled by two independent PI controllers where the integral gain of the PI controller eliminates the steady-state error as it provides the highest stiffness for the zero frequency disturbances [89]. For MCSRM, the salient structure of the stator and rotor poles creates considerable spatial harmonics which results in distorted phase currents [22]. When the distorted 3-phase currents are transformed into the dq synchronous reference frame, the resulting direct-and quadrature-axis currents have DC values in addition to the 6^{th}, 12^{th}, and 18^{th} order harmonics. The DC values represent the fundamental current component and they are controlled by the PI controllers. However, the harmonics in the dq synchronous frame cannot be effectively controlled by the PI controllers, as the effect of integral gain deteriorates for higher frequencies of disturbance [89]. As a result, the standard vector control with PI controllers cannot eliminate the spatial harmonics in MCSRM [90].

Several harmonic elimination methods can be used to suppress the spatial harmonics of phase currents. Most of the methods in literature are for power system application to eliminate the grid harmonics due to non-linear loads. The spatial harmonics in motor drive applications are usually ignored as they are not significant. In power system applications, the harmonics of phase current are mitigated by using

Proportional-Resonant (PR) controllers in the dq synchronous reference frame [91,92]. The PR controllers have an infinite gain at the resonant frequency. Hence, the controller is tuned to have a resonant frequency equal to the harmonic frequency, and the DC values of direct-and quadrature-axis currents are controlled by the PI controllers. The complexity of this method attributes to the high number of controllers which in turn impacts system stability and the design challenges to determine the cut-off frequency [93]. Shunt-active and passive filters are also used to eliminate current harmonics in power system applications. Shunt-active filters require an additional inverter in between the load and the AC source, that additional inverter injects current harmonics of the same magnitude and 180° phase shift electrical of the original harmonics, so that the resultant current harmonics are zero [94, 95]. These filters require additional inverter and external supply, so they are not cost-efficient solutions, in addition to the complex control. The passive filters require additional devices corresponding to each harmonic order [96].

So far, we know that the spatial harmonics are ignored in induction and synchronous machines, while they are significant in MCSRM. Additionally, the standard vector control with PI controllers cannot create sinusoidal currents in MCSRMs. Multiple PR controllers can be used with the PI controllers to eliminate the spatial harmonics. However, they are complicated in design and influence the system stability. Hence, the advantage of sinusoidal current excitation for MCSRM in terms of using a simple and robust control is extinguished, since the vector control cannot handle them. The objective of this chapter is to introduce a simple, robust, and efficient method to mitigate spatial harmonics in MCSRM without affecting system stability. The proposed method is based on calculating the required voltage harmonics to be added to the fundamental voltage component in order to generate the required sinusoidal currents, without using extra PI or PR controllers, or extra devices. The voltage harmonics are represented as vectors and they are calculated from the flux linkage harmonic vectors that are represented as Fourier coefficients. These Fourier coefficients are in the form of look-up tables (LUTs) and those LUTs are obtained from finite element analysis (FEA). The vector representation of flux linkage harmonics results in 2D LUTs independent of rotor position, which reduces the size of LUT significantly.

This chapter is organised as follows; section 6.2 presents the proposed harmonics compensation method, section 6.3 shows the validation of the proposed method using FEA ,and section 6.4 shows the validation using experiments. Finally, section 6.5 has the summary of the chapter.

6.2 The Proposed Spatial Harmonics Vector Compensation Method

In chapter 5, the focus was on the phase current and electro-magnetic torque. The focus in this chapter is on the phase flux linkage and phase voltage.

6.2.1 Flux Linkage Analysis

The output 3-phase flux linkages from the FEA model have the same waveform and are shifted 120° electrical. For instance, figure 6.1 shows the phase flux linkage and its harmonic content when direct-and quadrature-axis currents are equal to zero and 20 amps $\left([i_d, i_q]\text{=}[0,\ 20]\text{A}\right)$, respectively. It can be noticed from figure 6.1 that the

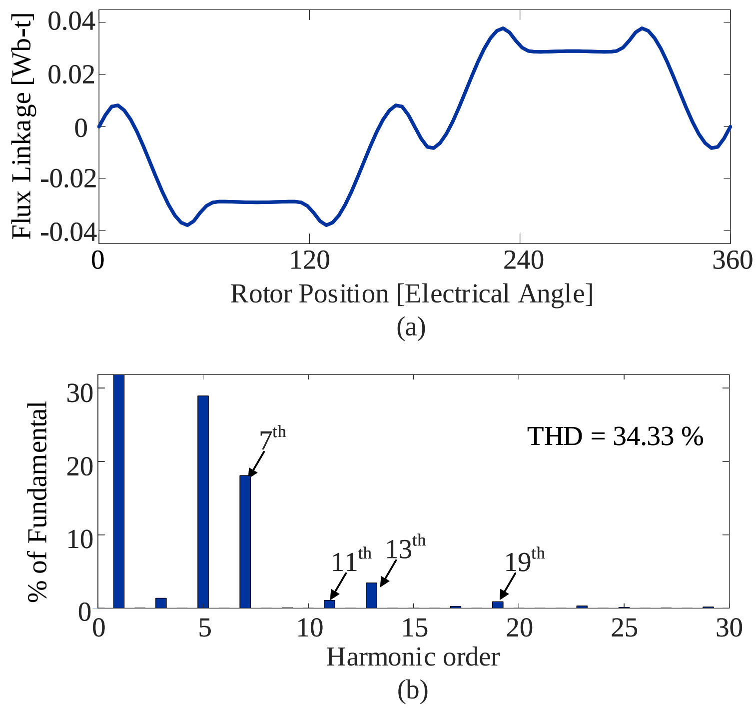

Figure 6.1: (a) Phase u flux linkage and (b) its harmonic content when $[i_d, i_q]$=$[0, 20]$A.

spatial harmonic orders are the 5^{th}, 7^{th}, 11^{th}, 13^{th}, etc. Phase u flux linkage can be expanded by Fourier series as:

$$\lambda_u(t) = \frac{\lambda_o}{2} + \sum_{n=1}^{\infty} \left[\lambda_{an} cos(n\theta) - \lambda_{bn} sin(n\theta)\right] \tag{6.2.1}$$

where λ_o is the DC offset and is equal to zero due to the sinusoidal current excitation, λ_{an} and λ_{bn} are the sine and cosine Fourier coefficients of the harmonic order n, and w is the electrical angular frequency. λ_{an} and λ_{bn} represent the flux linkage harmonic vector as:

$$\lambda_n = \sqrt{\lambda_{an}^2 + \lambda_{bn}^2} \tag{6.2.2a}$$

$$\phi_n = tan^{-1}\left(\frac{\lambda_{bn}}{\lambda_{an}}\right) \tag{6.2.2b}$$

where λ_n and ϕ_n are the magnitude and angle, respectively, of the n^{th} harmonic vector. The relationship between $\lambda_{an,bn}$ and $i_{d,q}$ is expressed as:

$$\sum_{n=1}^{\infty}\left[\lambda_{an} = f_{an}(i_d, i_q)\right] \tag{6.2.3a}$$

$$\sum_{n=1}^{\infty}\left[\lambda_{bn} = f_{bn}(i_d, i_q)\right] \tag{6.2.3b}$$

where $f_{an}(i_d, i_q)$ and $f_{bn}(i_d, i_q)$ are 2D LUTs independent of rotor position which in turn reduces the size of the LUT significantly. As I mentioned in chapter 5, there is a symmetry between current and flux linkage in the four quadrants of the dq frame, and the LUTs can represent a single quadrant. Thus, the equation (6.2.3) is modified to:

$$\sum_{n=1}^{\infty}\left[\lambda_{an} = f_{an}(|i_d|, |i_q|)\ sign(i_d)\right] \tag{6.2.4a}$$

$$\sum_{n=1}^{\infty}\left[\lambda_{bn} = f_{bn}(|i_d|, |i_q|)\ sign(i_q)\right] \tag{6.2.4b}$$

The symmetry between the direct-and quadrature-axis currents and the Fourier coefficients of the phase flux linkage is shown in chapter C.

6.2.2 Phase Voltage Analysis

The 3-phase voltages output from the FEA model are the essential voltages to create sinusoidal currents when they are applied to the motor terminals. Similar to equation (6.2.1), the phase voltage is represented by Fourier series as:

$$v_u(t) = \frac{V_o}{2} + \sum_{n=1}^{\infty} \big[V_{an} cos(n\theta) - V_{bn} sin(n\theta)\big] \tag{6.2.5}$$

where V_o is the DC offset and is equal to zero since it is a balanced 3-phase system. V_{an} and V_{bn} are the sine and cosine Fourier coefficients of the harmonic order n, and they represent the magnitude and angle of the harmonic voltage vector. The relationship between phase voltage and phase flux linkage is:

$$v_u(t) = i_u(t)R + \frac{d\lambda_u(t)}{dt} \tag{6.2.6}$$

where R is the phase resistance. With the help of (6.2.1) and (6.2.5), the relationship between $V_{an,bn}$ and $\lambda_{an,bn}$ is:

$$\begin{gathered}\sum_{n=1}^{\infty} \Bigg[V_{an} cos(n\theta) - V_{bn} sin(n\theta) = \\ I_{an} R cos(n\theta) - I_{bn} R sin(n\theta) + \frac{d\big(\lambda_{an} cos(n\theta) - \lambda_{bn} sin(n\theta)\big)}{dt}\Bigg]\end{gathered} \tag{6.2.7}$$

where I_{an} and I_{bn} are the sine and cosine Fourier coefficients, respectively, of the phase current. The fundamental voltage component is found by setting the harmonic order n to 1:

$$\begin{gathered} V_{a1}cos(\theta) - V_{b1}sin(\theta) = \\ I_{a1}Rcos(\theta) - I_{b1}sin(\theta) - \lambda_{b1}wcos(\theta) - \lambda_{a1}wsin(\theta) \end{gathered} \tag{6.2.8}$$

By considering the coefficients of the same trigonometric function in equation (6.2.8), the Fourier coefficients of the fundamental voltage vector are:

$$V_{a1} = I_{a1}R - \lambda_{b1}\omega \tag{6.2.9a}$$

$$V_{b1} = I_{b1}R + \lambda_{a1}\omega \tag{6.2.9b}$$

The fundamental voltage component is not enough to create sinusoidal currents in MCSRM. Hence, the Fourier coefficients of the harmonic voltage vectors, $\sum_{n=2}^{\infty}(V_{an}, V_{bn})$, are calculated from flux linkage harmonics. Thus, voltage harmonics are expressed as:

$$\sum_{n=2}^{\infty}\Big[V_{an}cos(n\theta) - V_{bn}sin(n\theta) = -\lambda_{bn}nwcos(n\theta) - \lambda_{an}nwsin(n\theta)\Big] \tag{6.2.10}$$

The harmonics of phase current do not exist in (6.2.10) as the FEA model is based on sinusoidal current excitation. By considering the coefficients of the same trigonometric function in equation (6.2.10), the Fourier coefficients of the harmonic voltage vectors are calculated as:

$$\sum_{n=2}^{\infty}\Big[V_{an} = -\lambda_{bn}n\omega\Big] \tag{6.2.11a}$$

$$\sum_{n=2}^{\infty}\Big[V_{bn} = \lambda_{an}n\omega\Big] \tag{6.2.11b}$$

Equation (6.2.11)) shows that the Fourier coefficients of the harmonic voltage vectors (V_{an} and V_{bn}) are the multiplication of the flux linkage Fourier coefficients (λ_{an} and λ_{bn}), the electrical angular frequency (w), and the harmonic order (n). As a result, the dominant spatial harmonics of the phase voltage have higher orders than the flux linkage. Figure 6.2 shows the phase voltage from the FEA model when $[i_d, i_q] = [0, 20]$A. As it can be noticed from figure 6.2, the phase voltage has dominant harmonic orders (around 10% of the fundamental) up to the 19^{th} order. As a result, the LUTs in equation (6.2.4) should consider the harmonic components up to the 19^{th} order harmonic:

$$\sum_{n=5,7,11}^{13,17,19} \left[\lambda_{an} = f_{an}(|i_d|, |i_q|)\ sign(i_d)\right] \tag{6.2.12a}$$

$$\sum_{n=5,7,11}^{13,17,19} \left[\lambda_{bn} = f_{bn}(|i_d|, |i_q|)\ sign(i_q)\right] \tag{6.2.12b}$$

Then the harmonic voltage vectors are calculated up to the 19^{th} order harmonic:

$$\sum_{n=5,7,11}^{13,17,19} \left[V_{an} = -\lambda_{bn} n\omega\right] \tag{6.2.13a}$$

$$\sum_{n=5,7,11}^{13,17,19} \left[V_{bn} = \lambda_{an} n\omega\right] \tag{6.2.13b}$$

After obtaining the harmonic voltage vectors from (6.2.13). The next section discusses the integration of the proposed method with the standard vector control.

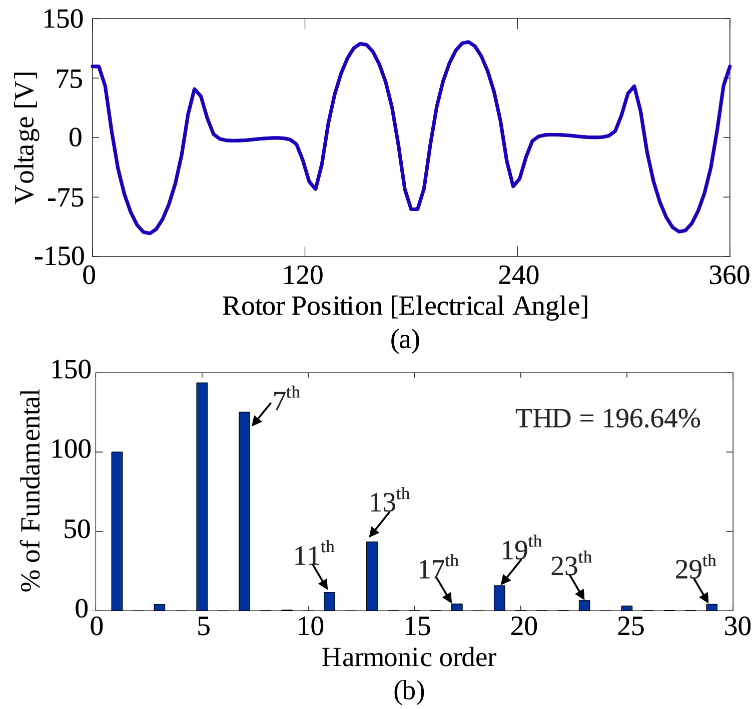

Figure 6.2: (a) Phase u voltage and (b) its harmonic content spectrum when $[i_d, i_q] = [0, 20]$A.

6.2.3 Integration of The Proposed Method With The Standard Vector Control

The integration of the proposed harmonics compensation method and the standard vector control is shown in figure 6.3. The model in figure 6.3 has two parts, the first part is the standard vector control which consists of two PI controllers, and the second part is the proposed harmonics compensation method. The PI controllers output the direct-and quadrature-axis voltages, v_{do} and v_{qo}, corresponding to the fundamental voltage component, v_{u1}. The relationship between $v_{do,qo}$ and v_{u1} is expressed by Park-Clarke transformation as [97]:

$$v_{u1}(t) = v_{do}cos(\theta) - v_{qo}sin(\theta) \tag{6.2.14}$$

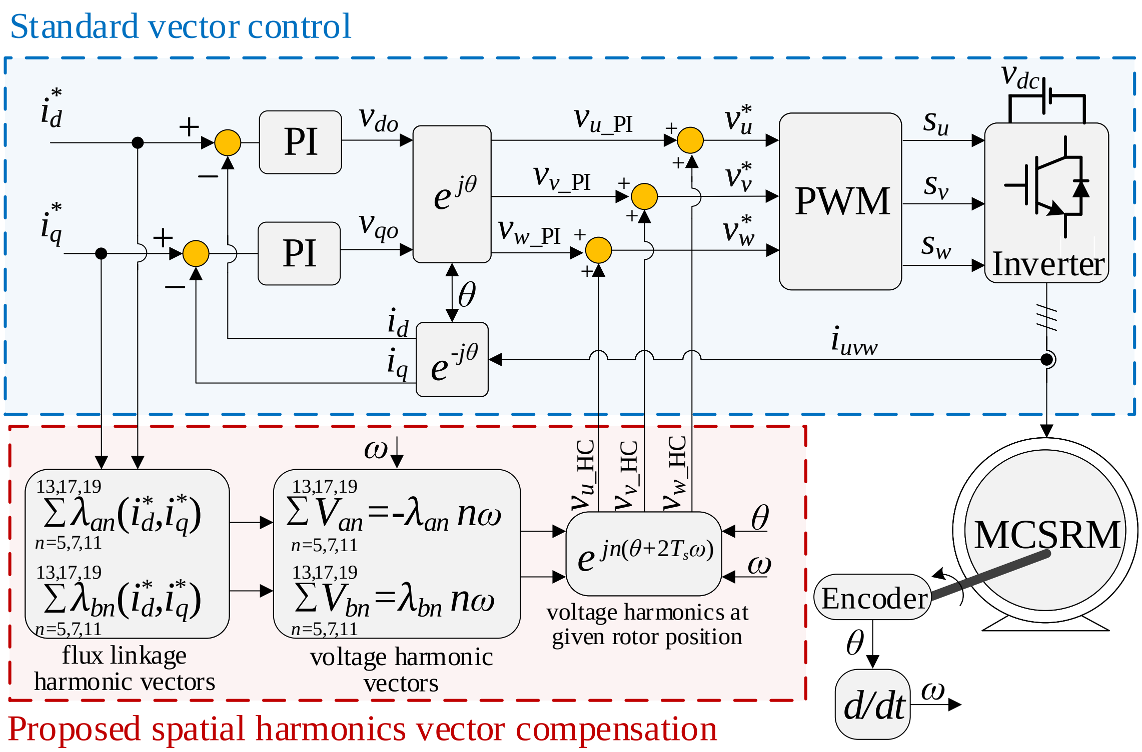

Figure 6.3: The proposed spatial harmonics compensation method integrated with the standard vector control for a 3-phase MCSRM.

v_{do} and v_{qo} can also be expressed in the dq synchronous reference frame as:

$$v_{do} = \underbrace{i_d R - \lambda_{qo}\omega}_{\substack{\text{during steady-state} \\ \text{operation (6.2.9(a))}}} + \underbrace{L_d \frac{di_d}{dt}}_{\substack{\text{during transient} \\ \text{operation}}} \tag{6.2.15a}$$

$$v_{qo} = \underbrace{i_q R + \lambda_{do}\omega}_{\substack{\text{during steady-state} \\ \text{operation (6.2.9(b))}}} + \underbrace{L_q \frac{di_q}{dt}}_{\substack{\text{during transient} \\ \text{operation}}} \tag{6.2.15b}$$

where L_d and Lq are the direct-and quadrature-axis inductances, respectively. λ_{do} and λ_{qo} are the direct-and quadrature-axis flux linkages corresponding to the fundamental flux linkage component. Therefore, the PI controllers regulate the resistive voltage drop and the first order component of the induced electro-motive force (emf), $\lambda_{do}w$ and $\lambda_{qo}w$, at the steady-state operation, in addition to $L_d\frac{di_d}{dt}$ and $L_q\frac{di_q}{dt}$ at the transient operation.

The PI controllers in figure 6.3 are within a closed-loop of current error feedback, while the harmonic compensation method is an open-loop system. Therefore, the stability of the closed-loop system depends on the PI controllers only and not on the proposed compensation method. The stability of the PI controllers depends on the proportional and integral gains and they are selected based on pole-zero cancellation [98] as:

$$k_{p,d} = 2\pi f_{bw} L_d, \quad k_{p,q} = 2\pi f_{bw} L_q \tag{6.2.16a}$$

$$k_i = 2\pi f_{bw} R \tag{6.2.16b}$$

where k_p and k_i are the proportional and integral gains of the PI controller, respectively, and f_{bw} is the bandwidth frequency of the PI controller. The higher bandwidth results in faster response but it can also lead to instability for finite sampling. The maximum value of f_{bw} is usually 1/10 of the switching frequency [99] to avoid oscillatory behaviour or unstable operation. Hence, the controller gains at 10 kHz switching frequency are:

$$k_{p,d} = 30, \quad k_{p,q} = 12 \tag{6.2.17a}$$

$$k_{i,dq} = 1800 \tag{6.2.17b}$$

As mentioned earlier, the fundamental phase voltage, v_{u1}, is not enough to create the reference sinusoidal currents, therefore, the associated voltage harmonics are calculated and provided by the proposed method. The proposed method receives the reference direct-and quadrature-axis currents and estimates the flux linkage harmonic vectors in terms of λ_{an} and λ_{bn} from equation (6.2.12), then the associated voltage harmonic vectors represented by V_{an} and V_{bn} are calculated based on equation (6.2.13). Afterwards, the instantaneous value of the voltage harmonic vectors are calculated at a given rotor position. For instance, at a sampling time t_k, the rotor position feedback θ_k is used to calculate the instantaneous values of the voltage harmonics. Then, the updated duty cycle is applied at the next time instant t_{k+1}. Additionally, the phase currents will reach the reference values after another sampling period at t_{k+2} [100, 101]. Therefore, in order to compensate this delay, rotor position after 2 sampling periods is predicted as:

$$\theta_{k+2} = \theta_k + 2\Delta\theta, \quad \Delta\theta = wT_s \tag{6.2.18}$$

where T_s is the reciprocal of sampling frequency. The resultant phase voltage is the summation of the PI controllers output and voltage harmonics calculated by the proposed method:

$$v_u(t) = \underbrace{v_{do}cos(\theta) - v_{qo}sin(\theta)}_{\substack{\text{regulated by the PI} \\ \text{controllers, } v_{u,v,w\_\text{PI}}}} + \underbrace{\sum_{n=5,7,11}^{13,17,19} [V_{an}cos(n\theta) - V_{bn}sin(n\theta)]}_{\substack{\text{provided by the proposed harmonic} \\ \text{compensation method, } v_{u,v,w\_\text{HC}}}} \tag{6.2.19}$$

The output voltage from the PI controllers is denoted as v_{u,v,w_PI} and the voltage harmonics provided by the proposed method are referred to as v_{u,v,w_HC}, as depicted in figure 6.3. The summation of v_{u,v,w_PI} and v_{u,v,w_HC} is the reference 3-phase voltages, $v^*_{u,v,w}$. If space voltage modulation (SVM) is used, then $v^*_{u,v,w}$ are transformed into alpha-beta stationary frame and the transformed voltages are input into SVM. If sinusoidal pulse width modulation (SPWM) is used, there is no need to perform alpha-beta transformation and $v^*_{u,v,w}$ are input into the SPWM.

6.3 Simulation Results and FEA Validation

The dynamic model introduced in chapter 5 is used and the simulation parameters are shown in table 6.1. Figure 6.4(a)-(d) compares the phase current at 1500 rpm when the reference direct-and quadrature-axis currents are 10A and 5A ($[i^*_d, i^*_q]$=$[10, 5]$A), respectively, using the standard vector control with and without the proposed method. Figure 6.4(a)-(b) shows that the THD of the phase current without using the proposed method is 16% due to the large magnitude of spatial harmonics. For instance, the magnitude of the 5^{th} and 7^{th} order harmonics is 15% and 7% of the fundamental component, respectively. The THD of the phase current is reduced to 2% with using the proposed method and the percentage of the spatial harmonics is suppressed to less than 2%, as depicted in figure 6.4(c)-(d). Please note that if one of the six voltage harmonics was not injected, that harmonic order will exist in the phase current. For instance, if the 5^{th} harmonic order of the phase voltage was not injected, then the phase current will contain the 5^{th} harmonic order.

Figure 6.4(e)-(f) shows the phase current waveform with using the hysteresis current control (HCC) at the same testing conditions. The sampling frequency is increased to 20 kHz to keep the maximum switching frequency as 10 kHz when the HCC is used. The hard switching of HCC (i.e., the applied phase voltage is either positive or negative the DC link voltage) results in high current ripple as it can be noticed in figure 6.4(e). Thus, the THD of the phase current is 28%. Please note

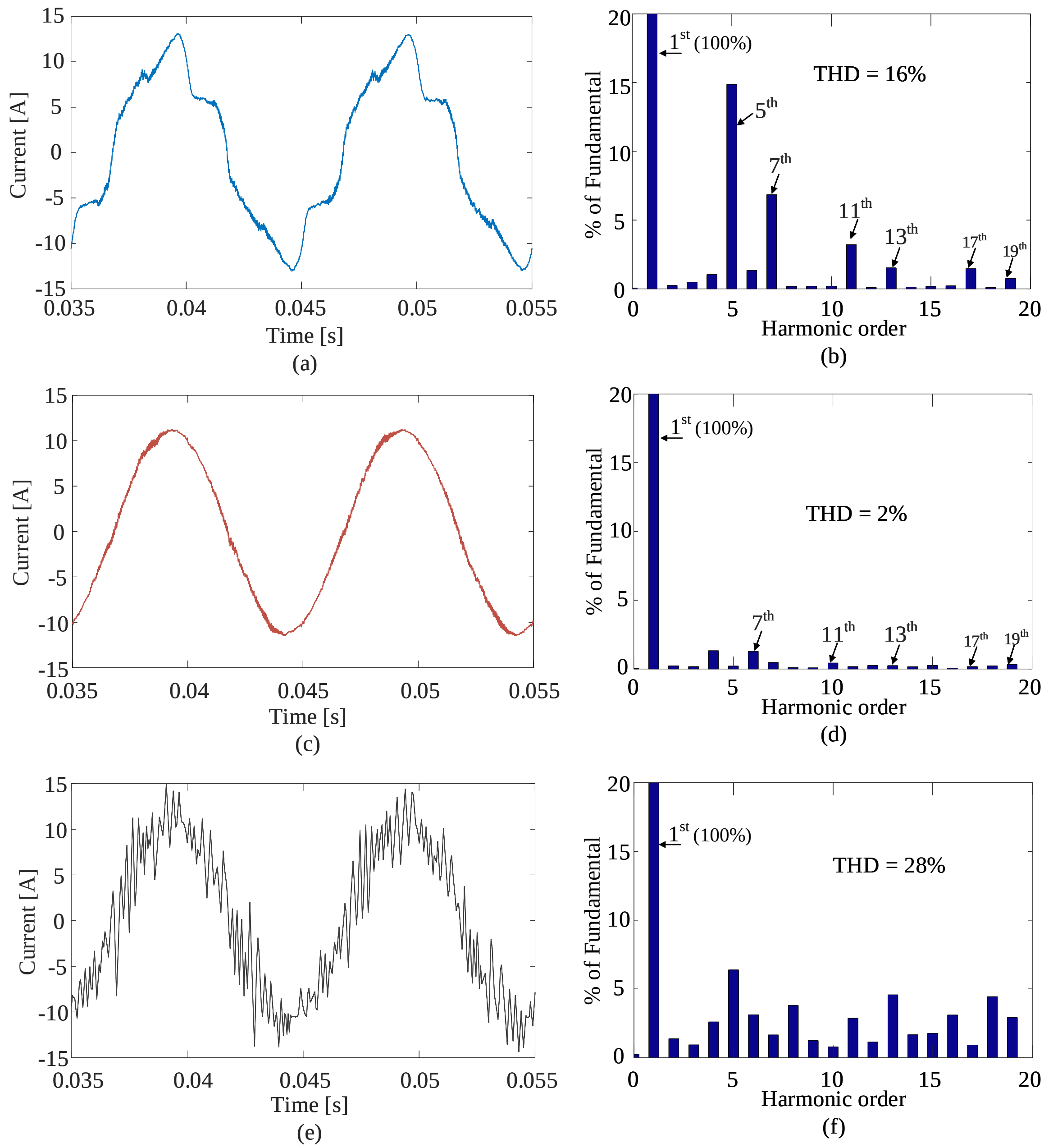

Figure 6.4: Phase ‘a’ current when $[i_d^*, i_q^*] = [10, 5]$A at 1500 rpm: (a) using the standard vector control without the proposed method and (b) its harmonic content, (c) using the standard vector control with the proposed method, and (d) its harmonic content, (e) using hysteresis current control (HCC) and (f) its harmonic content.

Table 6.1: Simulation and Experimental setup Parameters

Parameter	Value
DC link voltage	200 V
Sampling frequency	10 kHz
Switching frequency	10 kHz
d-axis PI current controller	$k_{p,d}$=30, $k_i = 1800$
q-axis PI current controller	$k_{p,q}$=12, $k_i = 1800$

that, the current ripple can be reduced with using soft switching HCC (i.e., the applied phase voltage can be zero, positive or negative the DC link voltage). However, the drawback of soft switching HCC is that each phase needs to be controlled by an H-bridge converter and the standard VSI cannot be used.

In order to compare the reference phase voltage with and without using the proposed method to the one from the FEA model, figure 6.5 shows the procedures of the FEA validation. In the first step, the 3-phase voltages when $[i_d, i_q]$=$[10, 5]$A at 1500 rpm are obtained from the FEA model, they are referred to as v_{u,v,w_FEA}, and they are the essential 3-phase voltages to create the sinusoidal currents when they are applied to the MCSRM. The 3-phase reference voltages from the dynamic model when $[i_d^*, i_q^*]$=$[10, 5]$A at 1500 rpm using the standard vector control with and without the proposed method are obtained as well, and they are referred to as $v^*_{u,v,w}$ and v_{u,v,w_PI}, respectively. In Step 2 in figure 6.5, the 3-phase voltages from the FEA model and the dynamic model are transformed into the dq synchronous reference frame. In Step 3, the direct-and quadrature-axis voltages from the FEA model and dynamic model are compared and this comparison is presented in figure 6.6. It can be noticed from figure 6.6 that the direct-and quadrature-axis voltages from the dynamic model with using the proposed method are similar to those from the FEA model, which explains

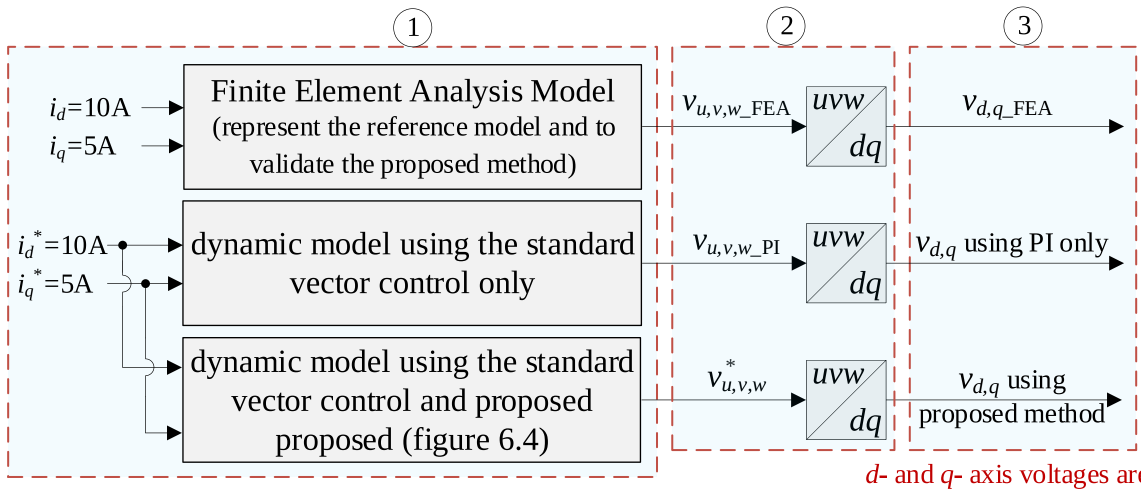

d- and *q*- axis voltages are compared in figure 6.6

Figure 6.5: FEA validation method.

why the phase current in figure 6.4(c) is sinusoidal with the minimum THD. On the other hand, the direct-and quadrature-axis voltages without using the proposed method do not match with those from the FEA model. Hence, the phase current is not sinusoidal as shown in figure 6.4(a).

6.4 Experimental Validation

The proposed harmonics compensation method is validated by experiments using the same setup in chapter 5. The LUTs in (6.2.12) required for the proposed method are saved in the DSP. The flux linkage harmonic vectors can be found at given i_d^* and i_q^* using the interpolation function implemented in DSP. The experimental drive setting is similar to table 6.1. The phase current of the MCSRM with and without using the proposed method is measured and recorded by oscilloscope. The THD of the phase current is calculated using Matlab for 20 cycles of the recorded current. The proposed method is validated for different speeds and current levels at motoring

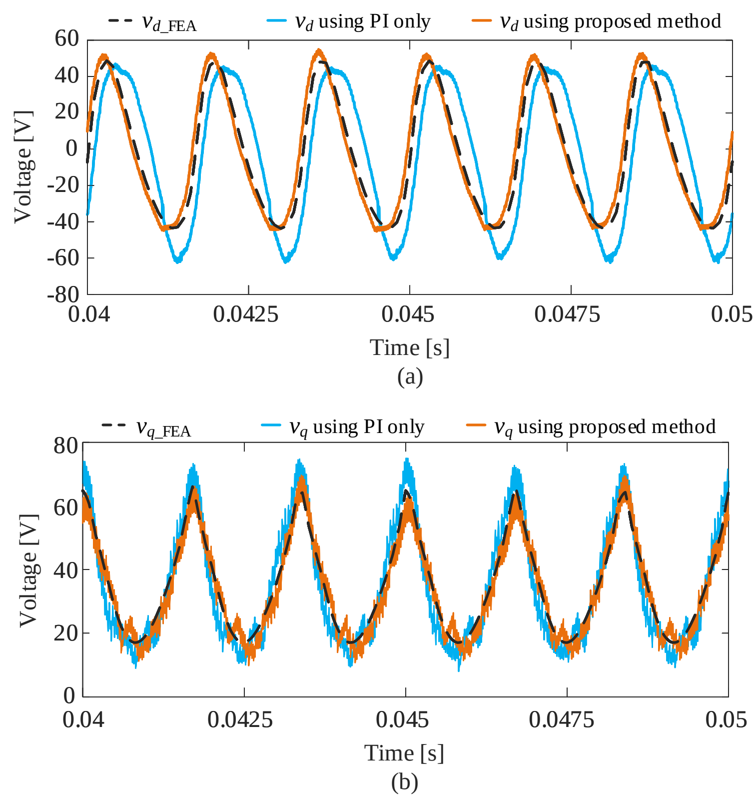

Figure 6.6: (a) direct-and (b)quadrature-axis voltages generated from the FEA model and the Simulink model by using the standard vector control with and without the proposed method.

and generating modes of operation.

6.4.1 Motoring Mode of Operation at 1000 rpm

Figure 6.7 compares the phase current with and without using the proposed method when $[i_d^*, i_q^*]$=$[10, 5]$A. It can be concluded from Figure 6.7(a)-(b) that the phase current without using the proposed method has a THD of 10% with dominant 5^{th}, 7^{th}, 11^{th} and 17^{th} order harmonics. After applying the proposed method, the phase current THD is reduced to 2% as shown in figure 6.7(c)-(d), where the 5^{th}, 7^{th}, 11^{th} and 17^{th} order harmonics are suppressed to less than 1% of the fundamental component.

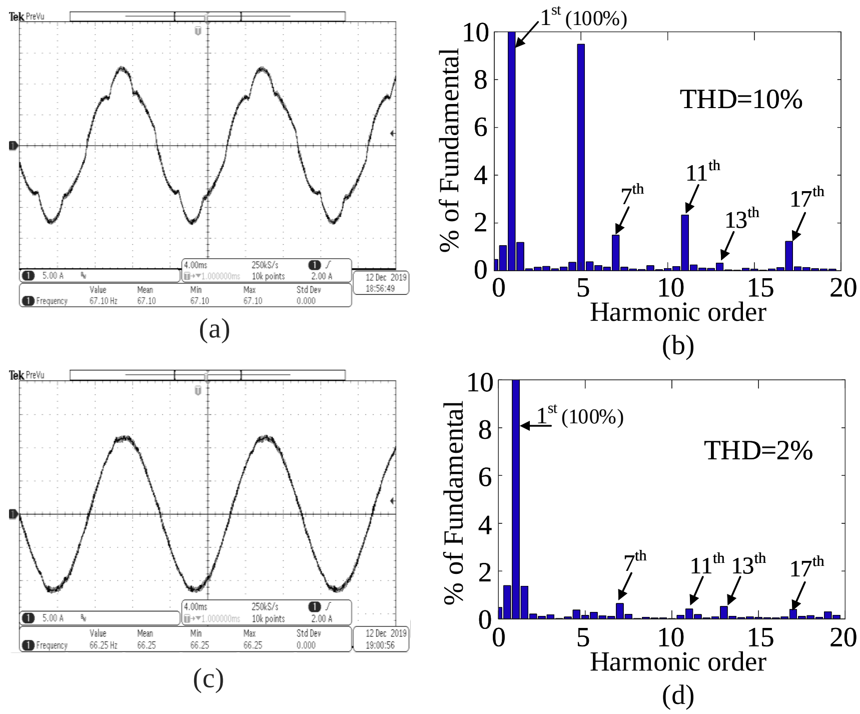

Figure 6.7: Phase current when $[i_d^*, i_q^*]$=$[10, 5]$A during motoring mode of operation and 1000 rpm for f_{bw}=1 kHz, (a) without using the proposed method and its (b) harmonic contents, (c) with using the proposed method and (d) its harmonic contents. Current scale: 5 A/div, time scale: 4 ms/div.

Figure 6.8 shows the improvement in phase current THD by using the proposed method when $[i_d^*, i_q^*]$=$[15, 15]$A. Figure 6.8(a)-(b) show that the phase current without using the proposed method has a THD of 6%. Figure 6.8(c)-(d) show the phase current when the proposed method is applied. It can be noticed from figure 6.8(d) that the magnitude of the 5^{th} harmonic order is reduced from approximately 6% to less than 1%. Similarly, the magnitudes of the 11^{th}, 13^{th}, and 17^{th} order harmonics are reduced to less than 1%. Hence, the phase current THD is reduced from 6% to 1% by using the proposed method.

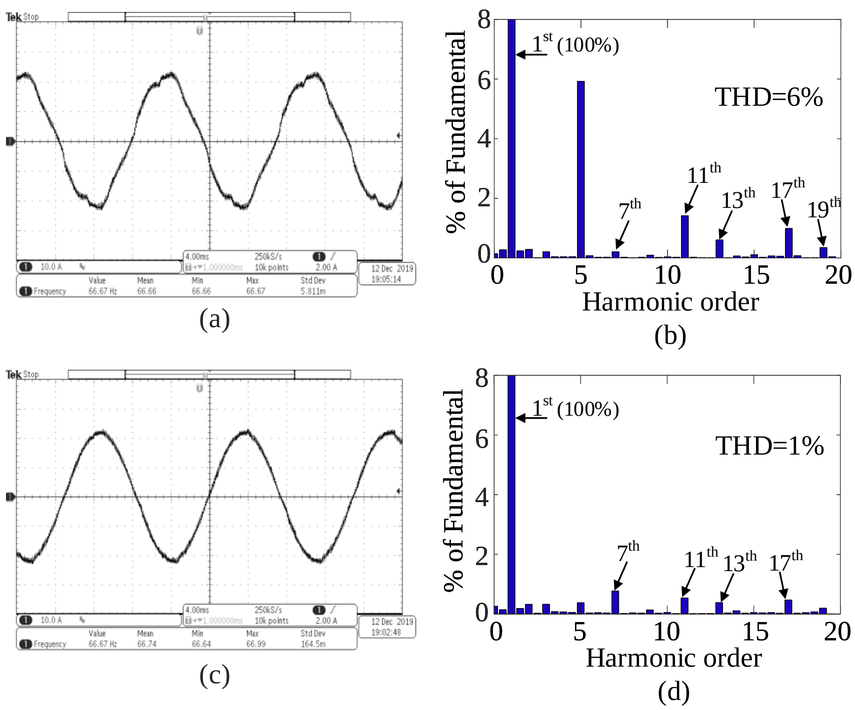

Figure 6.8: Phase current when $[i_d^*, i_q^*]$=[15, 15]A during motoring mode of operation and 1000 rpm for f_{bw}=1 kHz, (a) without using the proposed method and its (b) harmonic contents, (c) with using the proposed method and (d) its harmonic contents. Current scale: 10 A/div, time scale: 4 ms/div.

6.4.2 Motoring Mode of Operation at 1500 rpm

In this section, the proposed method is validated at 1500 rpm. Figure 6.9(a)-(b) show the phase current when $[i_d^*, i_q^*]$=[10,5]A without using the proposed method. It reveals that the 5^{th} and 11^{th} order harmonics are around 15% and 4% of the fundamental component and the phase current THD is 16%. The spatial harmonics of the phase current are suppressed to less than 1% with using the proposed method, as shown in figure 6.9(c)-(d). Hence, the phase current THD is reduced to 2%.

Figure 6.10 shows that the proposed method improves the phase current THD from 10% to 2% when $[i_d^*, i_q^*]$=[15, 15]A and the spatial harmonics are suppressed

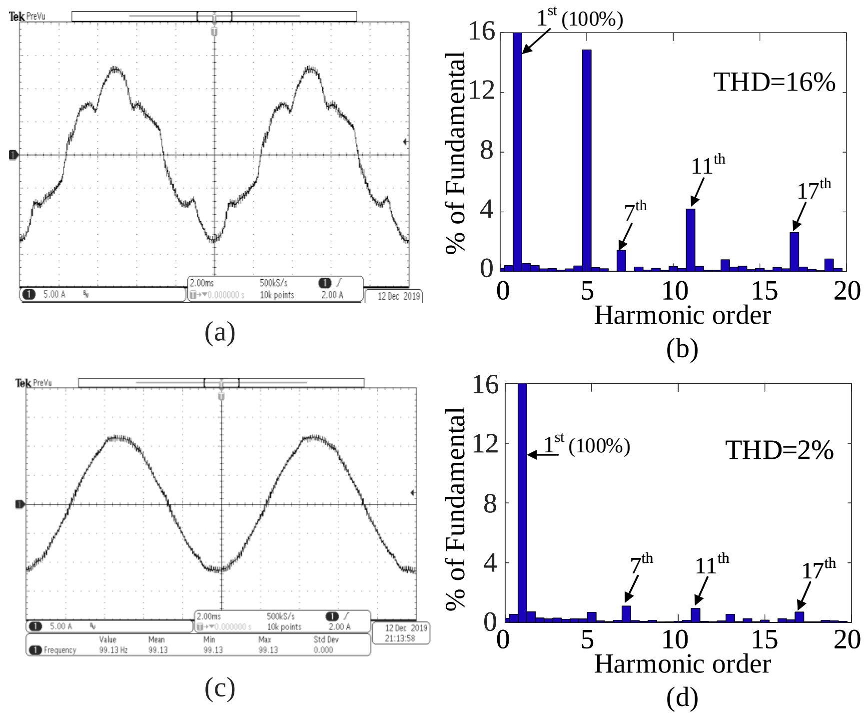

Figure 6.9: Phase current when $[i_d^*, i_q^*]$=[10, 5]A during motoring mode of operation and 1500 rpm for f_{bw}=1 kHz, (a) without using the proposed method and its (b) harmonic contents, (c) with using the proposed method and (d) its harmonic contents. Current scale: 5 A/div, time scale: 2 ms/div.

to less than 1%. It can be concluded from figure 6.9(a) and figure 6.10(a) that the performance of the PI controller degrades when motor speed increases compared to figure 6.7(a) and figure 6.8(a). The deterioration of the PI controller for higher frequencies of disturbance is due to the bandwidth limitation which is a physical property of PI controllers [89]. It is worth mentioning that the current waveforms in figures 6.7 to 6.10 have the minimum possible THD without using the proposed method, since the gains of the PI controller correspond to the maximum allowable bandwidth frequency, which is 1 kHz (f_{sw}/10). Increasing the PI gains will lead to oscillatory behaviour or unstable operation.

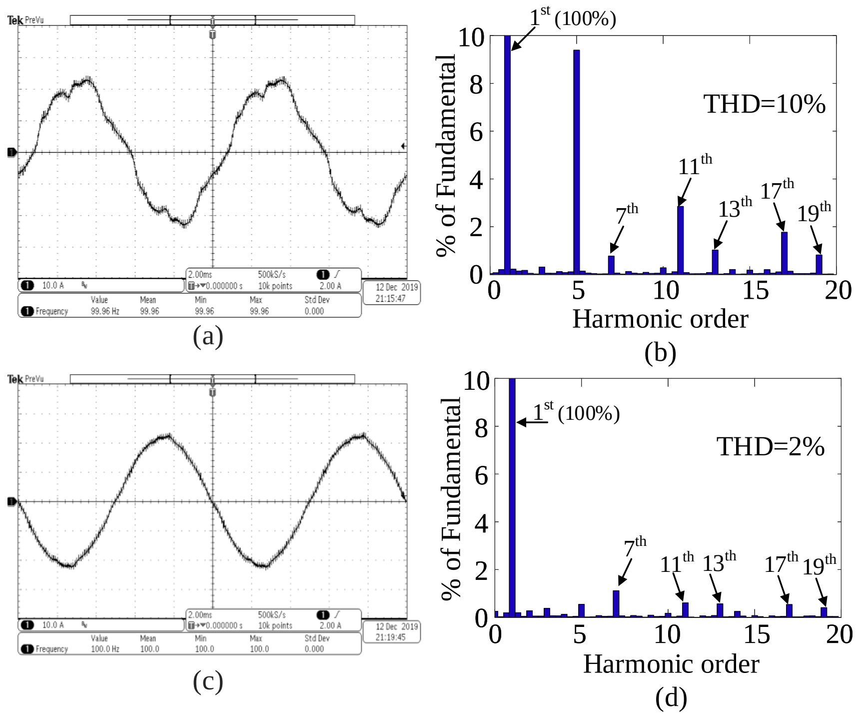

Figure 6.10: Phase current when $[i_d^*, i_q^*]$=$[15, 15]$A during motoring mode of operation and 1500 rpm for f_{bw}=1 kHz, (a) without using the proposed method and its (b) harmonic contents, (c) with using the proposed method and (d) its harmonic contents. Current scale: 10 A/div, time scale: 2 ms/div.

6.4.3 Motoring and Generating Modes of Operation at 1500 rpm With Reduced f_{bw}

As mentioned earlier, the SRM used in this thesis is designed to operate as CSRM. When the motor is operated as MCSRM with multi-phase excitation, the generated torque ripple is high so that the dynamometer cannot control speed above 1500 rpm. However, we know that for the same $[i_d^*, i_q^*]$ and without using the proposed method, the THD gets worse when speed increases due to the deterioration of the PI controller. Thus, in order to show the effect of performance deterioration of the PI controller without exceeding 1500 rpm, the bandwidth of the PI controllers is reduced to the

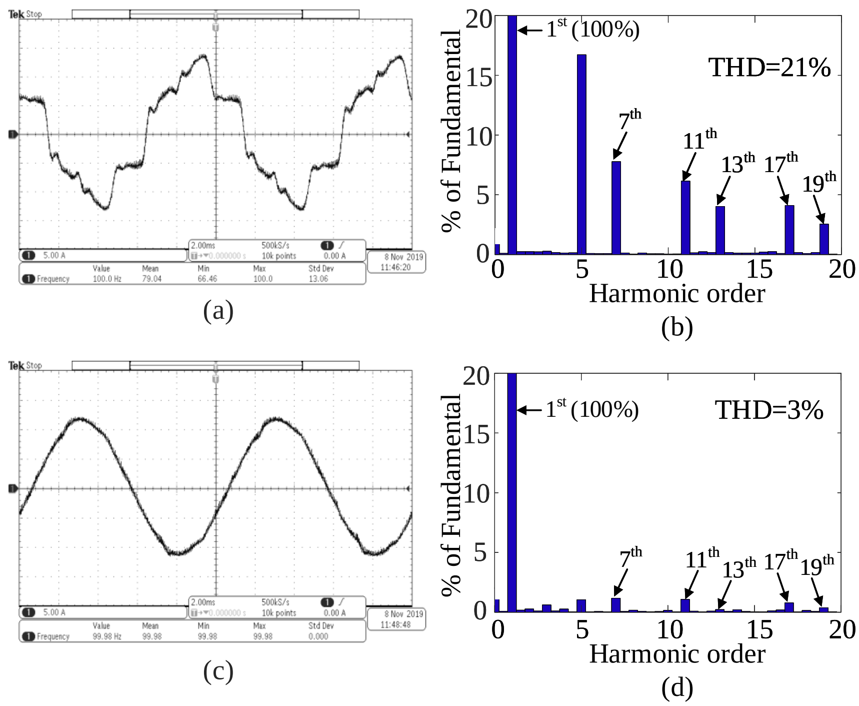

Figure 6.11: Phase current when $[i_d^*, i_q^*]$=[10, 5]A during motoring mode of operation and 1500 rpm for f_{bw}=500 Hz, (a) without using the proposed method and its (b) harmonic contents, (c) with using the proposed method and (d) its harmonic contents. Current scale: 5 A/div, time scale: 2 ms/div.

half (f_{bw}=500 Hz) by reducing the PI controller gains by half.

Motoring Mode of Operation

Figures 6.11 and 6.12 show the phase current at 1500 rpm with the reduced bandwidth PI controllers when $[i_d^*, i_q^*]$=[10, 5]A and $[i_d^*, i_q^*]$=[15, 15]A respectively, with and without using the proposed method. By using the proposed method, the THD of the phase current in figure 6.11 is improved from 21% to 3%. Likewise in figure 6.12, the THD is improved from 17% to 2%.

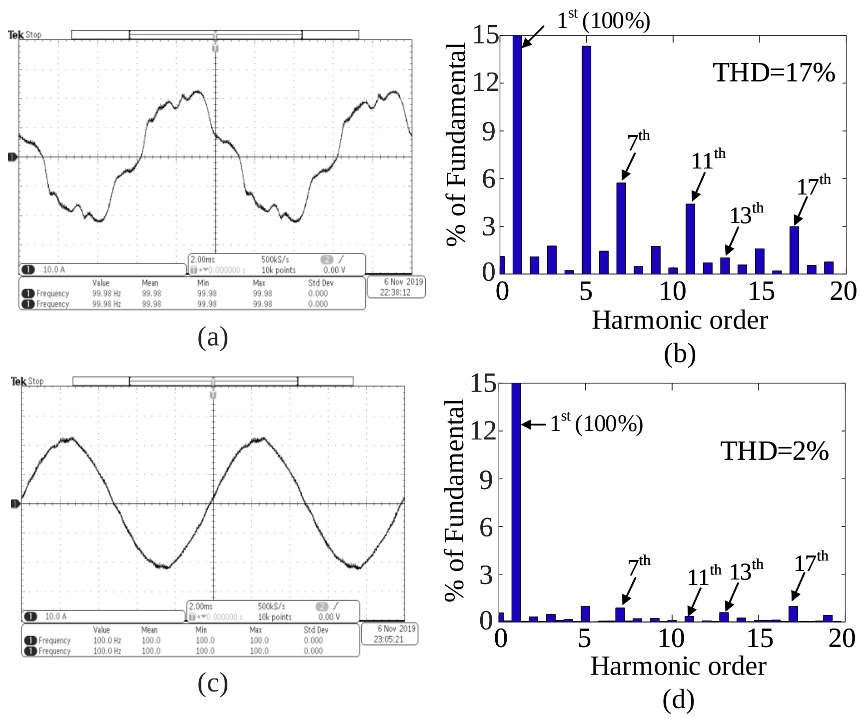

Figure 6.12: Phase current when $[i_d^*, i_q^*]$=$[15, 15]$A during motoring mode of operation and 1500 rpm for f_{bw}=500 Hz, (a) without using the proposed method and its (b) harmonic contents, (c) with using the proposed method and (d) its harmonic contents. Current scale: 10 A/div, time scale: 2 ms/div.

Generating Mode of Operation at 1500 rpm

The proposed method is validated at the generating mode of operation with the PI controllers of reduced bandwidth at 1500 rpm. Figure 6.13 shows the phase current waveform when $[i_d^*, i_q^*]$=$[-5, 15]$A, where the phase current THD is reduced from 13% to 2% after suppressing the spatial harmonics with using the proposed method.

Figure 6.14 shows the phase current when $[i_d^*, i_q^*]$=$[-15, 5]$A. Again, the proposed method succeeds to suppress the spatial harmonics of the phase current with the PI controllers of reduced bandwidth. Hence, the THD of the phase current is reduced from 19% to 3%.

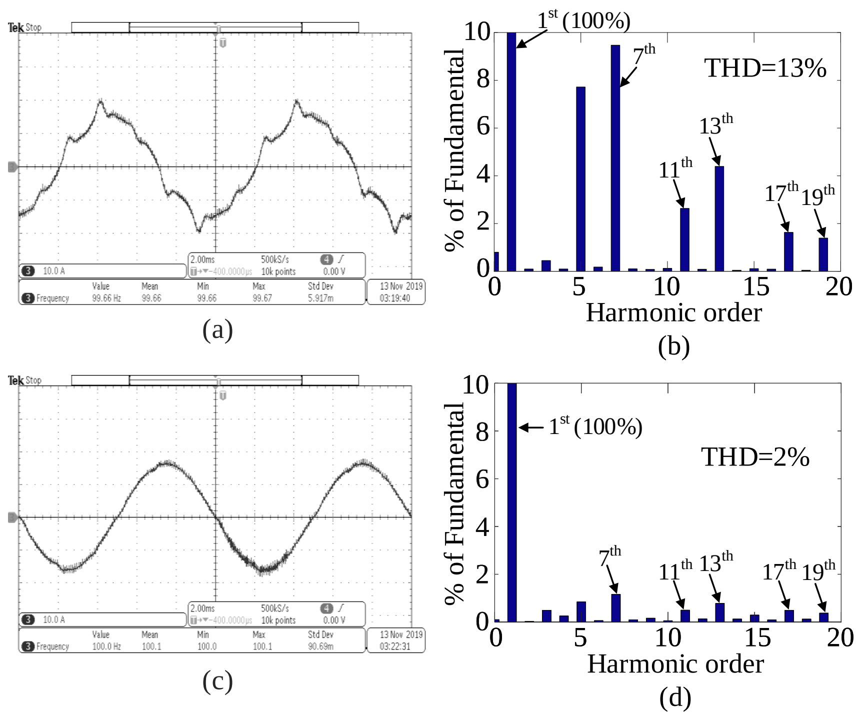

Figure 6.13: Phase current when $[i_d^*, i_q^*]$=$[-5, 15]$A during generating mode of operation and 1500 rpm for f_{bw}=500 Hz, (a) without using the proposed method and its (b) harmonic contents, (c) with using the proposed method and (d) its harmonic contents. Current scale: 10 A/div, time scale: 2 ms/div.

Table 6.2 summarizes the experimental results. It shows the THD of phase current using the standard vector control with and without the proposed method. Table 6.2 also shows the THD of phase current using hysteresis current control and it is obtained from simulation results. The dynamic model that is used to obtain the simulation results is accurate enough since it is in close proximity with the experiments from comparing figure 6.4 with figure 6.9.

The performance and limitations of the standard vector control with and without using the proposed method, the hysteresis current controller, and the PI with the PR controllers are presented in table 6.3. The limitations of the proposed method that is it is model-based since it uses LUTs to describe the motor characteristics, these LUTs

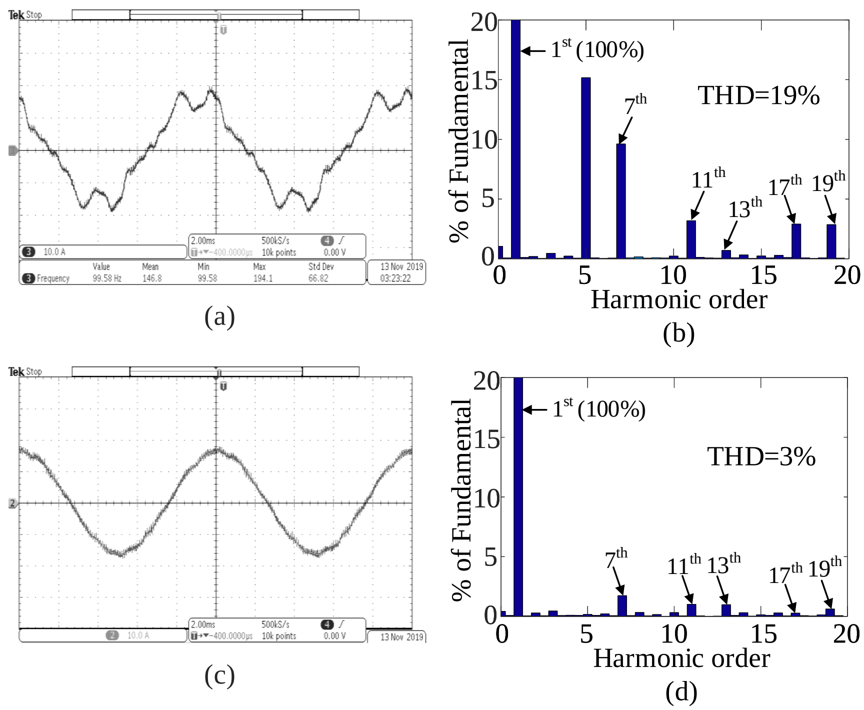

Figure 6.14: Phase current when $[i_d^*, i_q^*]$=$[-15, 5]$A during generating mode of operation and 1500 rpm for f_{bw}=500 Hz, (a) without using the proposed method and its (b) harmonic contents, (c) with using the proposed method and (d) its harmonic contents. Current scale: 10 A/div, time scale: 2 ms/div.

are obtained from the FEA model, and cannot be used for a different motor. On the other hand, the drawbacks of using the PI with the PR controllers is the complexity in determining the cut-off frequency without affecting the system stability. HCC is robust and simple in implementation, however, it requires high switching frequency to reduce the current ripple, in addition to noise due to the variable switching frequency.

Table 6.2: THD of Phase Current Using Different Controllers

$[i_d^*, i_q^*]$A	rpm	f_{bw} kHz	THD standard vector control	THD proposed method	THD HCC
[10, 5]	1000	1	10%	2%	28%
	1500	1	16%	2%	28%
	1500	0.5	21%	3%	28%
[15, 15]	1000	1	6%	1%	17%
	1500	1	10%	2%	17%
	1500	0.5	17%	2%	17%
[−15, 5]	1500	0.5	19%	3%	20%
[−5, 15]	1500	0.5	13%	2%	20%

Table 6.3: Performance Comparison Between Different Controllers

method	THD	complexity	limitation
standard vector control without the proposed method	medium	low	N/A
standard vector control with the proposed method	low	low	model-based
hysteresis current control	high	low	N/A
PI+ PR controllers	low	high	influences stability

6.5 Conclusion

This chapter introduces harmonics compensation method to a 3-phase MCSRM to eliminate the spatial harmonics of the phase current. The spatial harmonics in MC-SRMs cannot be ignored due to the high stator and rotor saliency. The standard vector control with using PI controllers cannot remove the spatial harmonics of the phase current due to the bandwidth limitation. The proposed method injects the essential harmonic voltage vectors to create sinusoidal currents. Voltage vectors are calculated from the flux linkage vectors. The voltage and flux linkage vectors are represented as Fourier coefficients. The Fourier coefficients of the flux linkage are in the form of two-dimensional look-up tables (LUTs), where these LUTs are independent of rotor position which reduces the size of the LUTs significantly. Simulation and experimental results show that the proposed method succeeds to suppress the spatial harmonics of the current and, hence, the phase current THD reduces significantly to 2%-3%. Experimental results validate the proposed method for different motor speeds, current levels, and bandwidth frequency of PI controllers at motoring and generating modes of operation. Furthermore, the proposed method does not require extra hardware or complicated algorithms and it does not influence the system stability. Thus, applying the proposed method is simple, robust and efficient.

Chapter 7

Comprehensive Analysis and Optimized Control of Torque Ripple and Power Factor in Mutually Coupled SRMs With Sinusoidal Current Excitation

7.1 Introduction

So far, we have a dynamic model for the MCSRM in chapter 5 that can predict the harmonic components of electro-magnetic torque for a given direct-and quadrature-axis current, we also can ensure sinusoidal current excitation in chapter 6. Now, we will discuss in this chapter how to chose the direct-and quadrature-axis currents to have the best motor performance. The existing control methods in the literature for MCSRMs are based on maximum torque per ampere control, where *d*- and *q*-axis currents are equal. In these methods, torque ripple and power factors are not considered [19, 30, 33]. In this chapter, the effect of direct-axis and quadrature-axis currents on torque ripple and power factor is first analysed. Then, an optimized control method is developed to improve the power factor, torque ripple, and average torque.

This chapter is organized as follows; section 7.2 analyzes the torque ripple sources in MCSRMs by sinusoidal current excitation, section 7.3 analyzes the effect of the current excitation angle and saturation level on power factor. Section 7.4 presents the proposed optimized control method for MCSRMs, section 7.5 validates the proposed method by experiments. Finally, section 7.6 has the conclusion of the chapter.

7.2 Torque Ripple Analysis

As it was shown in section 5.2.2, the generated electro-magnetic torque waveform has an average value in addition to the 6^{th}, 12^{th}, 18^{th}, and 24^{th} order harmonics. It was also concluded from figure 5.9 that the 6^{th} order harmonic has the largest magnitude among all other present harmonics. As a result, the torque waveform with the minimum magnitude of the 6^{th} order harmonic, corresponds to the minimum torque ripple. The average torque value T_{avg} and the Fourier coefficients of the 6^{th} order harmonic T_{6a} and T_{6b} were represented as (see equation (5.2.20)):

$$T_{avg} = f(|i_d|, |i_q|)\ sign(i_d i_q) \tag{7.2.1a}$$

$$T_{a6} = f_{a6}(|i_d|, |i_q|)\ sign(i_d i_q) \tag{7.2.1b}$$

$$T_{b6} = f_{b6}(|i_d|, |i_q|) \tag{7.2.1c}$$

Thus, the magnitude of 6^{th} order harmonic T_6 is calculated as:

$$T_6 = \sqrt{{T_{a6}}^2 + {T_{b6}}^2} \tag{7.2.2}$$

Figure 7.1 shows the 2D LUTs, $f_{a6}(i_d, i_q)$ and $f_{b6}(i_d, i_q)$ and their vector summation based on equation (7.2.2).

There is an infinite number of $[i_d, i_q]$ operating points that can achieve a certain average torque. These operating points have different phase current magnitude, torque ripple, and power factor. As an example, for an average torque T_{avg} of 3Nm, the range of d- and q- axis currents is swept and the operating points are found using equation (3.2.1). Then, these operating points are simulated using the FEA model. Figure 7.2 shows the torque waveforms from the FEA model that achieve T_{avg} of 3Nm. It can be observed from figure 7.2 that these operating points achieve the same average torque but with different torque ripple.

Figure 7.3 describes the behaviour of the torque ripple for the operating points in figure 7.2. The torque ripple is represented by the magnitude of T_6 with respect to the phase current magnitude, by the help of equation (7.2.2). It can be noticed

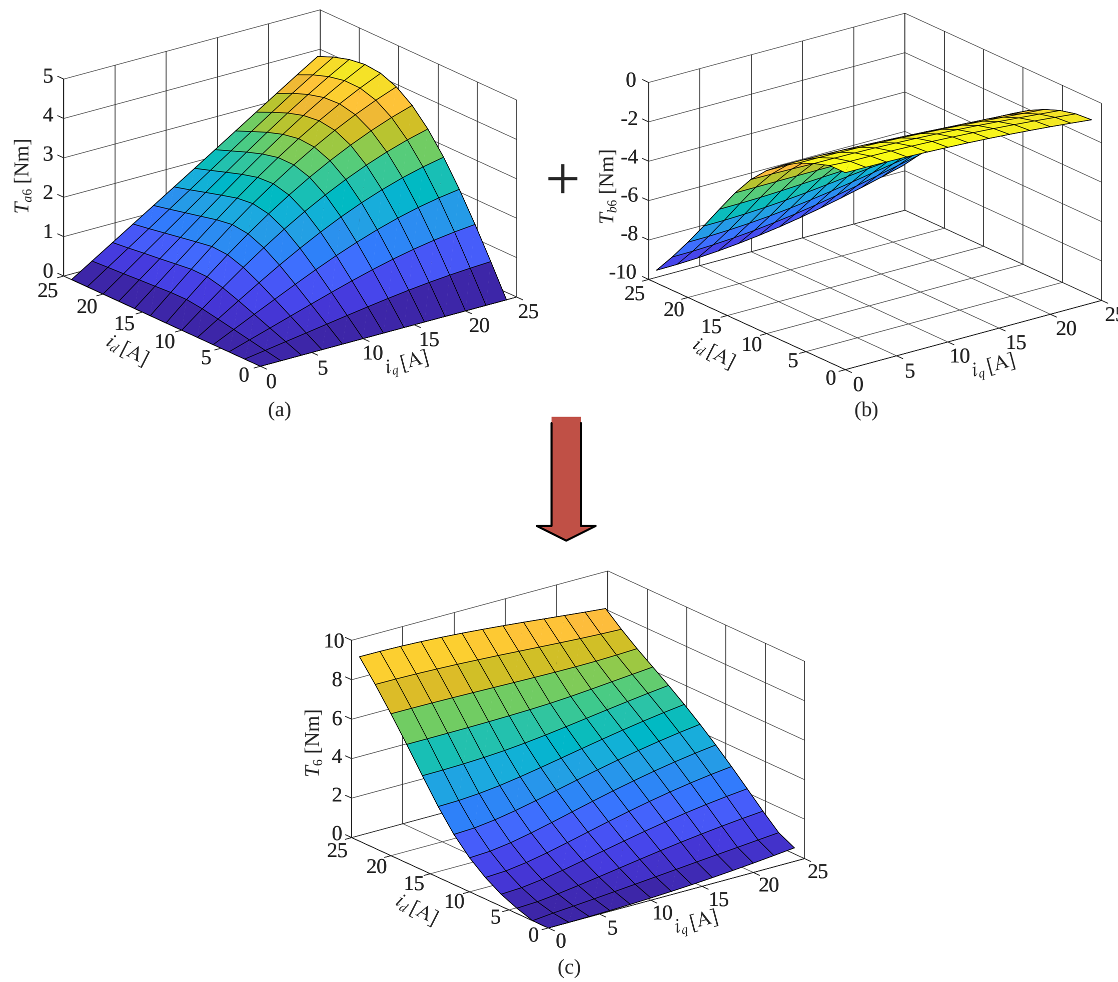

Figure 7.1: Fourier coefficients of the 6^{th} order torque harmonic (a) T_{6a} and (b) T_{6b}, and (c) vector summation of T_{6a} and T_{6b}

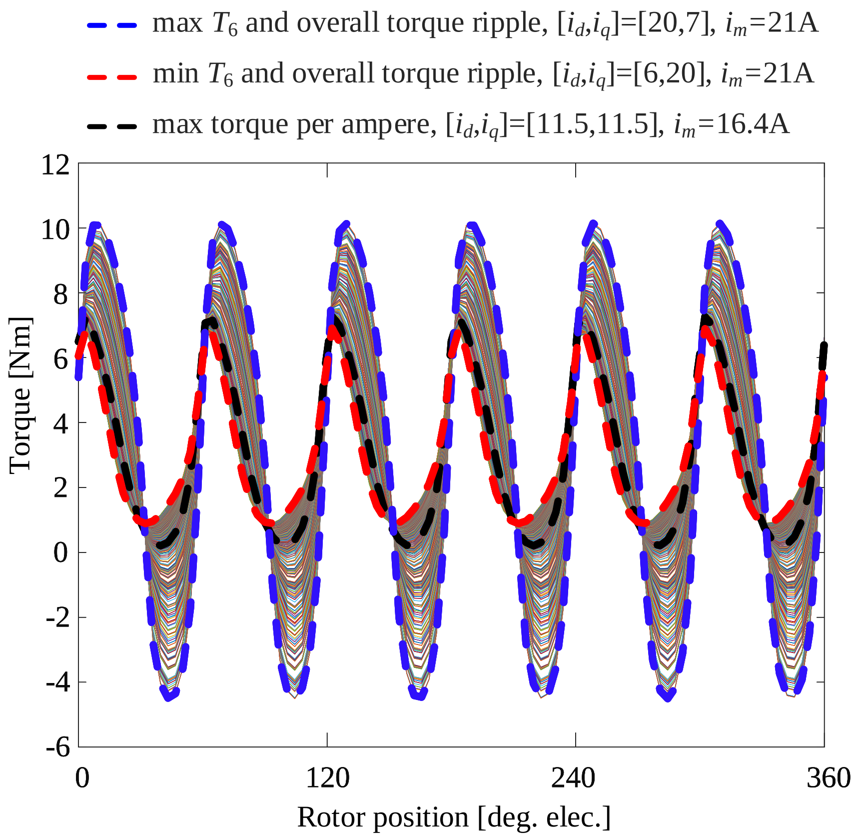

Figure 7.2: Torque waveforms from the FEA model at 3Nm average torque

that the operating point corresponding to the minimum torque ripple has the largest phase current magnitude, and hence, the highest copper loss. On the other hand, the operating point that corresponds to the minimum phase current magnitude has a relatively higher torque ripple. As it will be shown in the next section, this operating point also has a low power factor. Therefore, from the controls perspective, if the phase currents are optimized to achieve the lowest torque ripple, that would result in the highest copper loss. If only the magnitude of phase current is optimized, that would result in a low power factor and a relatively higher torque ripple. It should be noted that, the waveform in figure 7.3 is a quadratic function with respect to the

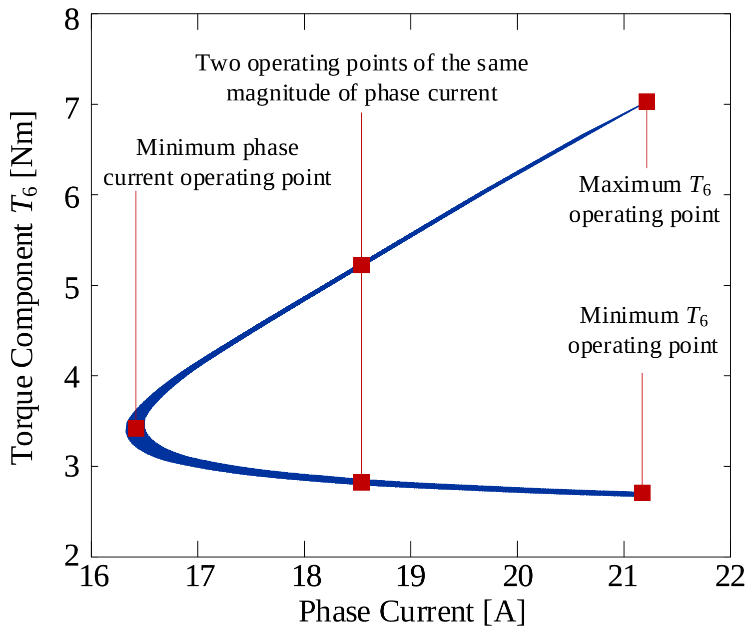

Figure 7.3: Non-linear relationship between torque ripple (T_6) with respect to phase current magnitude.

torque ripple component, T_6. Therefore, there are two operating points with the same phase current magnitude and same average torque, T_{avg} of 3Nm, but with different T_6. The implications of this behaviour will be discussed in more detail in the next section.

Please note that, the waveforms in figures 7.2 and 7.3 are the same for any speed, as the average torque and the 6^{th} order torque harmonic were found from equation (7.2.1). Both expressions are dependent on d- and q-axis currents, but they are independent of the motor speed. The implication of speed will also be discussed in the next section. The higher the speed, the higher the induced voltage, which in turn requires higher phase voltage to inject the same phase current.

7.3 Power Factor Analysis

Power factor affects the performance of both the motor and the inverter. From the inverter side, higher power factor means that less reactive power is supplied for the same apparent power. Thus, the size and the rms current of the DC-link capacitor can be reduced. The higher power factor also reduces the volt-ampere rating of the converter. From the motor perspective, power factor influences the core losses [102], and it reflects the saturation level of the motor [103]. In a saturated-magnetic system, the area corresponding to the co-energy on the flux linkage-current characteristics is larger than the area corresponding to the field energy. The co-energy represents the energy converted into mechanical energy. The field energy represents the magnetic energy stored in the system. Therefore, in an SRM, the ratio between the co-energy and field energy is equivalent to the ratio between the real power and reactive power, and it represents the power factor. Hence, a higher power factor can be achieved in an SRM when it operates at a higher saturation level. Due to its excitation principles and winding configuration, the majority of the flux in CSRM is in the radial direction [104]. This helps with the core saturation, but also results in stronger radial forces that would excite the stator core. The excitation principles in MCSRM results in lower radial flux, which in turn results in smaller radial forces [17, 48]. However, this also results in less effective core saturation as compared to CSRM. In other words, MCSRM saturates at higher current levels as compared to CSRM. This is the major factor for why the power factor of MCSRM is relatively low as compared to CSRM.

Power factor can be calculated for the operating points that achieve 3Nm average torque in figure 7.2. The fundamental d- and q- axis voltages v_d, v_q are first calculated at given d- and q- axis currents and given speed (see equations (3.2.2) and (3.2.3)):

$$v_d = i_d R - \lambda_{qo} w \tag{7.3.1a}$$

$$v_q = i_q R + \lambda_{do} w \tag{7.3.1b}$$

where R is the phase winding resistance. λ_{do} and λ_{qo} are similar to the first order Fourier coefficients of the phase flux linkage as mentioned in section 5.1.3 and they can be obtained from equation (6.2.12):

$$\lambda_{do} = f_{an}(|i_d|, |i_q|)\ sign(i_d) \tag{7.3.2a}$$

$$\lambda_{qo} = f_{bn}(|i_d|, |i_q|)\ sign(i_q) \tag{7.3.2b}$$

After calculating the fundamental voltage components, the power factor can be calculated based on the real power, P, and the reactive power, Q, (see equations (3.2.4) to (3.2.6)):

$$P = \frac{3}{2}(v_d i_d + v_q i_q) \tag{7.3.3a}$$

$$Q = \frac{3}{2}(v_q i_d - v_d i_q) \tag{7.3.3b}$$

$$cos(\phi) = \frac{P}{\sqrt{P^2 + Q^2}} \tag{7.3.3c}$$

where $cos(\phi)$ is the power factor. Figure 7.4 shows the power factor and phase voltage with respect to the phase current magnitude for the operating range that achieves 3Nm average torque at 1000 rpm. It can be noticed from figure 7.4 that the same magnitude of phase current can be created by two different voltage magnitudes. For the same phase current magnitude, the operating point that corresponds to a lower

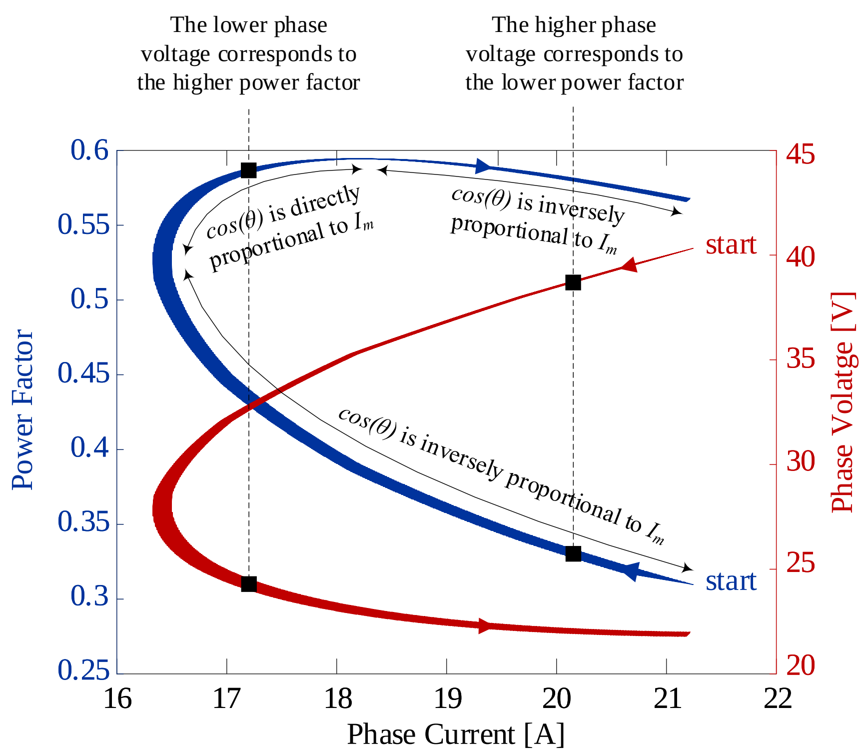

Figure 7.4: non-linear relationship between phase voltage and power factor, with respect to phase current magnitude.

phase voltage also corresponds to a higher power factor. This can be observed in figure 7.4 by following the direction of the power factor and phase voltage curves designated by the arrows. The operating point with the higher power factor has lower induced emf, so that the same magnitude of phase current is generated with a lower phase voltage. This can simply be quantified by expressing the phase voltage for single-phase excitation [104]:

$$v_u = i_u R + \underbrace{\left(L_u(\theta) \frac{di_u}{dt} + i_u \frac{dL_u(\theta)}{d\theta} w \right)}_{\text{induced emf}} \tag{7.3.4}$$

where v_u is the phase voltage, i_u is the phase current, and L_u is the phase inductance. Equation (7.3.4) shows that the phase voltage depends on the phase current, phase resistance, phase inductance, and motor speed w. For the same motor speed, phase current, and phase resistance, v_u depends on the phase inductance, L_u. As the core saturates, the magnitude of L_u decreases, which in turn, limits the induced emf. This enables injecting the same magnitude of current with a lower phase voltage.

Figure 7.4, the blue curve describing the relationship between the power factor and phase current can be divided into three regions. In the majority portion of the curve, the power factor is inversely proportional to the magnitude of the phase current. This implies that the saturation level represented by the power factor does not necessarily increase with the phase current magnitude. The location of the current vector ha s a significant effect on the power factor, as well. The current phasor is a rotating vector in space and its magnitude is $\frac{3}{2} I_m$, where I_m is defined by the d- and q- axis components:

$$I_m = \sqrt{i_d^2 + i_q^2} \tag{7.3.5}$$

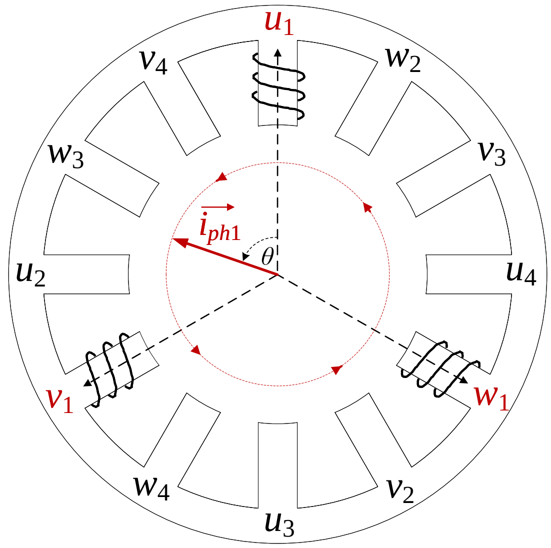

Figure 7.5: Rotating current vector i_{ph1} due to three phases shifted in time and space by 120 degrees

In a balanced 3-phase AC machine, the phase windings are distributed 120° apart in space and the electrical phase shift between phases is 120°. This creates a current vector, i_{ph1}, that has a constant magnitude of I_m, and it rotates uniformly in space (see figure 7.5). The instantaneous position of the current phasor depends on the vector summation of the instantaneous values of the 3-phase currents. The 12/8 SRM has four coils per phase and, hence, there are four sets of 120°-phase-shifted *abc* coils and the phase shift between each set is 90° (see figure 7.5). Therefore, there are four current phasors in space and they are 90° phase shifted from each other. For the coil set shown in figure 7.5, the current phasor can be expressed as:

$$\vec{i}_{ph1} = \underbrace{i_u(t) + i_v(t)}_{\text{instantaneous values}} \underbrace{e^{j\frac{2\pi}{3}}}_{\text{position in space}} + i_w(t)e^{j\frac{-2\pi}{3}} \tag{7.3.6a}$$

$$= \frac{3}{2} I_m e^{j\theta}, \quad \theta = 0 \rightarrow 2\pi \tag{7.3.6b}$$

where $i_u(t)$, $i_v(t)$ and $i_w(t)$ are the instantaneous values of the phase currents, and θ is the instantaneous position of the current phasor in space. The initial position, when $t = 0$, of the current phasor, i_{ph1}, is defined by the current excitation angle θ_{dq}:

$$\theta_{dq} = tan^{-1}(\frac{i_q}{i_d}) \tag{7.3.7a}$$

$$\theta = \theta_{dq} + wt, \quad wt = 0 \to 2\pi \tag{7.3.7b}$$

The initial position ($\theta = \theta_{dq}$) is when the rotor is aligned with the stator poles of phase u as shown in figure 7.5 (see section 5.1.2). At that position and for counter clockwise direction of rotation, magnetizing the stator poles of phase w will generate positive torque. In other words, the current phasor should be aligned with the stator poles of phase w, where the initial angle θ_{dq} would be 60 degrees. The closer the current phasor to the stator poles of phase w, a higher saturation level it will achieve and, hence, the higher the power factor will be.

For instance, the two operating points from the operating range that achieves 3Nm average torque $[i_d, i_q] = [8.4, 16]$A and $[i_d, i_q] = [15.9, 8.6]$A have the same current magnitude of 18A but their power factor at 1000 rpm is 0.67 and 0.46, respectively. The first operating point has a higher power factor as its current phasor is closer to the stator poles of phase w at the initial position, $\theta_{dq} = 62°$, compared to the second point which has an excitation angle of $\theta_{dq} = 28°$. In order to confirm that the maximum power factor is achieved at $\theta_{dq} = 60°$, figure 7.6 shows two conditions for the power factor with respect to the excitation angle when $I_m = 18$A. The first condition is when the phase resistance, R is ignored, and it shows that the maximum power factor occurs at $\theta_{dq} = 60°$. At this excitation angle, the current phasor is aligned with phase w,

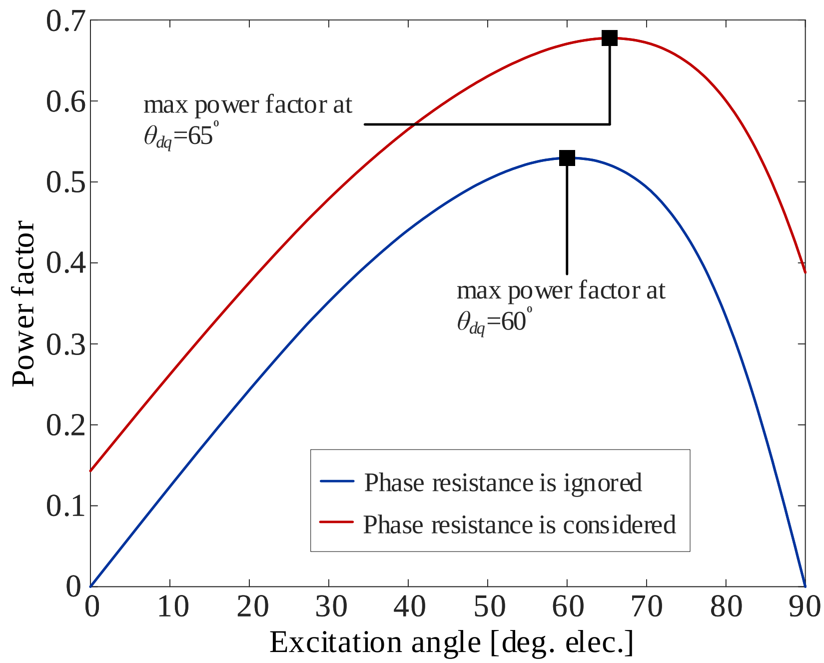

Figure 7.6: Power factor with respect to the current excitation angle at $I_m = 18$A with and without considering the phase resistance.

which at the given rotor position generates torque in the counter clockwise rotation, and achieves the highest saturation level. In the second condition in figure 7.6, the phase resistance is not ignored. Then, the total real power, P equals to the sum of the real power consumed by the motor and the power loss due to the phase resistance, ${I_m}^2R$. As a result, the maximum power factor occurs at $\theta_{dq} = 65°$ as it depends not only on the motor saturation level, but also on ${I_m}^2R$ losses. In the rest of this chapter, the phase resistance, R is taken into account when calculating the power factor.

Figure 7.7 shows the relationship between power factor and the current excitation angle, θ_{dq} for the operating range that achieves the 3Nm average torque at different speeds. Figure 7.7 reveals that the power factor increases till it reaches a certain excitation angle and then it starts to decrease. Figure 7.8 shows the excitation angles

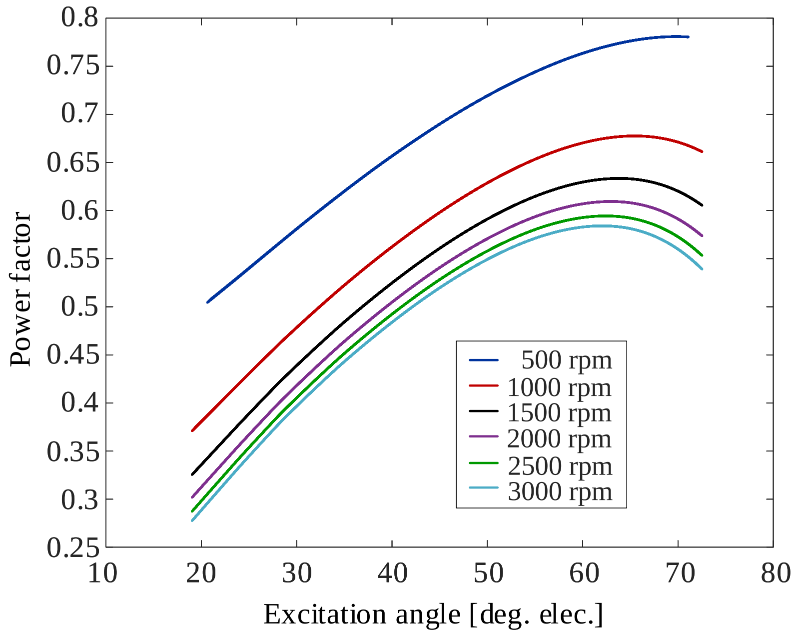

Figure 7.7: Non-linear relationship of power factor with respect to current excitation angle θ_{dq} at different speeds for 3Nm average torque.

corresponding to the maximum power factor at different speeds for average torque of 1Nm, 2Nm, and 3Nm. It can be seen that the maximum power factor always happens at an excitation angle between 62° and 67°. As mentioned before, the maximum power factor is not at $\theta_{dq} = 60°$ due to the ${I_m}^2 R$ losses and the different current magnitude I_m for the operating range that achieves the same average torque.

In order to show how the location of the current phasor affects the magnetization of stator poles, figure 7.9 shows the magnetic flux path at the aligned position for the maximum and minimum power factor operating points achieving T_{avg} =3Nm at 1000 rpm. It can be observed that when the current excitation angle is 65°, the current phasor is approximately aligned with the stator poles of phase w. In other words, the 65° current phasor is magnetizing the unaligned stator poles of phase w which are responsible for torque production. When the excitation angle is 19°, the

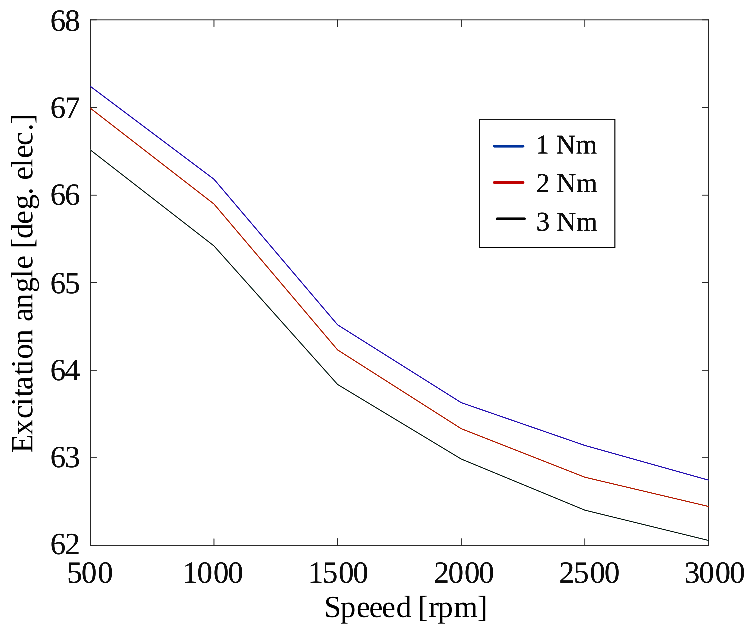

Figure 7.8: Non-linear relationship between current excitation angle θ_{dq} corresponding to the maximum power factor with respect to speed at different torque conditions.

current phasor is closer to phase u. However, the rotor poles are already aligned with phase u; therefore, this excitation angle generates the minimum torque since there is no variation in reluctance. When the rotor aligns with phase w after 15 degrees of rotation, the current vector rotates 60° in the same direction, as the electrical frequency is four times the mechanical frequency. The 60° rotation of the current phasor makes it aligned with phase v to magnetize its stator poles similar to what happened with the stator poles of phase w at the initial rotor position.

In order to explicit the difference between the maximum power factor and the maximum torque per ampere operating points, the phase current is decoupled into two components i_P and i_Q as shown in figure 7.10. i_P is the current component responsible for the real power as it is in phase with the voltage vector V_m. i_Q is the

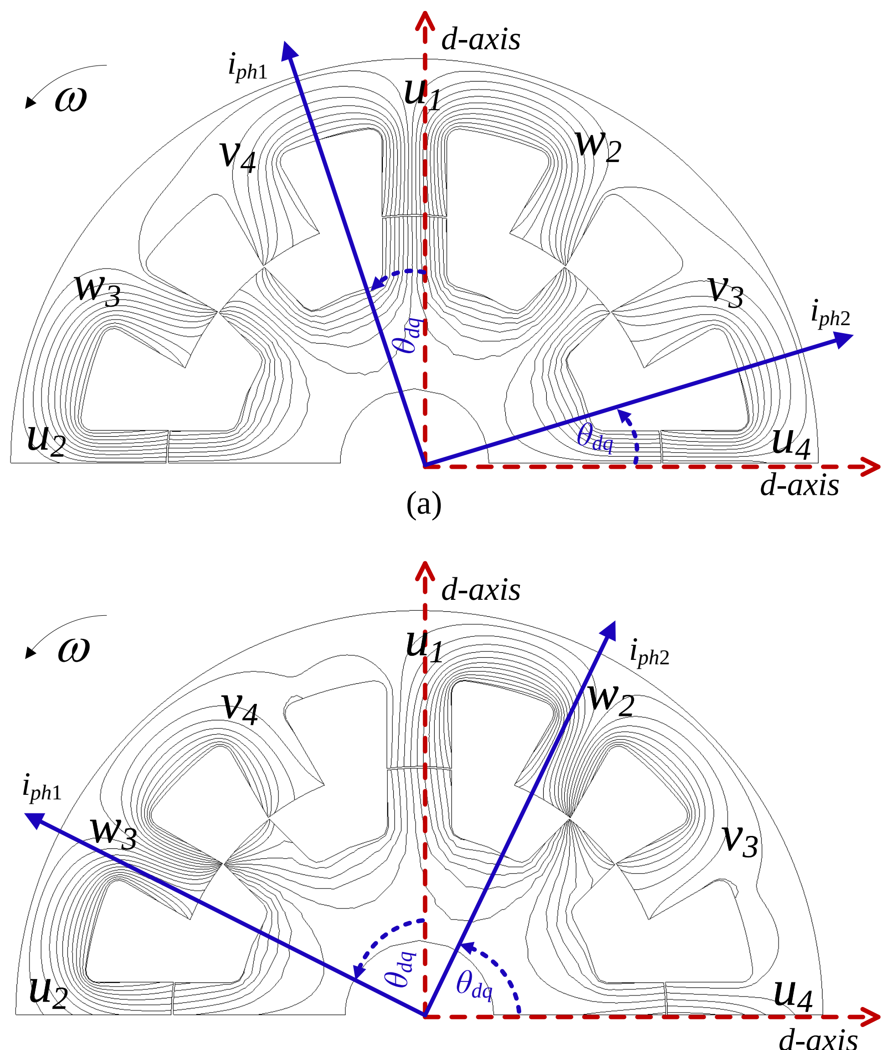

Figure 7.9: Current phasors at the initial rotor position ($\theta = \theta_{dq}$) and 1000 rpm (a) the minimum power factor operating point $\vec{i}_{ph1} = 21.1\angle\ 19°$, (b) the maximum power factor operating point $\vec{i}_{ph1} = 18.9\angle\ 65°$.

current component responsible for the reactive power:

$$i_P = I_m cos(\phi) \tag{7.3.8a}$$

$$i_Q = I_m sin(\phi) \tag{7.3.8b}$$

$$I_m = \sqrt{i_P^2 + i_Q^2} \tag{7.3.8c}$$

The real power, P and reactive power, Q can be reformulated using equation (7.3.8):

$$P = \frac{V_m}{\sqrt{2}} \frac{I_m}{\sqrt{2}} cos(\phi) = \frac{V_m}{2} i_P \tag{7.3.9a}$$

$$Q = \frac{V_m}{\sqrt{2}} \frac{I_m}{\sqrt{2}} sin(\phi) = \frac{V_m}{2} i_Q \tag{7.3.9b}$$

$$cos(\phi) = \frac{P}{\sqrt{P^2 + Q^2}} = \frac{i_P}{I_m} \tag{7.3.9c}$$

From equation (7.3.9)c, it is clear that the power factor is dependent on both i_P and I_m. Thus, the maximum power factor maximizes the ratio i_P/I_m regardless of how much I_m is. The maximum torque per ampere operating point minimizes the total current I_m regardless of how much is i_P or i_Q.

7.4 Optimized Performance for MCSRM

So far, we have analysed the torque ripple and power factor in MCSRM for sinusoidal current excitation. In this section, the selection of the optimized d- and q- axis currents will be discussed to minimize the torque ripple, and maximize the power factor and average torque. For these three performance parameters, the objective

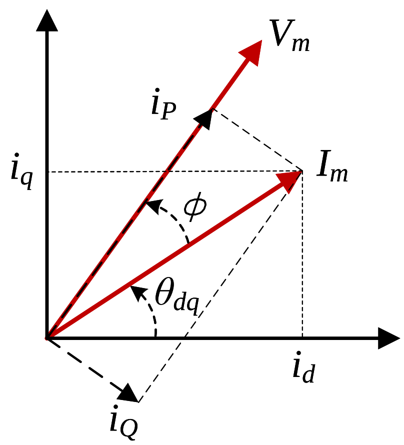

Figure 7.10: Currents components responsible for real and reactive power, i_P and i_Q.

function, j is formulated as:

$$j = \alpha(I_m/I_{rated}) + \beta(T_6/T_{6rated}) - \gamma cos(\phi) \tag{7.4.1}$$

$$\alpha + \beta + \gamma = 1 \tag{7.4.2}$$

where I_{rated} is the rated current, and T_{6rated} is the maximum T_6, which is 9.5Nm for the motor used in this thesis as shown in figure 7.1(c). α, β and γ are the weighting coefficients of the phase current, torque ripple, and power factor, respectively. The available voltage, the rated motor current, and the reference torque constitute the constraints of the optimization problem. The phase voltage depends on the motor speed as shown in equation (7.3.1). The optimized operating point is applicable as long as the line voltage is less than the DC link voltage. This is the maximum line voltage at the unity modulation index with using the space vector modulation (SVM). The voltage in equation (7.3.1) is the fundamental component, while the resultant voltage waveform has also harmonic components in order to remove the spatial harmonics of phase current as mentioned in chapter 6. Thus, a room of 30% is left for the voltage harmonics. Similarly, the phase current should be less than or equal to the rated motor current considering the thermal limitations. Finally, the average torque must be equal to the reference torque. Hence, the three constraints of the optimization problem can be formulated as:

$$\sqrt{i_d^2 + i_q^2} \leq i_{rated} \tag{7.4.3a}$$

$$\sqrt{v_d^2 + v_q^2} \leq 0.7\big(v_{dc}/\sqrt{3}\big) \tag{7.4.3b}$$

$$T_{avg} = T_{ref} \tag{7.4.3c}$$

The objective function in (7.4.1) combines the three objectives in one function by using the weighting coefficients in (7.4.2). The DC voltage utilization is considered in the optimization problem by optimizing the power factor (see equation (7.4.1)) and limiting the phase voltage as in equation (7.4.3). In order to identify how to select the weighting coefficients, some analysis have been applied. Figure 7.11 shows the optimized operating points at 3Nm and different speeds when only one weighting coefficient is considered and the other coefficients are set to zero.

As given in equation (7.2.1), the average torque depends on the d- and q-axis currents only and it is independent of the motor speed. Thus, in Region ① in figure 7.11, the minimum phase current to achieve the reference torque is the same at 500 rpm (the blue ×), 1000 rpm (×), 1500 rpm (the green ×), and 2000 rpm (the red ×), but with different power factors. The higher the speed, the higher the induced voltage, which in turn requires higher phase voltage to inject the same phase current and results in a lower power factor. T_6 also depends on d- and q- axis

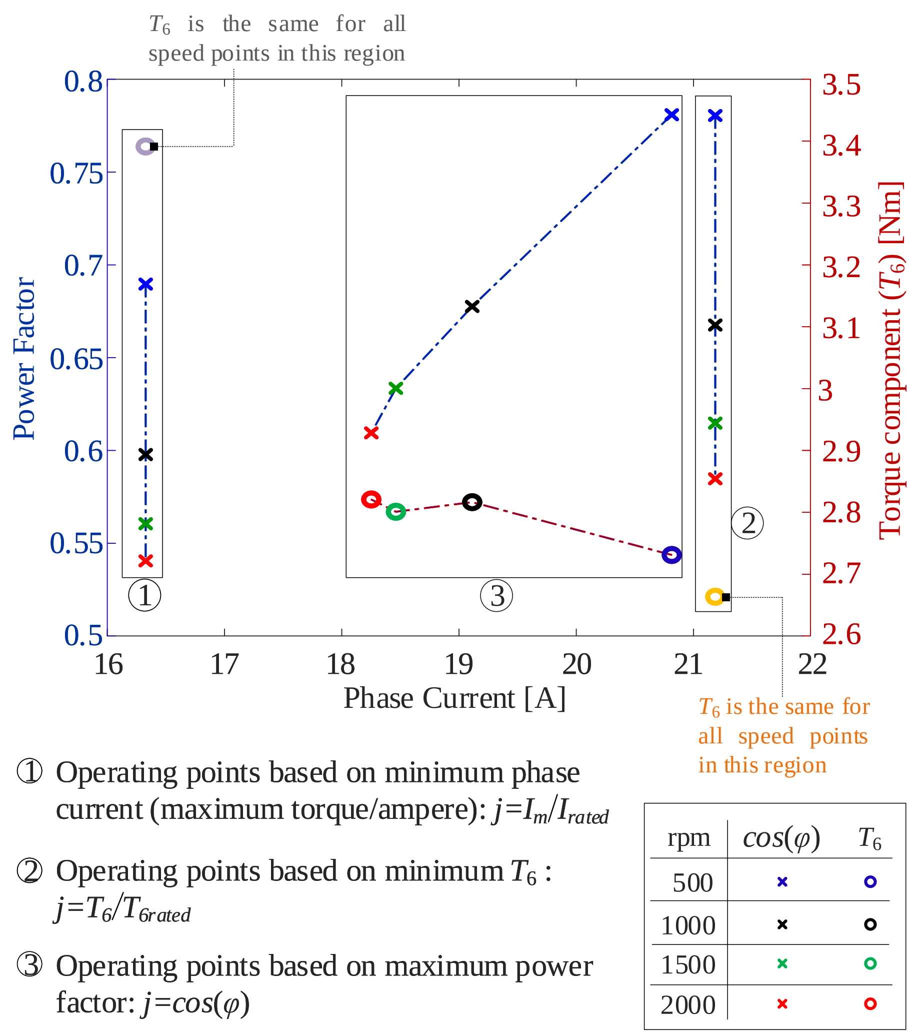

Figure 7.11: Optimized operating points at 3Nm based on the maximum torque per ampere ($j = I_m/I_{rated}$) are shown in Region ①, the minimum torque ripple ($j = T_6/T_{6rated}$) are shown in Region ②, and the maximum power factor ($j = cos(\phi)$) are shown in Region ③.

currents and it is independent of motor speed (see equation (7.2.1)). Therefore, the operating points in Region ① have the same T_6 (the bright lavender ∘). It can be noticed from the results in Region ① that minimizing the phase current results in the highest T_6. It also results in the lowest power factor. For example, the power factor at 2000 rpm in Region ① is lower than the power factor in Region ② and Region ③ for the same operating point. This can be observed by comparing the (the red ×) symbols in the three regions. Region ② in figure 7.11 defines the optimized operating points that have the minimum T_6. Since the operating points in Region ② achieve the same reference torque, they have the same phase current and the same T_6, which is 2.6Nm (denoted by the golden ∘). It can be observed from figure 7.11 that minimizing the torque ripple results in the highest phase current magnitude, which is the motor rated current. For instance, the black × symbols in Region ② have higher phase current compared to the × symbols of the same color in Region ① and Region ②. Region ③ defines the operating points which have the maximum power factor. These operating points have different d- and q- axis currents, and hence, different T_6 and power factor. T_6 in Region ③ (denoted by the ∘ symbols in different colors) varies between 2.7Nm and 2.9Nm. When the operating points were optimized for the minimum T_6 in Region ②, the minimum value was 2.6 Nm. Therefore, achieving the maximum power factor results in an acceptable T_6, which is close to the minimum value. Additionally, the operating points in Region ③ also have an intermediate magnitude of phase currents between that for Region ① and Region ②. Thus, based on the results in figure 7.11, the weighting coefficient of the torque ripple β in equation (7.4.1) can be set to zero, as optimizing the power factor will result in an acceptable T_6. Then, (7.4.2) reduces to:

$$\alpha + \gamma = 1 \tag{7.4.4}$$

In order to define the values of α and γ, the optimization problem has been developed in MATLAB using Genetic Algorithm. The weighting coefficient α is varied between 0 and 1. The optimization is conducted at different speeds for the rated torque, $T_{avg} = 3$Nm. The results are presented in figure 7.12. It can be concluded from figure 7.12(a) that as α increases, the phase current magnitude decreases. This is intuitive, because higher values of α penalizes the phase current as formulated in (7.4.4). The weighting coefficient of the power factor γ decreases with the increase of α since their summation is unity (7.4.4). Hence, the power factor reduces with increasing α as shown in figure 7.12(c). When α exceeds 0.4, the phase current magnitude stays almost constant, but only the power factor reduces. As a result, the current and power factor weighting coefficients α and γ are set to 0.4 and 0.6. respectively. This provides a good agreement between power factor, phase current magnitude, and torque ripple T_6.

The optimized d- and q- axis currents of the MCSRM for the operating speed and torque ranges are shown in figure 7.13. Figure 7.13 represent the LUTs that generate the reference d- and q-axis currents, which achieve the optimum performance at different operating points. These two LUTs are saved in the Digital Signal Processor (DSP). The reference d- and q- axis currents are then found at the given operating condition by using interpolation function implemented in the DSP. The speed range in figure 7.13 is from 500 rpm to 3000 rpm with 250 rpm step, while the torque range is from 0.5Nm to 3Nm with 0.25Nm step. The torque range is not starting from zero

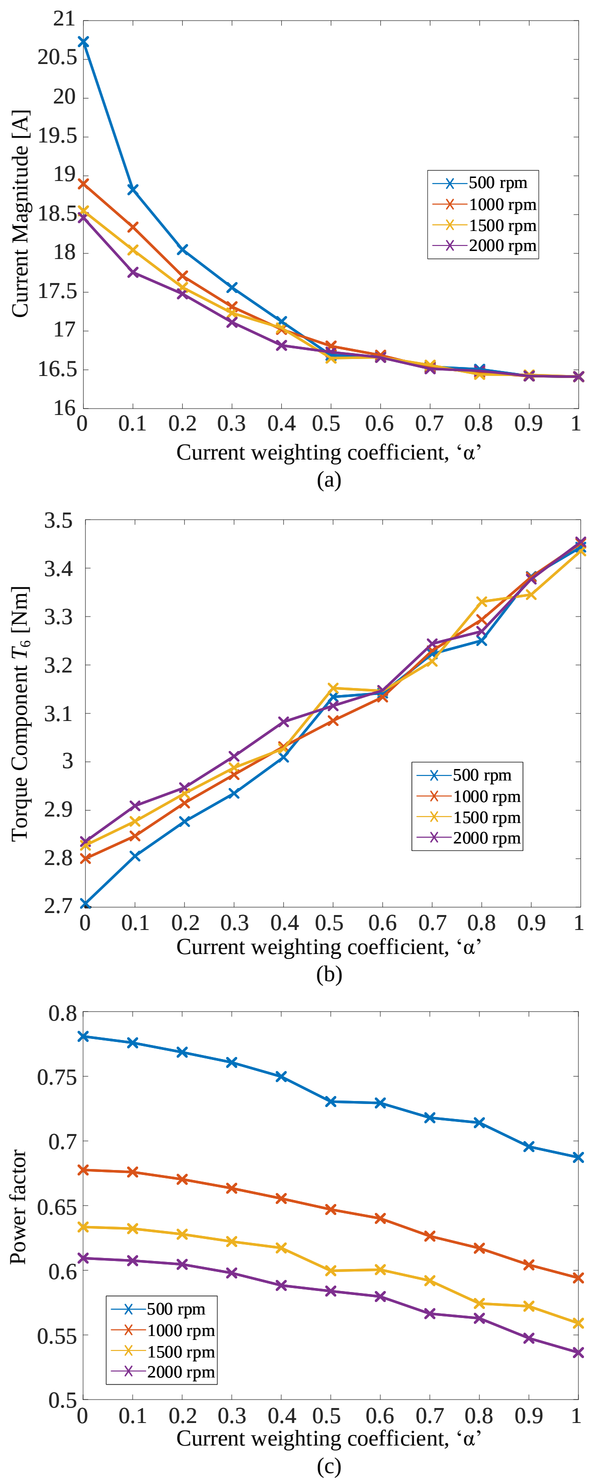

Figure 7.12: The variation of (a) phase current magnitude, (b) torque component T_6, and (c) power factor with the current weighting coefficient α for T_{avg}=3Nm.

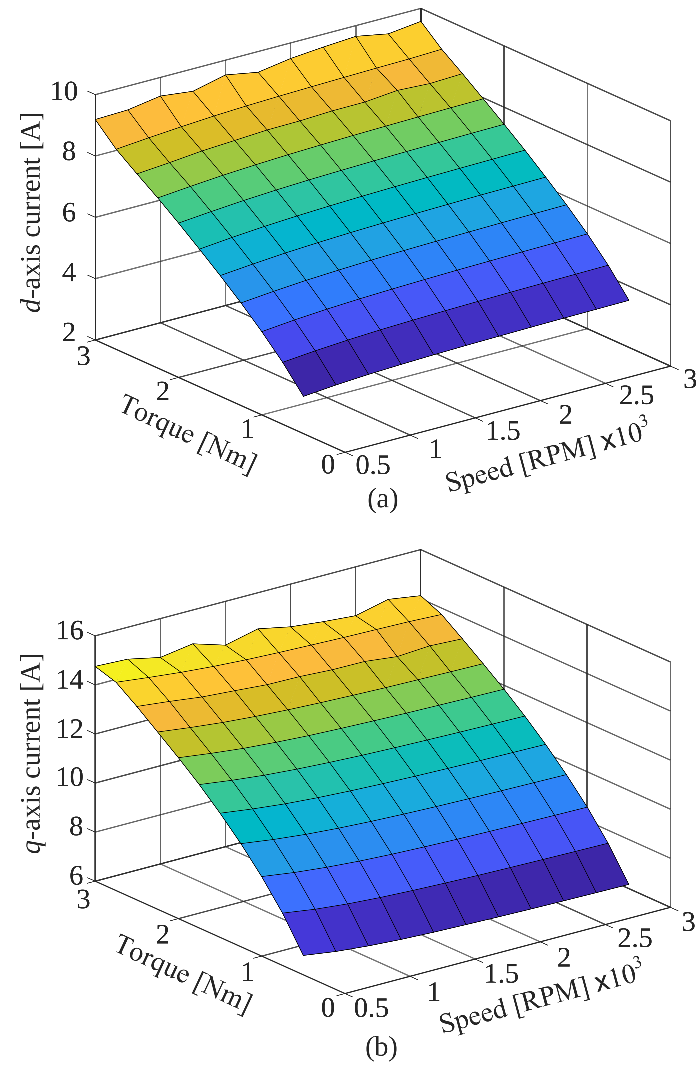

Figure 7.13: a) d-axis current reference and b) q-axis current reference as a function of torque and speed.

because we know that zero torque can be generated by setting i_d or i_q or both of them to zero. It can be concluded from figure 7.13 that the reference phase currents are defined by two values only which are the d- and q-axis currents unlike current shaping techniques in CSRM where the phase current is defined instantaneously at each rotor position which results in huge LUTs.

Now, we know what should be the values of i_d^* and i_q^* to have the desired performance. The LUTs in figure 7.13 is integrated with the model in figure 6.3 and the final model is presented in figure 7.14. To sum up the LUTs in figure 7.14, The optimized control has two 12x12 LUTs: one for the reference direct-axis current and the second one for the reference quadrature-axis current. The harmonic compensation method has two 10x10 LUTs for each harmonic component, thus the total number of LUTs used for the harmonic compensation are 12 LUTs. That may sound as a large number of LUTs, however, the size of those 12 LUTs are 10x10 only due to the vector modeling. I also reduced the size of the LUTs to 7x7 instead of 10x10, and I found that the effectiveness of the harmonic compensation method is not affected. Therefore, although the number of the LUTs is large, the total size of those LUTs is small.

7.5 Experimental Results and Discussion

For the experimental validation, the same setup in chapter 5 is used.

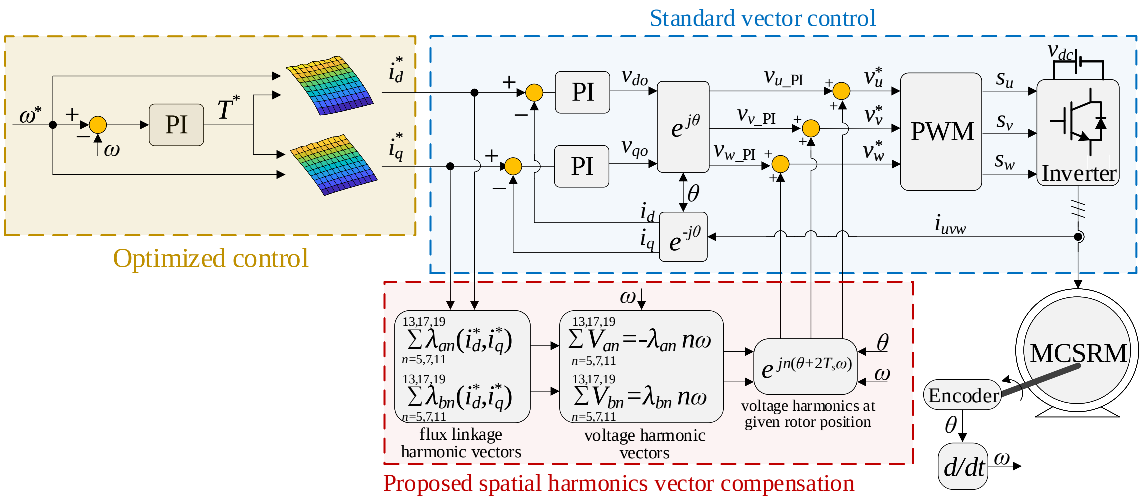

Figure 7.14: a) d-axis current reference and b) q-axis current reference as a function of torque and speed.

7.5.1 MCSRM performance at 1000 rpm

First, the performance of the MCSRM was evaluated at 1000 rpm for the rated torque of $T_{avg} = 3$Nm. Four operating conditions have been tested: (1) the maximum torque per ampere for $\alpha = 1$, (2) the maximum power factor for $\alpha = 0$, (3) the minimum torque ripple, and (4) the optimized operation for $\alpha = 0.4$. Figure 7.15 shows phase u current and the torque waveform for these four operating points. Table 7.1 summarizes the motor performances at those operating points. Figure 7.15, the results are presented in a single figure to show the difference between the current and torque waveforms at different operating conditions. Since the test results are obtained separately in individual experiments for each operating point, the phase shift between the current and torque waveforms could not be shown.

It can be noticed from table 7.1 and figure 7.15 that the operating point corresponding to the minimum torque ripple has the minimum T_6 of 2.6Nm among all the tested operating points. But, it also has the largest magnitude of phase current at

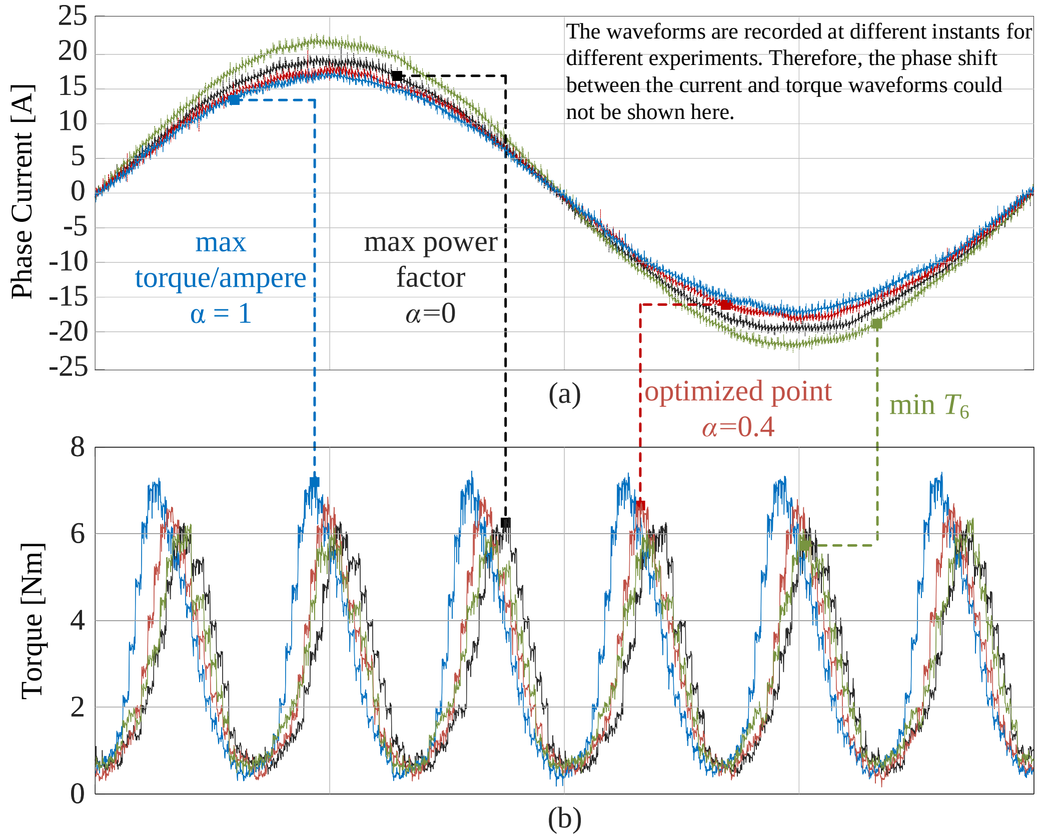

Figure 7.15: Experimental results at 1000 rpm and 3Nm: (a) Phase u current, and (b) electro-magnetic torque, time scale: (4ms/div)

21.2A, which is the motor rated current. The maximum torque per ampere operating point has the smallest magnitude of phase current, which is 16.4A. However, it has the highest T_6 of 3.4Nm and the lowest power factor of 0.59. The operating point corresponding to the maximum power factor has the highest power factor of 0.69 and approximately the same minimum T_6 of 2.7Nm with a phase current of 18.7A. The optimized operating point has a power factor of 0.65 with a torque ripple of 2.7Nm and a phase current of 17A. Therefore, the optimized operating point provides a combination of high power factor, low torque ripple, and low phase current magnitude. Table 7.1 also shows that the power factor calculated from the experimental current and voltage waveforms is in good agreement with the power factor calculated from equation (7.3.3).

The real and reactive power in table 7.1 for each operating point are calculated from equation (7.3.3). It can be observed that the maximum power factor operating point and the optimized operating point draw approximately 11% lower reactive power as compared to the maximum torque per ampere operating point and the minimum torque ripple operating point. The reduction in the reactive power could help reducing the DC-link capacitance.

The motor efficiency η in table 7.1 for each operating point is calculated as:

$$\eta = \frac{T_e w_{mech}}{P}, \quad w_{mech} = \frac{2\pi N_{rpm}}{60} \tag{7.5.1}$$

where w_{mech} is the mechanical angular frequency, N_{rpm} is the motor speed in rpm, and P is the real power calculated from equation (7.3.3). It can be observed that the motor efficiency is directly proportional to the magnitude of the phase current. Hence, the minimum phase current operating point has the highest efficiency and the minimum torque ripple operating point has the lowest efficiency, as it has the highest phase current magnitude. Although the efficiency of the optimized point is 3% less than the highest efficiency, it has lower torque ripple and higher power factor. The poor performance of the MCSRM is due to the motor topology as the MCSRM used in this thesis is originally designed to operate as a conventional SRM with single-phase excitation.

Table 7.1: MCSRM Performance at 1000 rpm

Case	$[i_d, i_q]$(A)	I_m(A)	P(W)	Q(Var)	$cos(\phi)$ Experimental	$cos(\phi)$ Calculated	T_6(Nm)	η(%)
Max torque per ampere (α=1)	[11.5, 11.5]	16.4	425	573	0.59	0.59	3.4	74
Max power factor (α=0)	[8, 17.1]	18.9	470	510	0.69	0.68	2.7	67
Min torque ripple	[7, 20]	21.2	517	575	0.67	0.67	2.6	61
Optimized point (α=0.4)	[8.9, 15.3]	17	441	508	0.65	0.66	2.8	71

7.5.2 MCSRM performance at 1500 rpm

The performance of the MCSRM is also tested at 1500 rpm. Figures 7.16 to 7.19 shows phase u current and torque waveforms of the maximum torque per ampere operating point, maximum power factor operating point, minimum torque ripple operating point and the optimized operating point. Table 7.2 summarizes the experimental results for those four operating points. The higher speed results in higher induced emf and hence, lower power factor compared to the 1000 rpm. The operating points corresponding to the maximum torque per ampere and the minimum torque ripple at 1500 rpm draw the same current for the same average torque and deliver the same torque ripple as in 1000 rpm operation. This is because the average torque and torque ripple are functions of d- and q- axis currents and they are independent of the motor speed. Table 7.2 shows that the optimized operating point has lower T_6, lower phase current, and higher power factor. Table 7.2 also shows that the power factor predicted from equation (7.3.3) matches closely with the power factor calculated from the experiments.

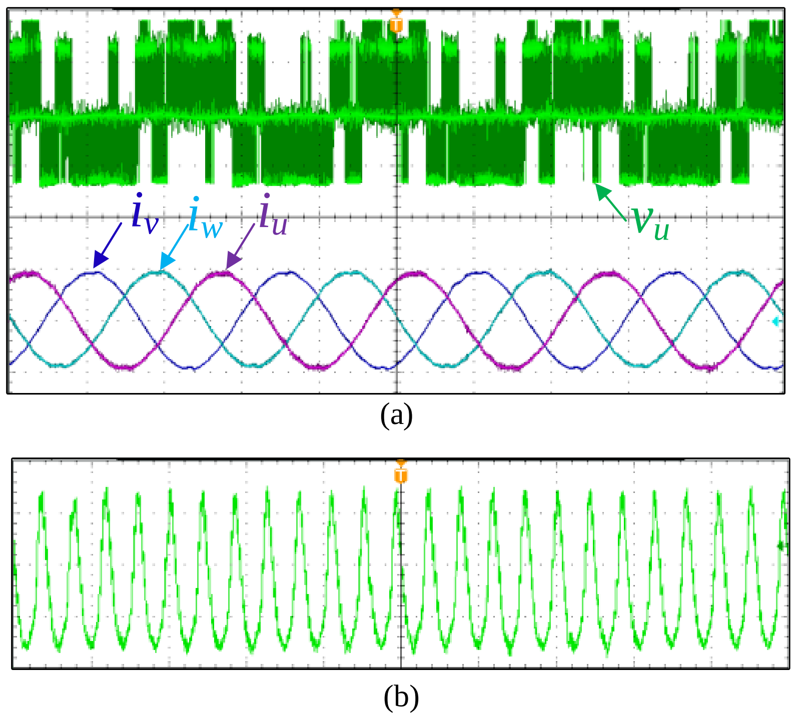

Figure 7.16: Waveforms corresponding to the maximum torque per ampere at 1500 rpm and 3Nm (a) Phase u voltage and the 3-phase currents, and (b) the electro-magnetic torque at 1500 rpm and 3Nm. Voltage scale: (50V/div), current scale: (20A/div), torque scale: (2Nm/div), time scale: (4ms/div)

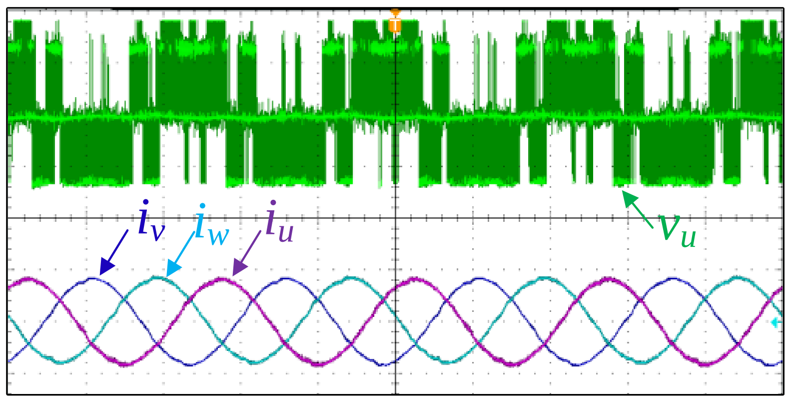

(a)

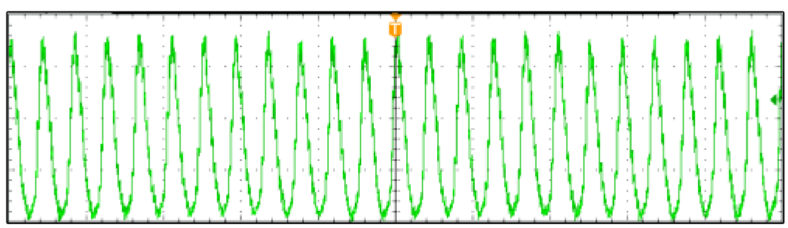

(b)

Figure 7.17: Waveforms corresponding to the maximum power factor at 1500 rpm and 3Nm (a) Phase u voltage and the 3-phase currents, and (b) the electro-magnetic torque at 1500 rpm and 3Nm. Voltage scale: (50V/div), current scale: (20A/div), torque scale: (2Nm/div), time scale: (4ms/div)

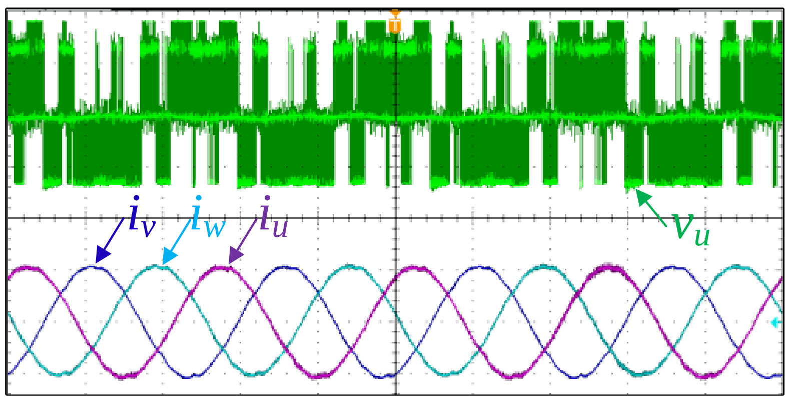

(a)

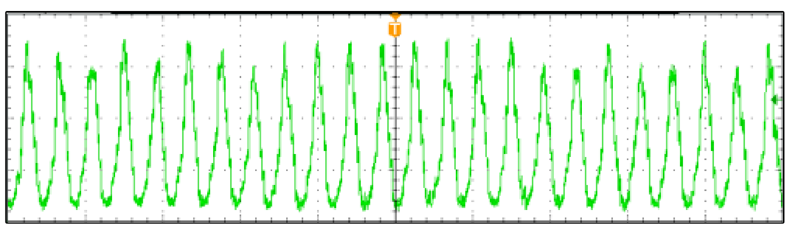

(b)

Figure 7.18: Waveforms corresponding to the minimum torque ripple (T_6) at 1500 rpm and 3Nm (a) Phase u voltage and the 3-phase currents, and (b) the electro-magnetic torque. Voltage scale: (50V/div), current scale: (20A/div), torque scale: (2Nm/div), time scale: (4ms/div)

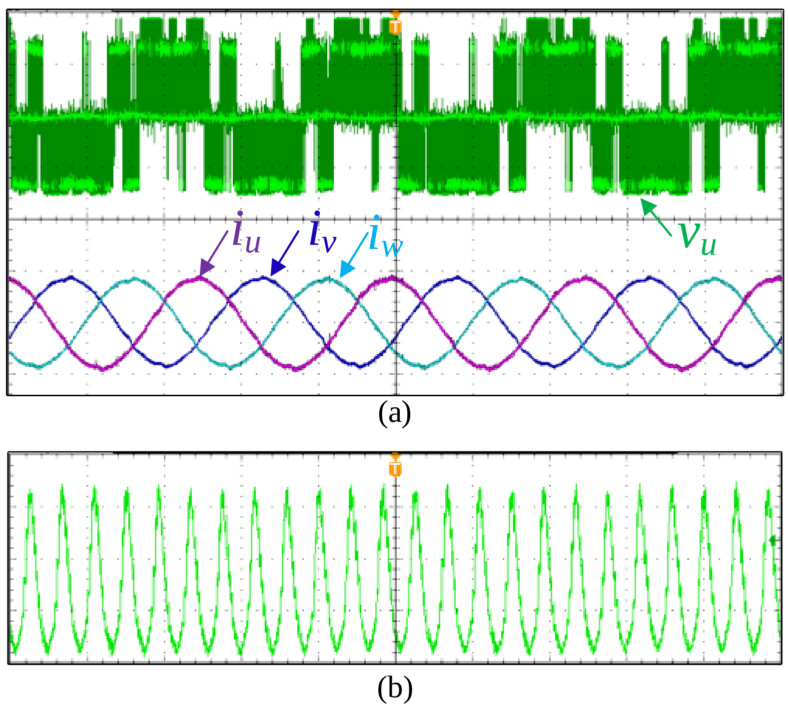

Figure 7.19: Waveforms corresponding to the optimized point at 1500 rpm and 3Nm (a) Phase u voltage and the 3-phase currents, and (b) the electro-magnetic torque. Voltage scale: (50V/div), current scale: (20A/div), torque scale: (2Nm/div), time scale: (4ms/div)

Table 7.2: MCSRM Performance at 1500 rpm

Case	$[i_d, i_q]$(A)	I_m(A)	P(W)	Q(Var)	$cos(\phi)$ Experimental	$cos(\phi)$ Calculated	T_6(Nm)	η(%)
Max torque per ampere (α=1)	[11.5, 11.5]	16.4	582	859	0.55	0.56	3.4	81
Max power factor (α=0)	[8.2, 16.6]	18.5	624	762	0.63	0.63	2.7	76
Min torque ripple	[7, 20]	21.2	675	862	0.62	0.62	2.6	70
Optimized point (α=0.4)	[9, 15.1]	17	598	763	0.61	0.62	2.8	79

7.6 summary

Torque ripple and power factor of MCSRMs with sinusoidal currents excitation are investigated in this chapter. Torque ripple in MCSRM is mainly due to the 6^{th} order harmonic of the torque waveform. Hence, reducing the 6^{th} order harmonic can significantly reduce the torque ripple. Power factor reflects the saturation level of MCSRM, and it depends on both the magnitude and angle of the current phasor. When the stator poles of phase u are aligned with the rotor poles, the maximum power factor is achieved when the current phasor is aligned with the stator poles of another phase which generates torque in the positive rotation direction. The position of the current phasor at the aligned position is defined by the current excitation angle. Therefore, the maximum power factor is achieved when the current excitation angle is $60°$ for the 3-phase 12/8 MCSRM. Simulation results show that the excitation angle corresponding to the maximum power factor deviates slightly from $60°$ due to the real power loss in phase resistance.

An optimized control of MCSRM is presented which aims to reduce the torque ripple and increase the power factor. Optimization results reveal that the operating point corresponding to the minimum torque ripple has the largest magnitude of phase current. Additionally, the operating point corresponding to the minimum phase current has the maximum torque ripple. The optimization results show that optimizing the power factor results in low torque ripple; therefore, the applied objective function includes the phase current and power factor only. The weighting coefficients of phase current and the power factor are selected so that the optimized operating point has lower phase current, lower torque ripple, and higher power factor. The proposed method is also validated by experimental results.

Chapter 8

Conclusions, Future Work and Publications

8.1 Conclusions

Mutually coupled SRMs (MCSRMs) with sinusoidal current excitation merge the advantages of SRMs which are the simple and robust structure, with the advantages of AC motors which are using the standard AC motor drives, such as the 2-level voltage source inverter and vector control with the regular modulation schemes such as the space vector modulation or sinusoidal pulse width modulation. The challenges of MCSRMs with sinusoidal current excitation are:

1. A flexible and less complicated dynamic model is required.
2. Spatial harmonics elimination of phase currents.
3. The selection of the reference direct-and quadrature-axis currents to optimize the motor performance in terms of efficiency, torque ripple, and power factor.

In regard to the first challenge, the most accurate modeling method for MCSRMs is based on look-up tables (LUTs), where those LUTs and the simulated currents in the FEA model represent two quadrants of the dq frame. That method is improved in chapter 5 so that the simulated currents in the FEA model represent only a single dq quadrant and, hence, the number of FEA steps and size of LUTs are reduced by 50%. In the proposed method, the phase current and electro-magnetic torque are represented as vectors in terms of Fourier coefficients. Hence, the dimensions of the LUTs are 2D independent of rotor position, which reduces the size of the LUTs significantly. The proposed modeling method has the minimum error compared to other methods in literature and it is validated by FEA and experiments.

In regard to the second challenge, a spatial harmonics compensation method is introduced to ensure sinusoidal current excitation in chapter 6. In that method, the phase voltage waveform is shaped to obtain the desired sinusoidal currents by injecting the essential voltage harmonics. The required voltage harmonics are calculated from the flux linkage harmonics. The voltage and flux linkage harmonics are represented as vectors in terms of Fourier coefficients in the stationary reference frame. The proposed method is validated at different current levels and different speeds for motoring and generating mode of operation. The proposed harmonic compensation method reduced the THD of phase current to 2%-3%. The proposed method does not influence the system stability since it does not require extra proportional-integral or proportional-resonant controllers.

In regard to the third challenge, the 6^{th} order harmonic is the major component that causes torque ripple in the torque waveform and, hence, reducing the 6^{th} order harmonic reduces the overall torque ripple. Power factor reflects the saturation level in SRMs, unlike CSRMs, the higher magnitude of phase current does not necessary means higher saturation level, while the position of the current phasor in space is important as well, which is referred to as the current excitation angle. In chapter 7, torque ripple and power factor for 3-phase MCSRMs are analysed in details. these analyses are then used to propose an optimized control that aims to reduce torque ripple and to increase the power factor and efficiency. It was also concluded from chapter 7 that the sinusoidal current excitation only is not enough to improve the MCSRM performance, while the design of the motor must be considered to have a high performance.

8.2 Future Work

8.2.1 Current Profile Shaping for MCSRM

Current shaping has been widely investigated for CSRMs to reduce the torque ripple and acoustic noise [35–38]. Similarly, shaping the phase current waveforms in MCSRM, rather than using the standard current waveforms discussed in chapter 3, can improve the motor performance significantly. Current shaping can be based on either dependent or independent phase current control.

8.2.2 Sinusoidal Flux Linkage Excitation

If both phase current and phase flux linkage are sinusoidal waveforms, the instantaneous torque waveform will be free of torque ripples. However, this cannot be achieved in MCSRM due to the salient stucture of the stator and rotor poles. As a result, only the phase flux linkage or the phase current can be sinusoidal and the other will be distorted. In chapter 6, a feedforward control method is introduced to achieve sinusoidal current excitation. The sinusoidal phase current causes a distorted phase flux linkage which in return causes the torque ripples. Instead of achieving sinusoidal current excitation, authors in [19] injected current harmonics randomly to reduce torque ripple by investigating the effect of different current harmonics with different magnitudes. Instead of injecting current harmonics randomly as in [19], certain current harmonics can be injected to generate sinusoidal flux linkage, that can have a lower torque ripple than the sinusoidal current excitation.

8.2.3 Space Vector Modulation Based on Current Controllers

The standard vector control with proportional-integral controllers cannot be used to control current in sections 8.2.1 and 8.2.2 as the phase currents are not sinusoidal waveforms. Hence, the hysteresis current control (HCC) is more effective in those cases, however, The disadvantages of HCC is discussed in chapter 6. Therefore, the best current control method from my point of view for those cases is the SVM-based-HCC [105, 106]. In that control method, the voltage vectors are applied based on the current error from the HCC. It is worth mentioning that when the switching action is dependent on the current error such as the HCC or the SVM-based-HCC, the modulation scheme becomes self-tolerant to inverter switch faults. On the other hand, the switching action in voltage controllers such as the standard vector control is based on the voltage error and the modulation strategy needs to reconfigured at switch fault [107–110].

8.2.4 Other Winding Configurations of MCSRM

As mentioned in section 2.2.2, CSRMs have concentrated winding to maximize the generated MMF for single-phase excitation [6, 14–16]. As a result, all SRMs (CSRM and MCSRM) have concentrated windings. For multi-phase excitation in MCSRMs, distributed winding configurations can provide a better performance in terms of torque density and power factor.

8.2.5 Mechanical Design of MCSRM

As I mentioned before, the SRM used in this thesis is mainly designed to operate as CSRM with single-phase excitation. That justifies the relatively low performance of the SRM shown in table 7.1 and table 7.2. You can think about it as if you excited an induction motor by rectangular waveform current instead of sin waves, the performance of the induction motor will be totally different and degraded. However, in this thesis, I did not only change the current waveform, I also changed the winding configuration to be mutually coupled instead of conventional, and the excitation method to be multi-phase instead of single-phase. Therefore, if the SRM is designed to operate as a mutually coupled SRM with sinusoidal current and multi-phase excitation, the performance of the MCSRM will be significantly improved.

8.2.6 Acoustic Noise and Vibrations of SRM

Acoustic noise and vibrations are important parameters for SRMs and they are due to the radial forces. Therefore, reducing the radial forces results in reducing the acoustic noise. The harmonic components of the radial forces can be modeled as vectors similar to the vector modeling of torque profile. The reduction of the radial forces can be done by reducing the largest harmonic component. That is similar to the torque ripple reduction by reducing the 6^{th} order harmonic.

8.3 Publications

8.3.1 Published Journal papers

1. **P. Azer**, B. Bilgin and A. Emadi, "Mutually Coupled Switched Reluctance Motor: Fundamentals, Control, Modeling, State of the Art Review and Future Trends," in IEEE Access, vol. 7, pp. 100099-100112, July 2019.

2. **P. Azer**, R. Rodriguez, J. Guo, J. Gareau, J. Bauman, B. Bilgin, and A. Emadi,

"Time Efficient Integrated Electro-Thermal Model for a 60 kW 3-Phase Bidirectional Synchronous DC-DC Converter," in IEEE Transactions on Industry Applications, vol. 56, no. 1, pp. 654-668, Jan. 2020.

3. **P. Azer**, S. Ouni and M. Narimani, "A Novel Fault-Tolerant Technique For Active Neutral Point Clamped Inverter Using Carrier-Based PWM," in IEEE Transactions on Industrial Electronics, vol. 67, no. 3, pp. 1792-1803, March 2020.

4. **P. Azer**, and A. Emadi, "Generalized State Space Average Model for Multi-Phase Interleaved Buck, Boost and Buck-Boost DC-DC Converters: Transient, Steady-State and Switching Dynamics," in IEEE Access, vol. 8, pp. 77735-77745, April 2020.

5. J. Guo, R. Rodriguez, , J. Gareau, D. Schumacher, M. Alizadeh, **P. Azer**, J. Bauman, B. Bilgin, and A. Emadi, "A Comprehensive Analysis for High-Power Density, High-Efficiency 60kW Interleaved Boost Converter Design for Electrified Powertrains," in IEEE Transactions on Vehicular Technology, available in early access.

8.3.2 Journal papers under review

1. **P. Azer**, B. Howey, B. Bilgin, and A. Emadi, "Dynamic Vector Modeling of Three-Phase Mutually Coupled Switched Reluctance Machines with Single dq-Quadrant Look-up Tables", submitted to IEEE Transactions on Power Electronics.

2. **P. Azer**, and A. Emadi, "Model-Based Spatial Harmonics Vector Compensation Method for Three-Phase Mutually Coupled Switched Reluctance Machine With Sinusoidal Current Excitation", submitted to IEEE Open Journal of Power Electronics.

3. **P. Azer**, B. Bilgin and A. Emadi, "Optimized Control for Three-Phase Mutually Coupled Switched Reluctance Machine Controlled by Sinusoidal Currents", submitted to IEEE Transactions on Power Electronics.

8.3.3 Published Conference papers

1. **P. Azer**, S. Ouni, and M. Narimani, "Fault-Tolerant Method For 5-Level Active Neutral Point Clamped Inverter Using Sinusoidal PWM," 2019 IEEE Energy Conversion Congress and Expo (ECCE), Baltimore, MD, 2019, pp. 2985-2990.

2. **P. Azer** and J. Bauman, "An Asymmetric Three-Level T-Type Converter for Switched Reluctance Motor Drives in Hybrid Electric Vehicles," 2019 IEEE Transportation Electrification Conference and Expo (ITEC), Detroit, MI, USA, 2019, pp. 1-6.

3. **P. Azer**, S. Ouni and M. Narimani, "A New Fault-Tolerant Method For Four-level Neutral Point Clamped Inverter Based on Sinusoidal PWM," 2019 IEEE 28th International Symposium on Industrial Electronics (ISIE), Vancouver, BC, Canada, 2019, pp. 2009-2014.

4. **P. Azer**, S. Ounie and M. Narimani, "A New Post-Fault Control Method Based on Sinusoidal Pulse Width Modulation Technique for a Neutral Point Clamped

(NPC) Inverter," 2019 IEEE Applied Power Electronics Conference and Exposition (APEC), Anaheim, CA, USA, 2019, pp. 2499-2504.

5. E. Sayed, **P. Azer**, M. Kordic, J. Reimers, B. Bilgin, M. Bakr, and A. Emadi, "Design of a Switched Reluctance Motor for a Pump Jack Application," 2018 IEEE Electrical Power and Energy Conference (EPEC), Toronto, ON, 2018, pp. 1-6.

6. **P. Azer**, J. Ye and A. Emadi, "Advanced Fault-Tolerant Control Strategy for Switched Reluctance Motor Drives," 2018 IEEE Transportation Electrification Conference and Expo (ITEC), Long Beach, CA, 2018, pp. 20-25.

7. **P. Azer**, R. Rodriguez, H. Ge, J. Bauman, P. S. Ravi and A. Emadi, "Time Efficient Integrated Electro-Thermal Model for Bidirectional Synchronous DC-DC Converter in Hybrid Electric Vehicles," 2018 IEEE Transportation Electrification Conference and Expo (ITEC), Long Beach, CA, 2018, pp. 55-62.

Appendices

Appendix A

The Symmetry Between Direct-and Quadrature-axis Flux Linkage and Fourier Coefficients of Phase Current

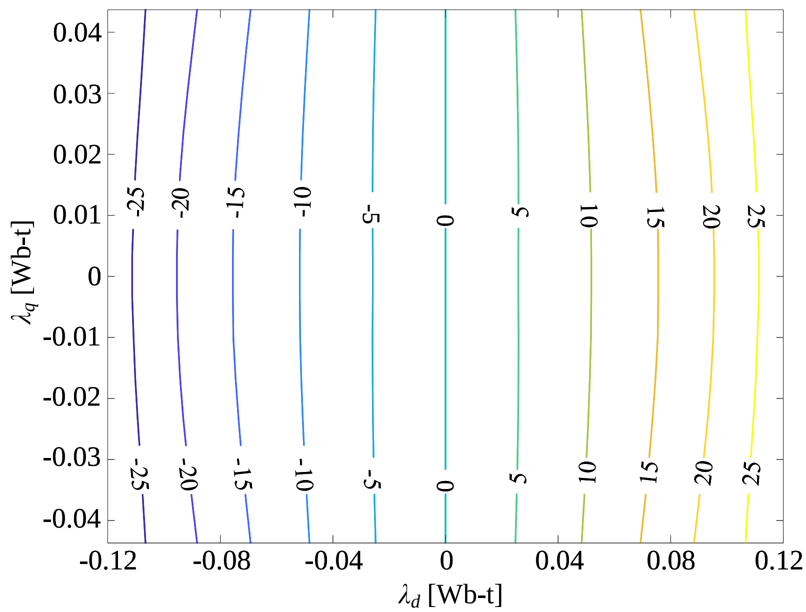

(a)

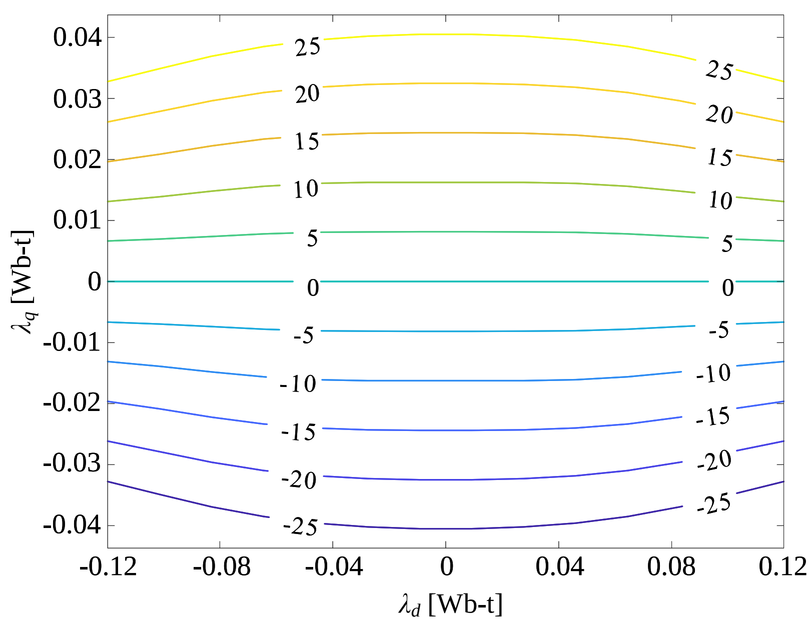

(b)

Figure A.1: 1^{st} order Fourier coefficients of the phase current with respect to dq flux linkages among the four quadrants of the dq frame: (a) I_{a1} and (b) I_{b1}.

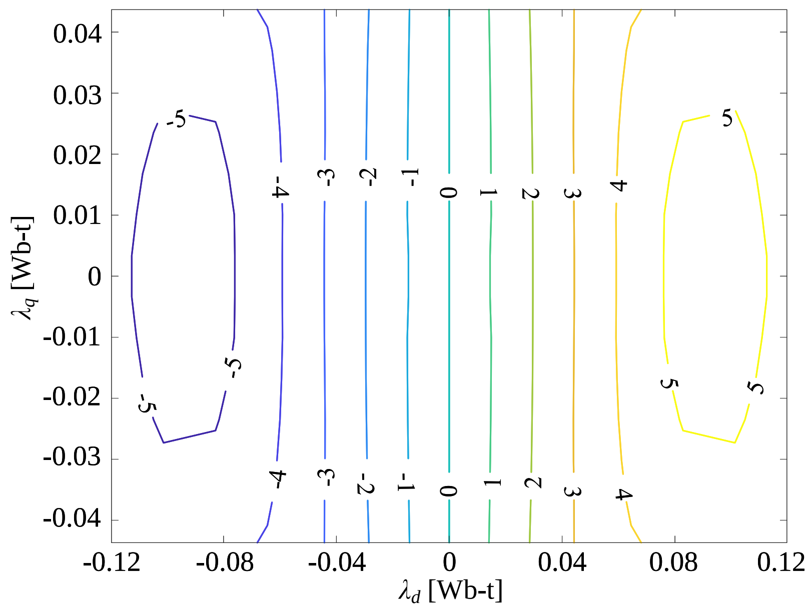

(a)

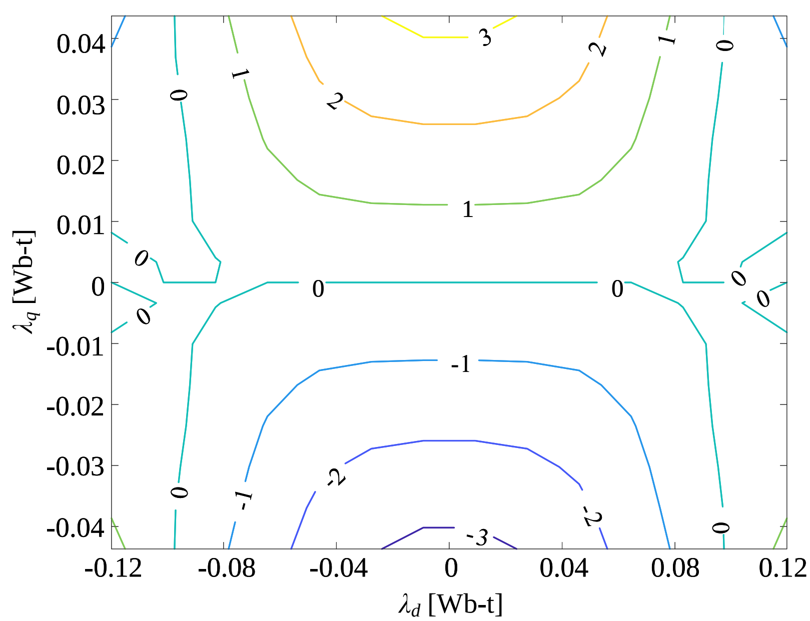

(b)

Figure A.2: 5^{th} order Fourier coefficients of the phase current with respect to dq flux linkages among the four quadrants of the dq frame: (a) I_{a5} and (b) I_{b5}.

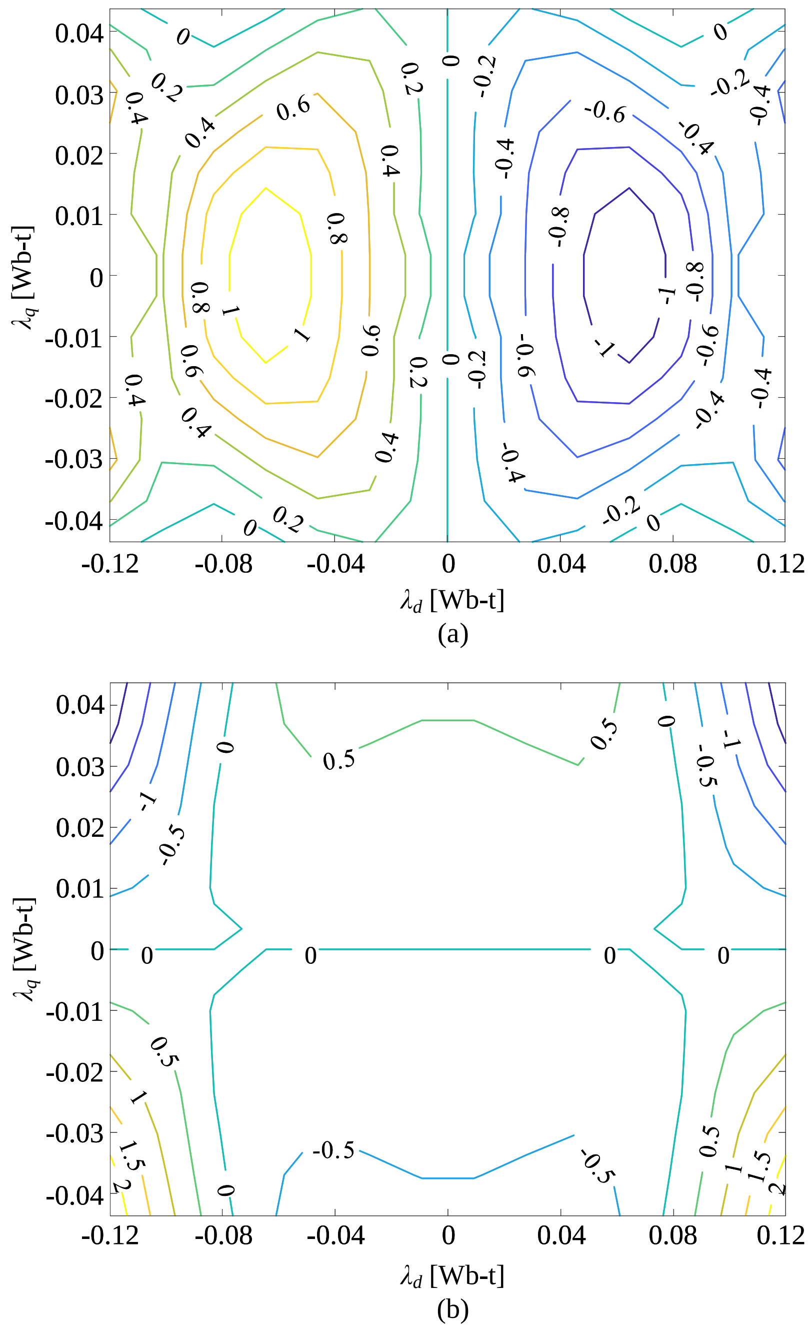

Figure A.3: 7^{th} order Fourier coefficients of the phase current with respect to dq flux linkages among the four quadrants of the dq frame: (a) I_{a7} and (b) I_{b7}.

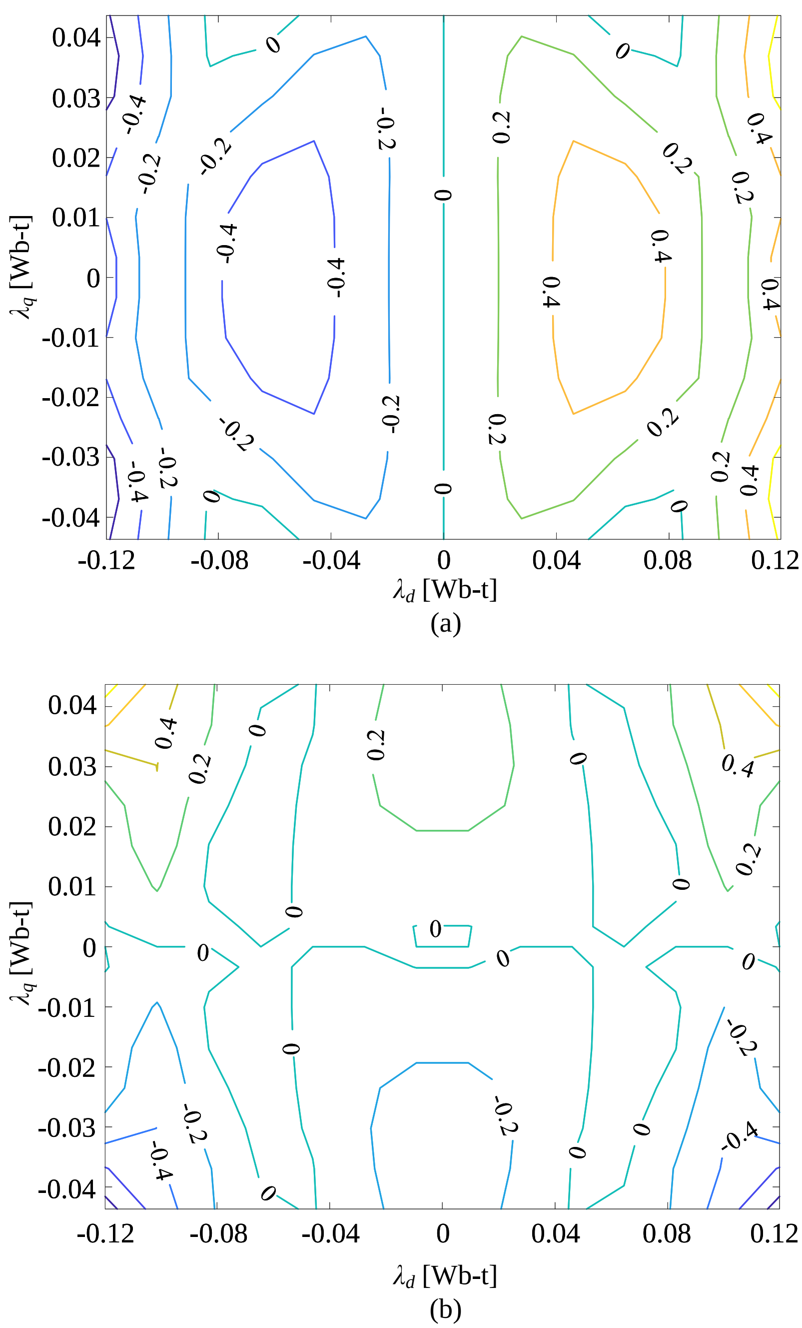

Figure A.4: 11^{th} order Fourier coefficients of the phase current with respect to dq flux linkages among the four quadrants of the dq frame: (a) I_{a11} and (b) I_{b11}.

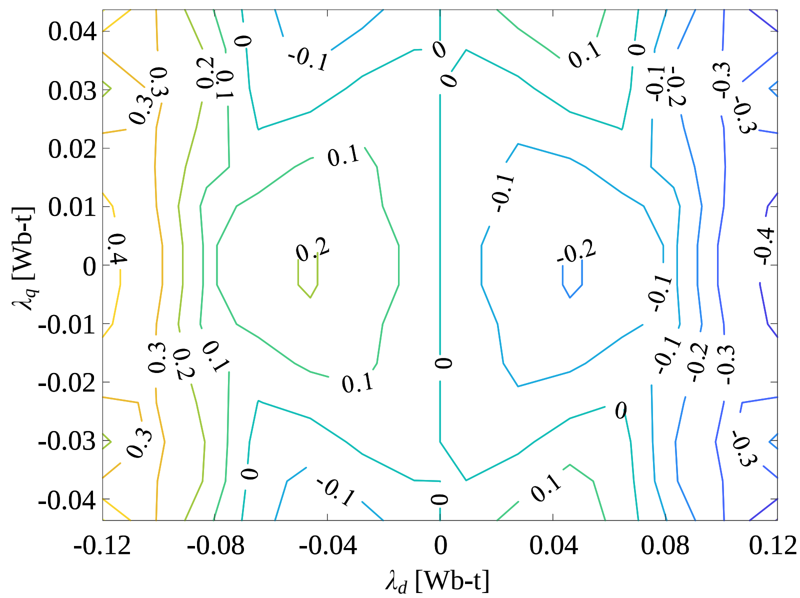

(a)

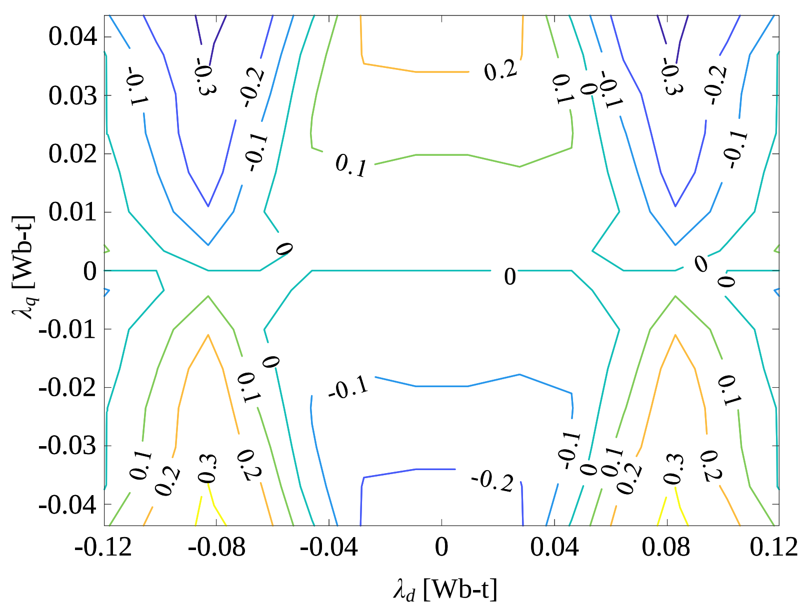

(b)

Figure A.5: 13^{th} order Fourier coefficients of the phase current with respect to dq flux linkages among the four quadrants of the dq frame: (a) I_{a13} and (b) I_{b13}.

Appendix B

The Symmetry Between Direct-and Quadrature-axis Currents and Fourier Coefficients of Electro-magnetic Torque

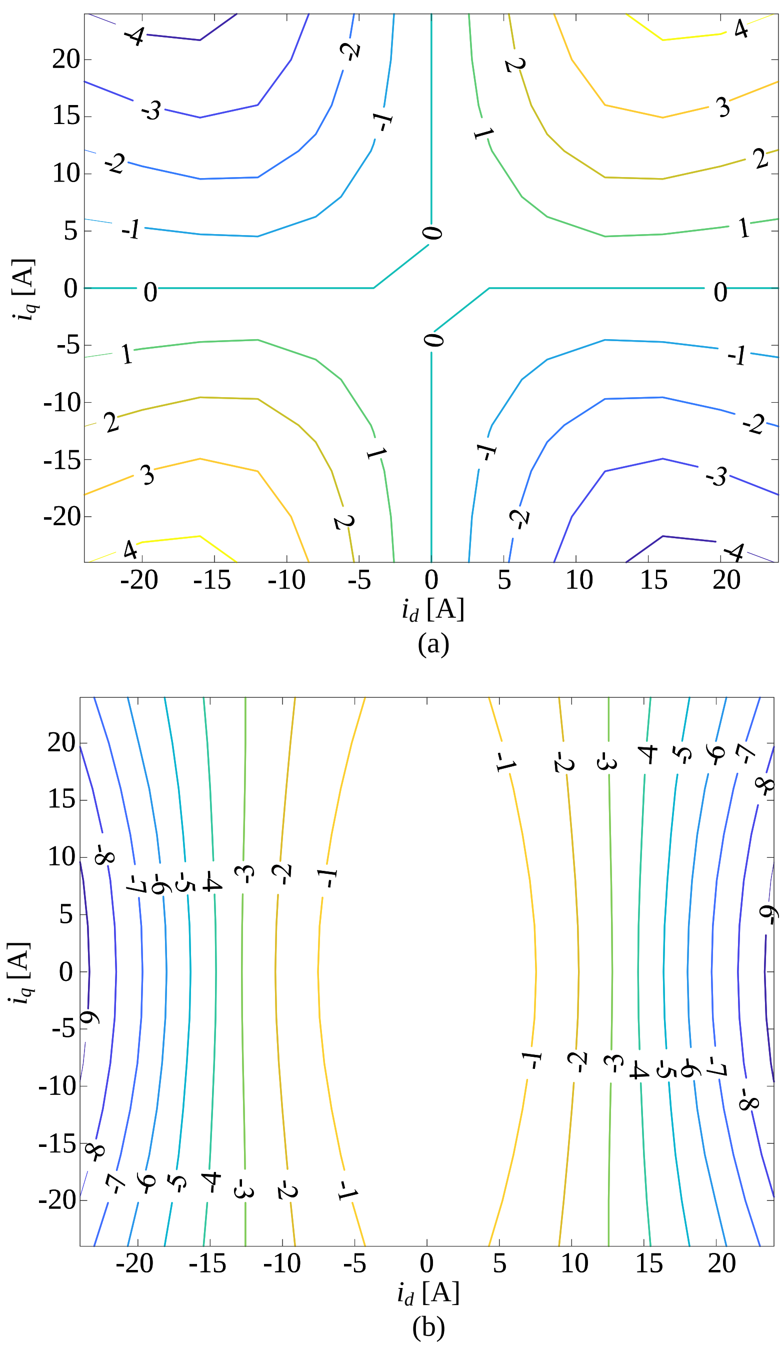

Figure B.1: Fourier coefficients for the 6^{th} harmonic of the torque with respect to dq currents among the four quadrants of the dq frame: (a) T_{a6} and (b) T_{b6}.

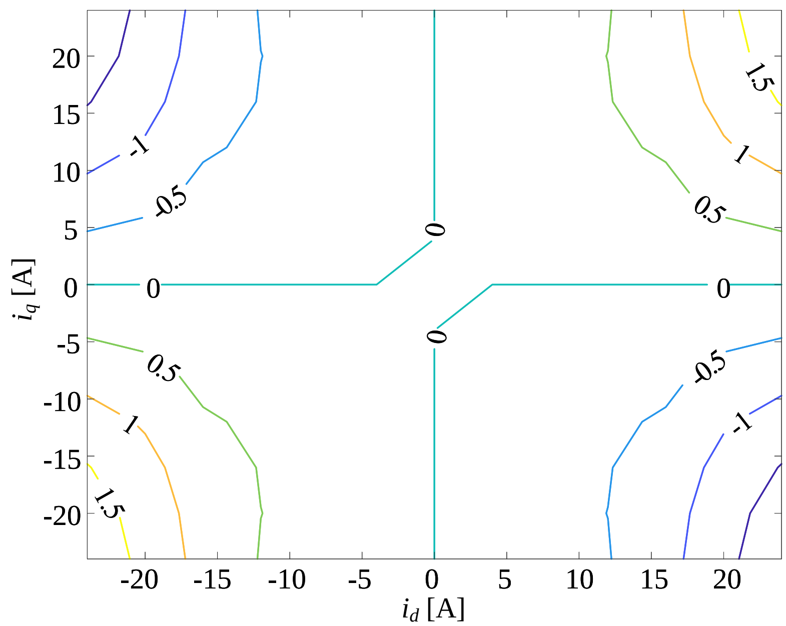

(a)

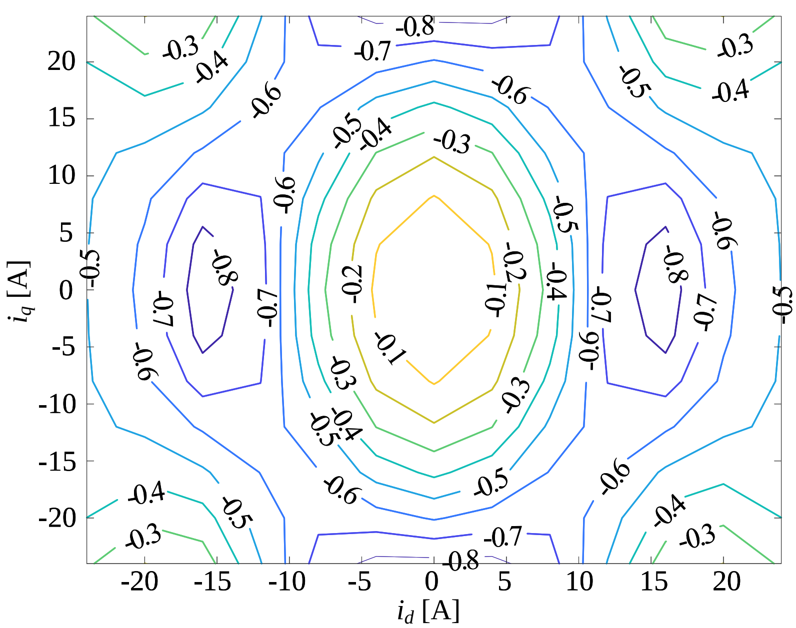

(b)

Figure B.2: Fourier coefficients for the 12^{th} harmonic of the torque with respect to dq currents among the four quadrants of the dq frame: (a) T_{a12} and (b) T_{b12}.

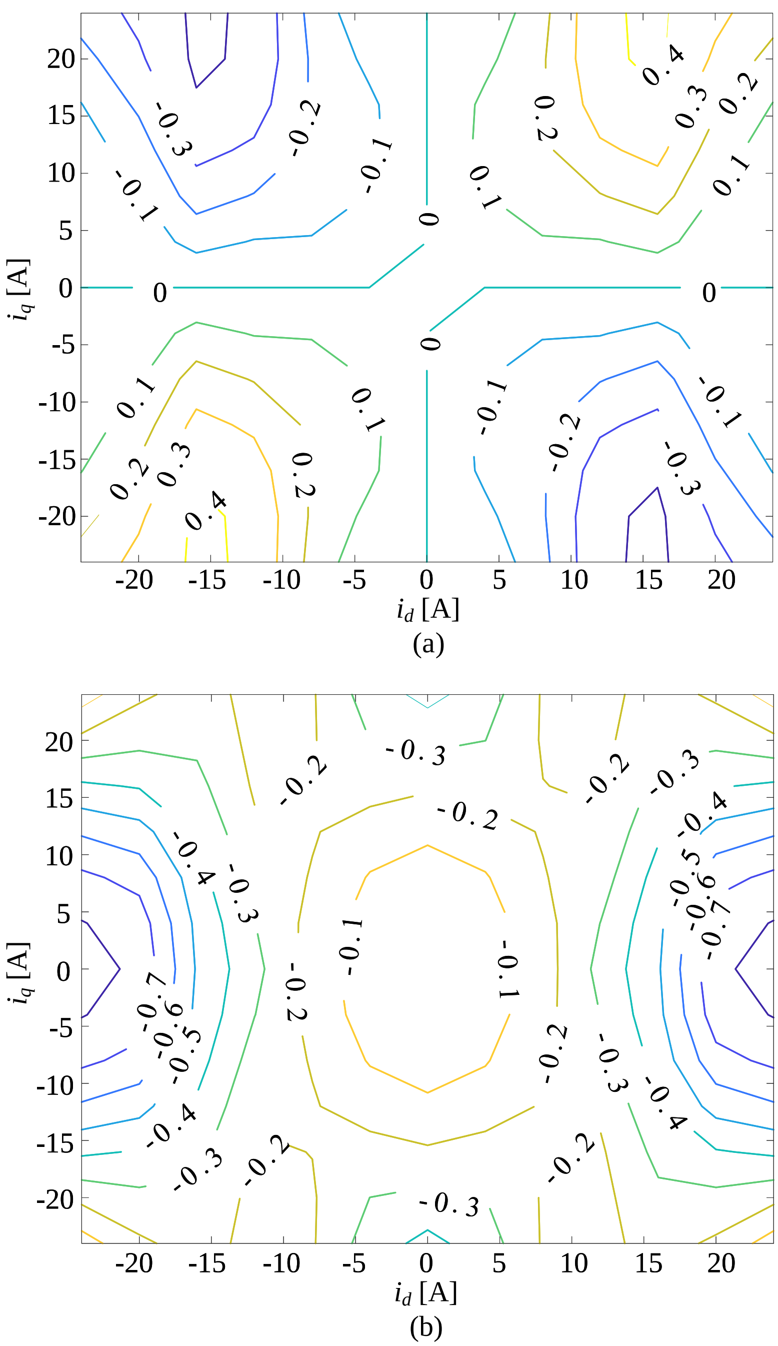

Figure B.3: Fourier coefficients for the 18^{th} harmonic of the torque with respect to dq currents among the four quadrants of the dq frame: (a) T_{a18} and (b) T_{b18}.

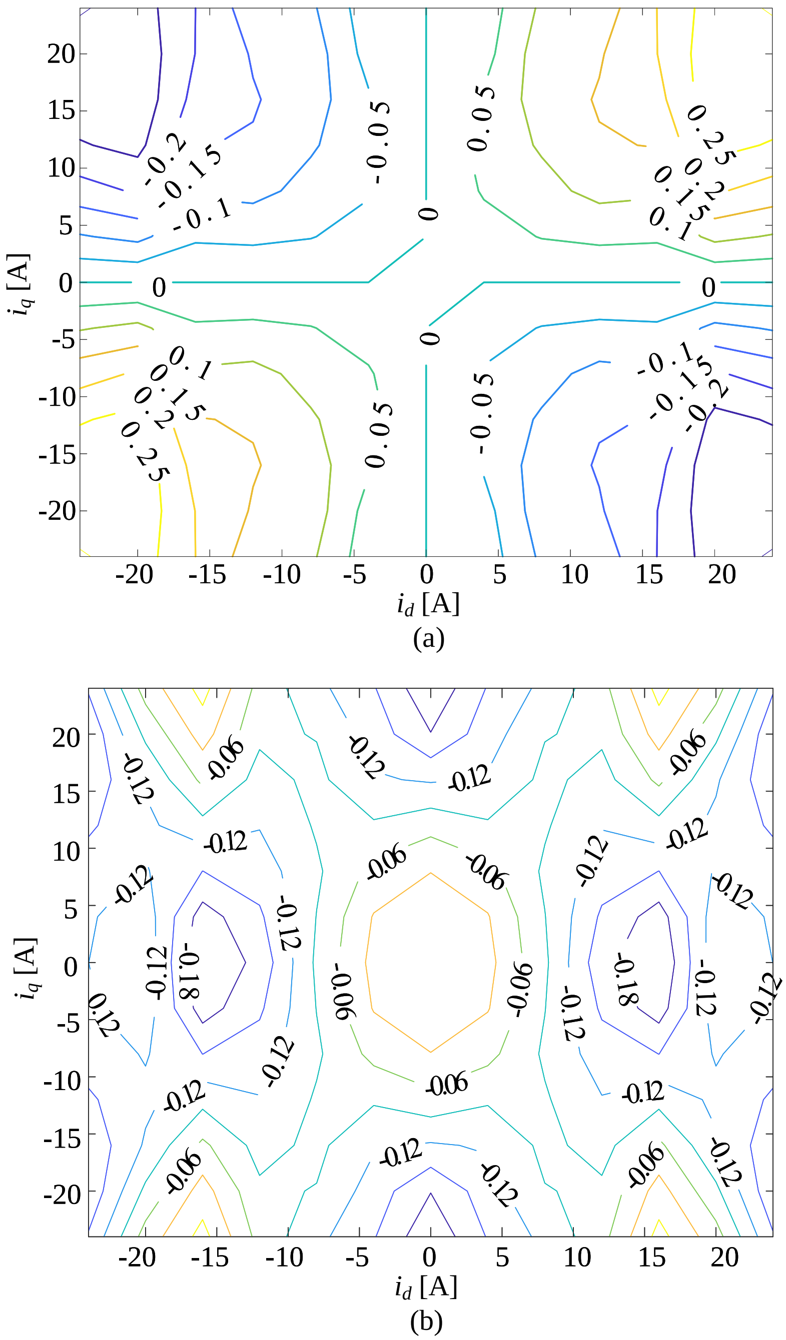

Figure B.4: Fourier coefficients for the 24^{th} harmonic of the torque with respect to dq currents among the four quadrants of the dq frame: (a) T_{a24} and (b) T_{b24}.

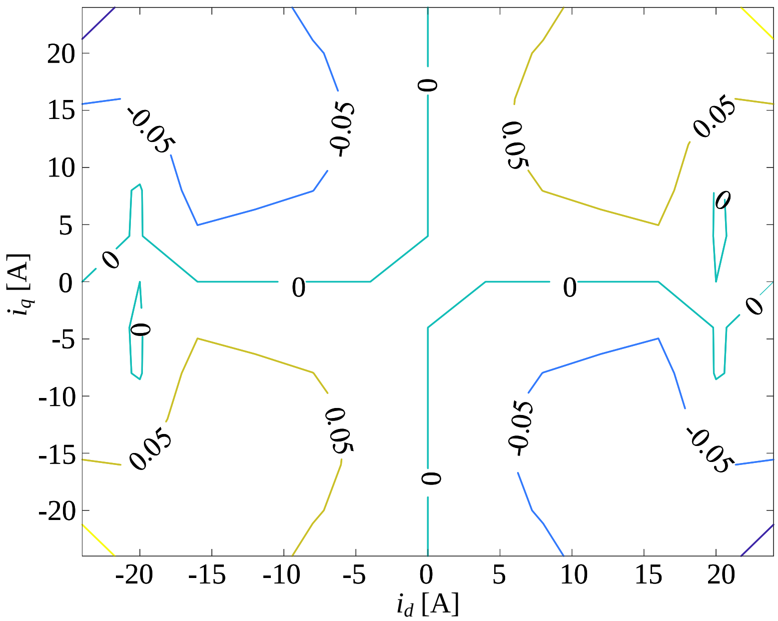

(a)

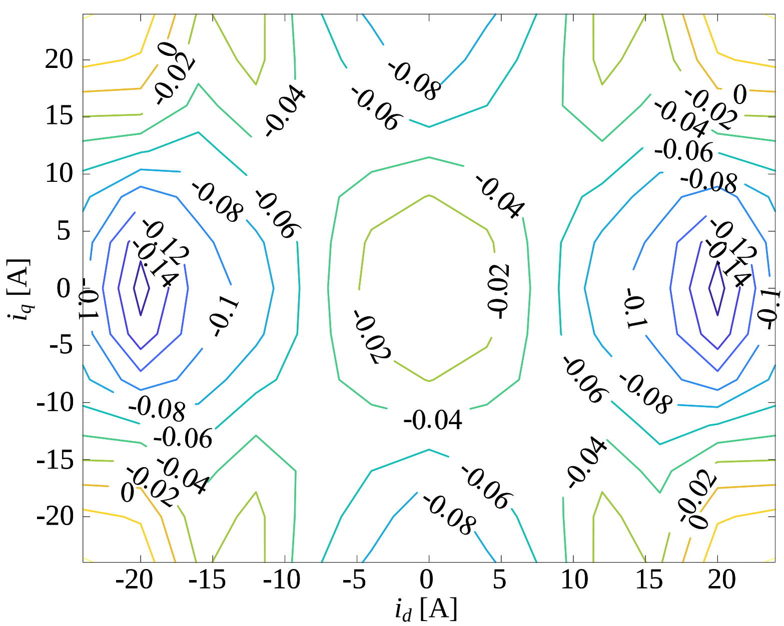

(b)

Figure B.5: Fourier coefficients for the 30^{th} harmonic of the torque with respect to dq currents among the four quadrants of the dq frame: (a) T_{a30} and (b) T_{b30}.

Appendix C

The Symmetry Between Direct-and Quadrature-axis Currents and Fourier Coefficients of Phase Flux Linkage

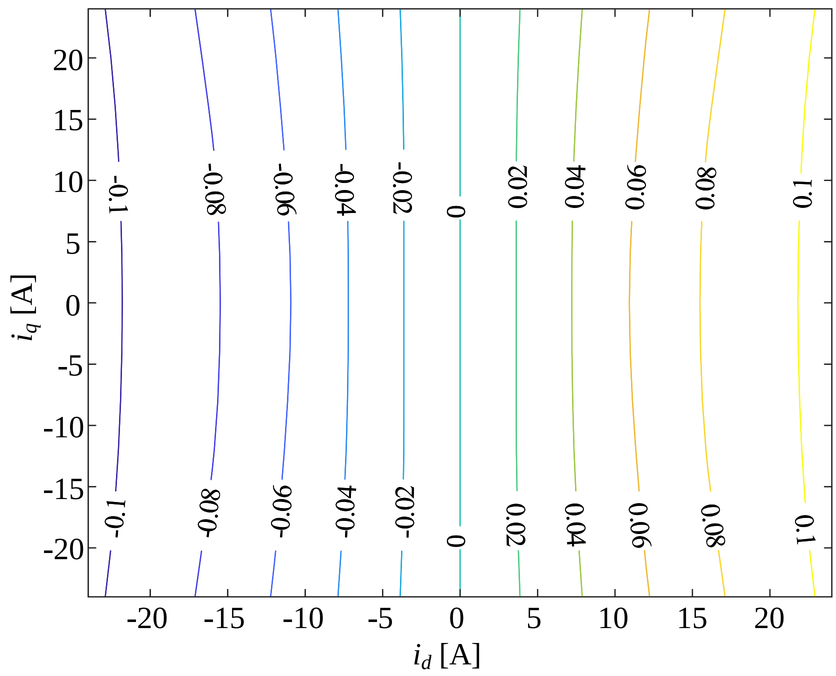

(a)

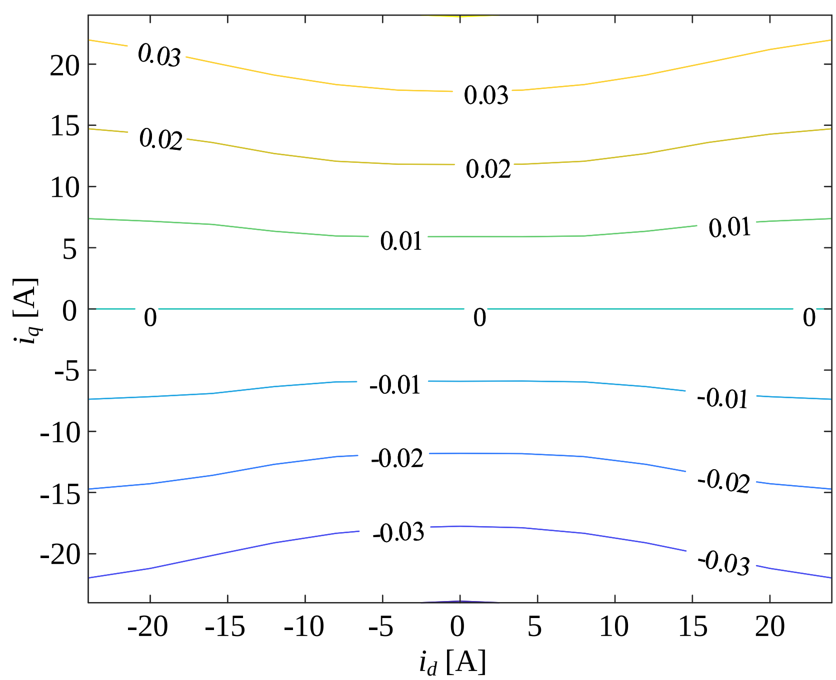

(b)

Figure C.1: 1^{st} order Fourier coefficients of the phase flux linkage with respect to dq currents among the four quadrants of the dq frame: (a) λ_{a1} and (b) λ_{b1}.

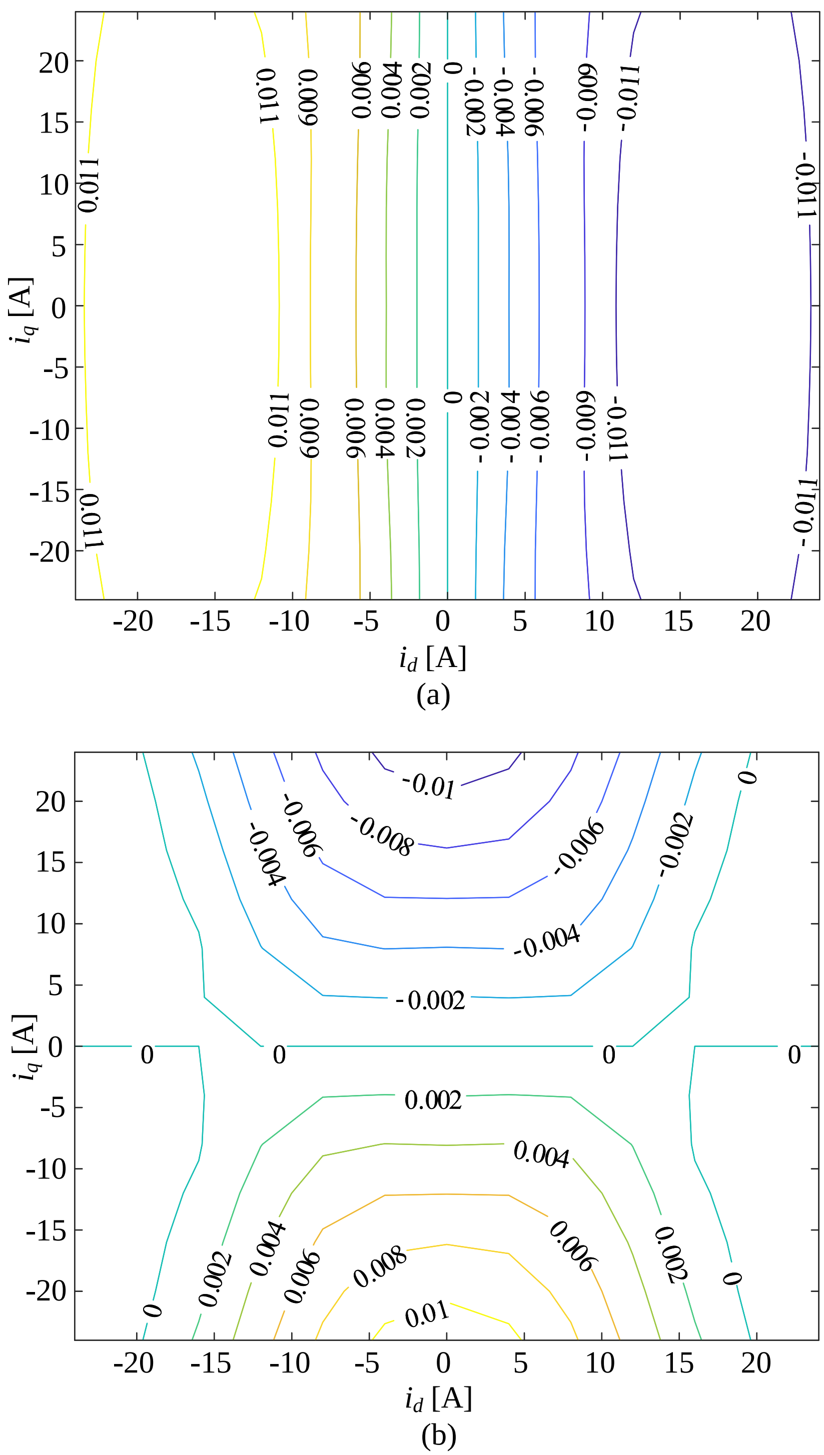

Figure C.2: 5^{th} order Fourier coefficients of the phase flux linkage with respect to dq currents among the four quadrants of the dq frame: (a) λ_{a5} and (b) λ_{b5}.

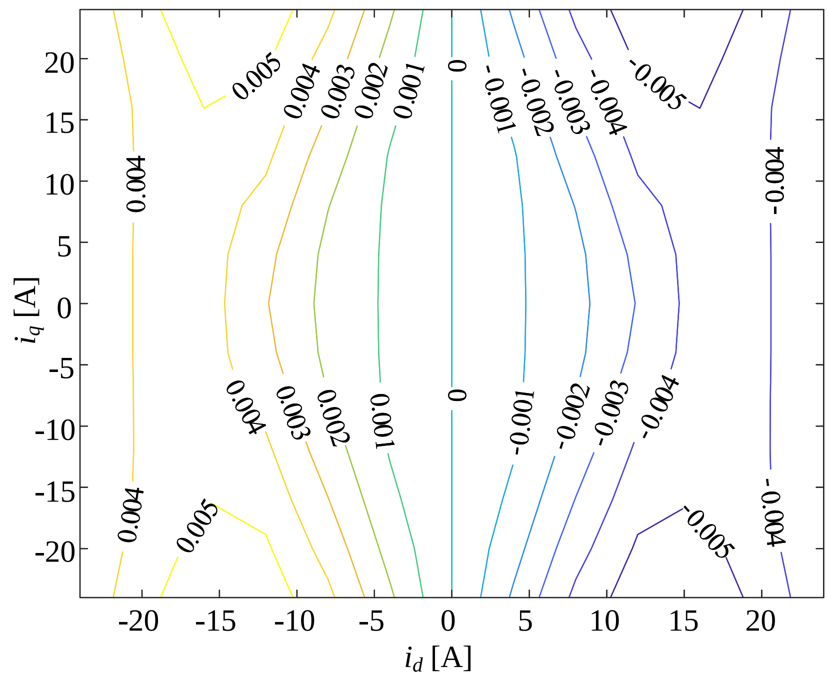

(a)

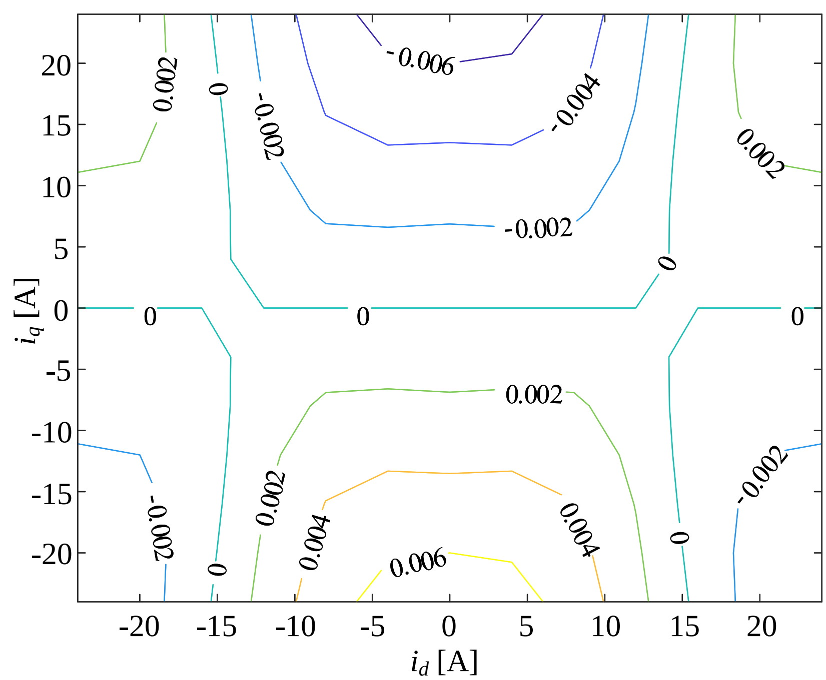

(b)

Figure C.3: 7^{th} order Fourier coefficients of the phase flux linkage with respect to dq currents among the four quadrants of the dq frame: (a) λ_{a7} and (b) λ_{b7}.

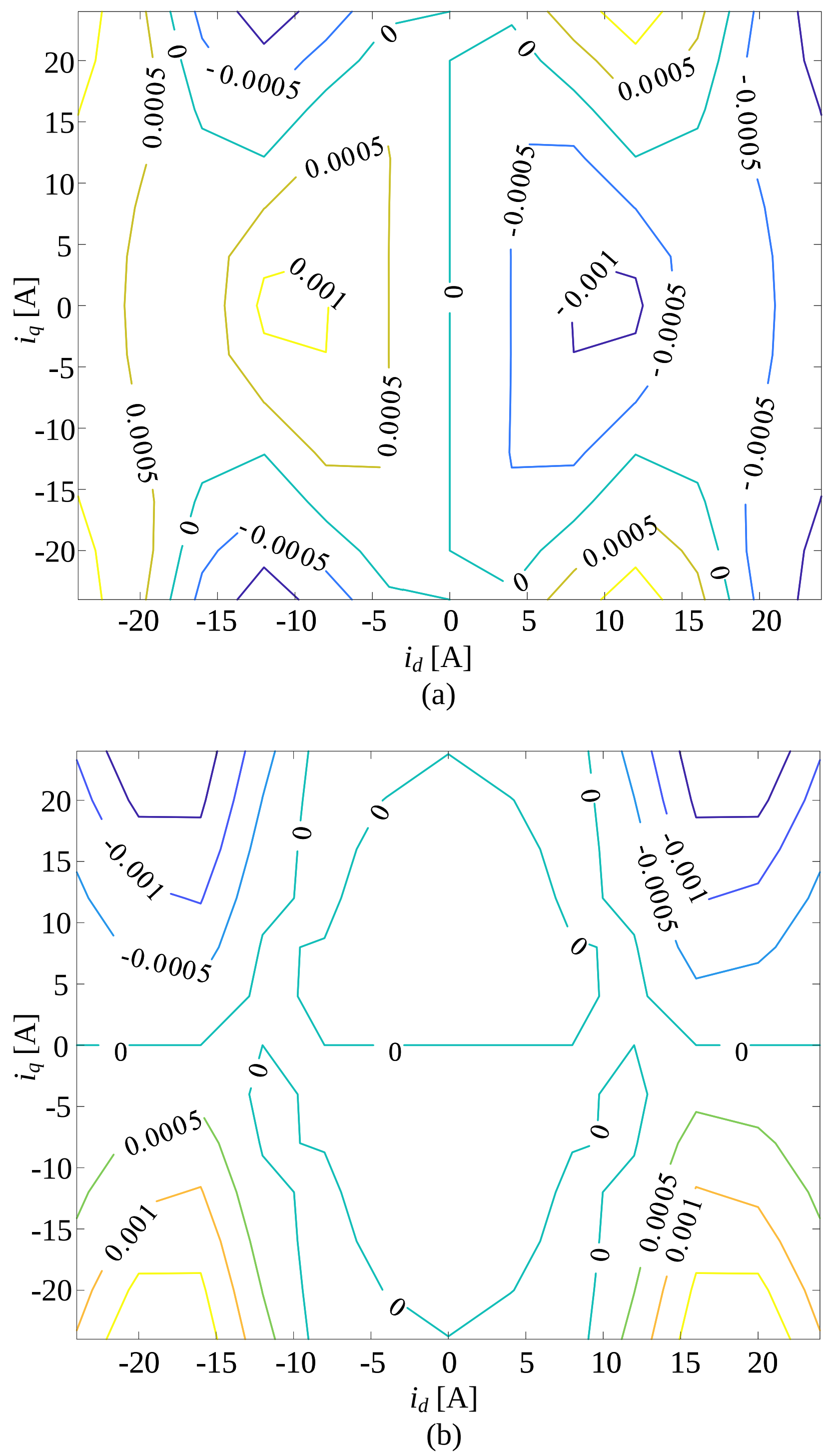

Figure C.4: 11^{th} order Fourier coefficients of the phase flux linkage with respect to dq currents among the four quadrants of the dq frame: (a) λ_{a11} and (b) λ_{b11}.

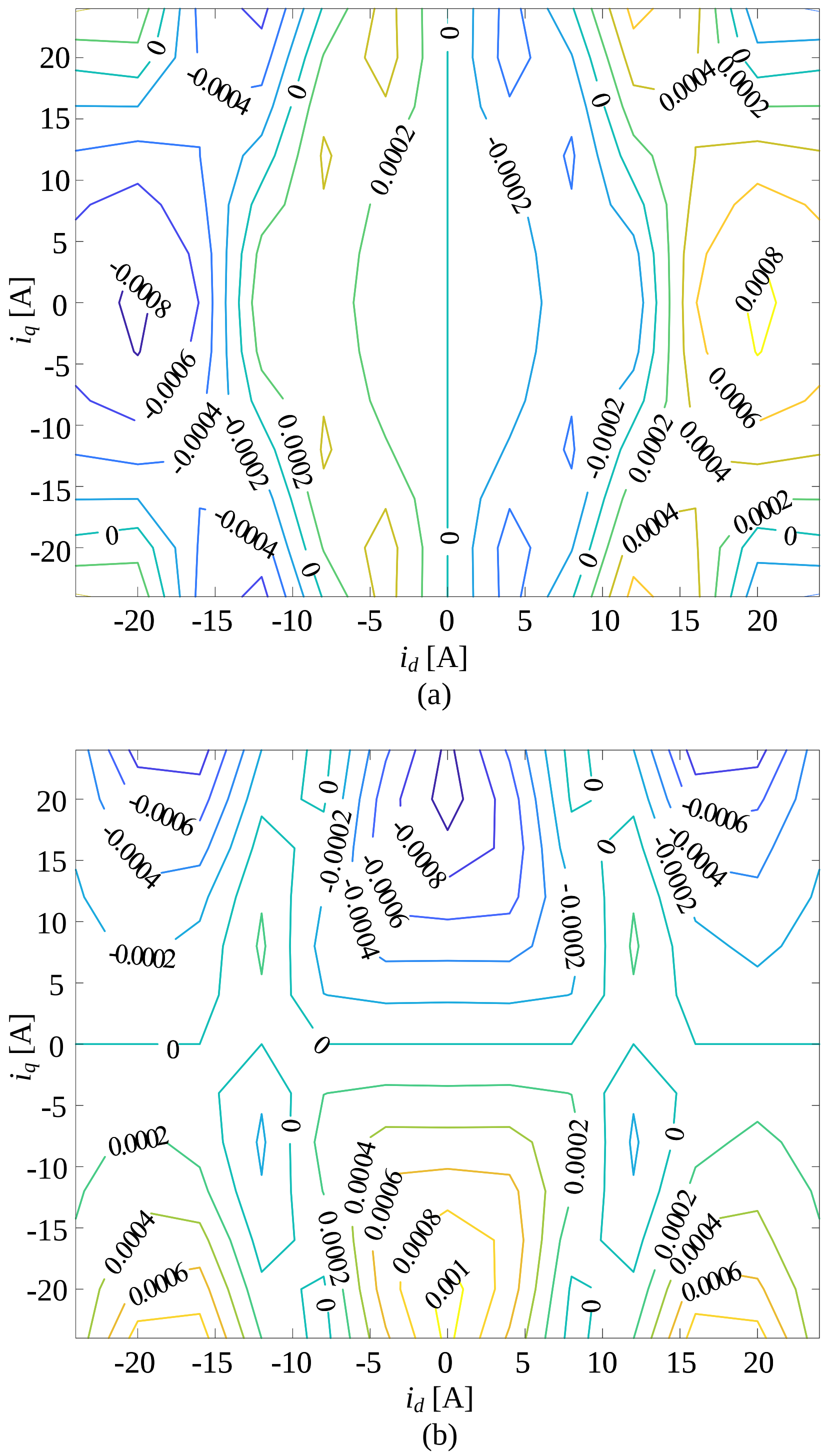

Figure C.5: 13^{th} order Fourier coefficients of the phase flux linkage with respect to dq currents among the four quadrants of the dq frame: (a) λ_{a13} and (b) λ_{b13}.

References

[1] P. J. Lawrenson, J. M. Stephenson, P. T. Blenkinsop, J. Corda, and N. N. Fulton, "Variable-speed switched reluctance motors," *IEE Proceedings B - Electric Power Applications*, vol. 127, no. 4, pp. 253–265, Jul. 1980.

[2] W. F. Ray and R. M. Davis, "Inverter drive for doubly salient reluctance motor: Its fundamental behaviour, linear analysis and cost implications," *IEE Journal on Electric Power Applications*, vol. 2, no. 6, pp. 185–193, Dec. 1979.

[3] S. D. Sudhoff and P. C. Krause, "Analysis of steady-state operation of a multistack variable-reluctance stepper motor using $qd0$ variables," *IEEE Trans. on Energy Conversion*, vol. 6, no. 4, pp. 693–699, Dec. 1991.

[4] P. J. Clarkson and P. P. Acarnley, "Simplified approach to the dynamic modelling of variable-reluctance stepping motors," *IEE Proceedings B - Electric Power Applications*, vol. 136, no. 1, pp. 1–10, Jan. 1989.

[5] S. D. Sudhoff, "Multiple reference frame analysis of a multistack: variable-reluctance stepper motor," *IEEE Trans. on Energy Conversion*, vol. 8, no. 3, pp. 418–424, Sept. 1993.

[6] J. Bernat, J. Kolota, and S. Stepien, "Proportional-integral-derivative position control of variable reluctance stepper motor," in *Proc. VBD International Symposium on Theoretical Electrical Engineering*, Lubeck, Germany, Jun. 2009, pp. 1–4.

[7] M. Ehsani, J. T. Bass, T. J. E. Miller, and R. L. Steigerwald, "Development of a unipolar converter for variable reluctance motor drives," *IEEE Trans. on Industry Applications*, vol. IA-23, no. 3, pp. 545–553, May 1987.

[8] M. Barnes and C. Pollock, "Power electronic converters for switched reluctance drives," *IEEE Trans. on Power Electronics*, vol. 13, no. 6, pp. 1100–1111, Nov. 1998.

[9] H. L. J. Ye and J. W. Jiang, "Control of switched reluctance machines," in *Switched Reluctance Motor Drives: Fundamentals to Applications*, Boca Raton, FL, USA, CRC Press, 2019.

[10] J. Ye, "Power electronic converters to drive switched reluctance machines," in *Switched Reluctance Motor Drives: Fundamentals to Applications*, Boca Raton, FL, USA, CRC Press, 2019.

[11] P. Azer, J. Ye, and A. Emadi, "Advanced fault-tolerant control strategy for switched reluctance motor drives," in *2018 IEEE Transportation Electrification Conference and Expo (ITEC)*, 2018, pp. 20–25.

[12] P. Azer and J. Bauman, "An asymmetric three-level t-type converter for switched reluctance motor drives in hybrid electric vehicles," in *2019 IEEE Transportation Electrification Conference and Expo (ITEC)*, 2019, pp. 1–6.

[13] F. Peng, J. Ye, and A. Emadi, "A digital PWM current controller for switched reluctance motor drives," *IEEE Transactions on Power Electronics*, vol. 31, no. 10, pp. 7087–7098, Oct 2016.

[14] J. W. Finch, H. M. B. Metwally, and J. A. Agber, "Performance prediction in saturated variable reluctance and hybrid motors," in *Proc. IET International Conference on Power Electronics and Variable-Speed Drives*, London, UK, Jul. 1990, pp. 231–236.

[15] J. W. Finch, "Design method for torque estimation in stepping and switched reluctance motors," in *Proc. IET Colloquium on Stepper Motors and Their Control*, Jan. 1994, pp. 3/1–3/3.

[16] B. C. Mecrow, "Fully pitched-winding switched-reluctance and stepping-motor arrangements," *IEE Proceedings B - Electric Power Applications*, vol. 140, no. 1, pp. 61–70, Jan. 1993.

[17] X. Liang, G. Li, J. Ojeda, M. Gabsi, and Z. Ren, "Comparative study of classical and mutually coupled switched reluctance motors using multiphysics finite-element modeling," *IEEE Trans. on Industrial Electronics*, vol. 61, no. 9, pp. 5066–5074, Sept. 2014.

[18] G. J. Li, Z. Q. Zhu, X. Y. Ma, and G. W. Jewell, "Comparative study of torque production in conventional and mutually coupled SRMs using frozen permeability," *IEEE Trans. on Magnetics*, vol. 52, no. 6, pp. 1–9, Jun. 2016.

[19] G. J. Li, K. Zhang, Z. Q. Zhu, and G. W. Jewell, "Comparative studies of torque performance improvement for different doubly salient synchronous reluctance

machines by current harmonic injection," *IEEE Trans. on Energy Conversion*, vol. 34, no. 2, pp. 1094–1104, Jun. 2019.

[20] G. J. Li, X. Y. Ma, G. W. Jewell, Z. Q. Zhu, and P. L. Xu, "Influence of conduction angles on single-layer switched reluctance machines," *IEEE Trans. on Magnetics*, vol. 52, no. 12, pp. 1–11, Dec. 2016.

[21] X. Y. Ma, G. J. Li, G. W. Jewell, Z. Q. Zhu, and H. L. Zhan, "Performance comparison of doubly salient reluctance machine topologies supplied by sinewave currents," *IEEE Trans. on Industrial Electronics*, vol. 63, no. 7, pp. 4086–4096, Jul. 2016.

[22] P. Azer, B. Bilgin, and A. Emadi, "Mutually coupled switched reluctance motor: Fundamentals, control, modeling, state of the art review and future trends," *IEEE Access*, vol. 7, pp. 100 099–100 112, 2019.

[23] J. W. Ahn, S. G. Oh, J. W. Moon, and Y. M. Hwang, "A three-phase switched reluctance motor with two-phase excitation," *IEEE Trans. on Industry Applications*, vol. 35, no. 5, pp. 1067–1075, Sept. 1999.

[24] G. J. Li, J. Ojeda, E. Hoang, M. Lecrivain, and M. Gabsi, "Comparative studies between classical and mutually coupled switched reluctance motors using thermal-electromagnetic analysis for driving cycles," *IEEE Trans. on Magnetics*, vol. 47, no. 4, pp. 839–847, Apr. 2011.

[25] J. M. Kokernak and D. A. Torrey, "Magnetic circuit model for the mutually coupled switched-reluctance machine," *IEEE Trans. on Magnetics*, vol. 36, no. 2, pp. 500–507, Mar. 2000.

[26] B. C. Mecrow, "New winding configurations for doubly salient reluctance machines," *IEEE Trans. on Industry Applications*, vol. 32, no. 6, pp. 1348–1356, Nov. 1996.

[27] Y. Xu and D. A. Torrey, "Study of the mutually coupled switched reluctance machine using the finite element-circuit coupled method," *IEE Proceedings - Electric Power Applications*, vol. 149, no. 2, pp. 81–86, Mar. 2002.

[28] W. Uddin and Y. Sozer, "Analytical modeling of mutually coupled switched reluctance machines under saturation based on design geometry," *IEEE Trans. on Industry Applications*, vol. 53, no. 5, pp. 4431–4440, Sept. 2017.

[29] B. C. Mecrow, C. Weiner, and A. C. Clothier, "The modeling of switched reluctance machines with magnetically coupled windings," *IEEE Trans. on Industry Applications*, vol. 37, no. 6, pp. 1675–1683, Nov. 2001.

[30] M. A. Kabir and I. Husain, "Design of mutually coupled switched reluctance motors (MCSRMs) for extended speed applications using 3-phase standard inverters," *IEEE Trans. on Energy Conversion*, vol. 31, no. 2, pp. 436–445, Jun. 2016.

[31] Y. Li and Y. Tang, "Switched reluctance motor drives with fractionally-pitched winding design," in *Proc. IEEE Power Electronics Specialists Conference*, Saint Louis, MO, USA, Jun. 1997, pp. 875–880.

[32] T. Husain, W. Uddin, and Y. Sozer, "Performance comparison of short-pitched and fully pitched switched reluctance machines over wide speed operations,"

IEEE Trans. on Industry Applications, vol. 54, no. 5, pp. 4278–4287, Sept. 2018.

[33] G. Li, J. Ojeda, S. Hlioui, E. Hoang, M. Lecrivain, and M. Gabsi, "Modification in rotor pole geometry of mutually coupled switched reluctance machine for torque ripple mitigating," *IEEE Transactions on Magnetics*, vol. 48, no. 6, pp. 2025–2034, June 2012.

[34] Brock Howey, Berker Bilgin, and Ali Emadi, "Design of a mutually coupled external-rotor direct drive e-bike switched reluctance motor," *IET Electrical Systems in Transportation*, vol. 10, no. 1, pp. 89–95, Mar. 2020.

[35] V. P. Vujicic, "Minimization of torque ripple and copper losses in switched reluctance drive," *IEEE Trans. on Power Electronics*, vol. 27, no. 1, pp. 388–399, Jan. 2012.

[36] P. L. Chapman and S. D. Sudhoff, "Design and precise realization of optimized current waveforms for an 8/6 switched reluctance drive," *IEEE Trans. on Power Electronics*, vol. 17, no. 1, pp. 76–83, Jan. 2002.

[37] A. D. Callegaro, B. Bilgin, and A. Emadi, "Radial force shaping for acoustic noise reduction in switched reluctance machines," *IEEE Trans. on Power Electronics*, vol. 34, no. 10, pp. 9866–9878, Oct. 2019.

[38] H. Li, B. Bilgin, and A. Emadi, "An improved torque sharing function for torque ripple reduction in switched reluctance machines," *IEEE Trans. on Power Electronics*, vol. 34, no. 2, pp. 1635–1644, Feb. 2019.

[39] B. Howey, "Non-coupled and mutually coupled switched reluctance machines for an e-bike traction application: Pole configurations, design, and comparison," Ph.D. dissertation, McMaster University, Hamilton, Canada, Aug. 2018.

[40] X. Liu, Z. Q. Zhu, M. Hasegawa, A. Pride, R. Deodhar, T. Maruyama, and Z. Chen, "Performance comparison between unipolar and bipolar excitations in switched reluctance machine with sinusoidal and rectangular waveforms," in *Proc. IEEE Energy Conversion Congress and Exposition*, Phoenix, AZ, USA, Sept. 2011, pp. 1590–1595.

[41] P. Krause, O. Wasynczuk, S. D. Sudhoff, and S. Pekarek, "Synchronous machines," in *Analysis of Electric Machinery and Drive Systems, 3rd Edition*, Hoboken, NJ, USA, Wiley-IEEE Press, 2013.

[42] A. C. Clothier, "Switched reluctance motor drives with fully pitched windings," Ph.D. dissertation, Newcastle University, Newcastle, UK, Sept. 2001.

[43] M. A. Kabir and I. Husain, "Hybrid excitation topologies for three-phase mutually coupled reluctance machine with standard inverters," in *Proc. IEEE Power Energy Society General Meeting*, Denver, CO, USA, Jul. 2015, pp. 1–5.

[44] G. J. Li, X. Ojeda, S. Hlioui, E. Hoang, M. Gabsi, and C. Balpe, "Comparative study of switched reluctance motors performances for two current distributions and excitation modes," in *Proc. Annual conference of IEEE Industrial Electronics*, Porto, Portugal, Nov. 2009, pp. 4047–4052.

[45] M. Mohseni and S. M. Islam, “A new vector-based hysteresis current control scheme for three-phase PWM voltage-source inverters,” *IEEE Trans. on Power Electronics*, vol. 25, no. 9, pp. 2299–2309, Sept. 2010.

[46] A. Tilli and A. Tonielli, “Sequential design of hysteresis current controller for three-phase inverter,” *IEEE Trans. on Industrial Electronics*, vol. 45, no. 5, pp. 771–781, Oct 1998.

[47] Bong-Hwan Kwon, Byung-Duk Min, and Jang-Hyoun Youm, “An improved space-vector-based hysteresis current controller,” *IEEE Trans. on Industrial Electronics*, vol. 45, no. 5, pp. 752–760, Oct 1998.

[48] X. B. Liang, G. J. Li, J. Ojeda, M. Gabsi, and Z. Ren, “Comparative study of vibration and acoustic noise between classical and mutually coupled switched reluctance motors,” in *Proc. IEEE International Conference on Electrical Machines*, Marseille, France, Sept. 2012, pp. 2955–2960.

[49] Y. Chen and K. M. Smedley, “A cost-effective single-stage inverter with maximum power point tracking,” *IEEE Trans. on Power Electronics*, vol. 19, no. 5, pp. 1289–1294, Sept. 2004.

[50] A. M. Michaelides and C. Pollock, “Modelling and design of switched reluctance motors with two phases simultaneously excited,” *IEE Proceedings - Electric Power Applications*, vol. 143, no. 5, pp. 361–370, Sept. 1996.

[51] C. Ma, L. Qu, and Z. Tang, “Torque ripple reduction for mutually coupled switched reluctance motor by bipolar excitations,” in *Proc. IEEE International*

Electric Machines Drives Conference, Chicago, IL, USA, May 2013, pp. 1211–1217.

[52] C. Ma and L. Qu, "Design considerations of switched reluctance motors with bipolar excitation for low torque ripple applications," in *Proc. IEEE Energy Conversion Congress and Exposition*, Denver, CO, USA, Sept. 2013, pp. 926–933.

[53] J. Park, S. Jung, and J. Ha, "Variable time step control for six-step operation in surface-mounted permanent magnet machine drives," *IEEE Trans. on Power Electronics*, vol. 33, no. 2, pp. 1501–1513, Feb. 2018.

[54] Y. Kwon, S. Kim, and S. Sul, "Six-step operation of PMSM with instantaneous current control," *IEEE Trans. on Industry Applications*, vol. 50, no. 4, pp. 2614–2625, Jul. 2014.

[55] P. Chancharoensook and M. F. Rahman, "Dynamic modeling of a four-phase 8/6 switched reluctance motor using current and torque look-up tables," in *Proc. IEEE Industrial Electronics Society Conference*, Sevilla, Spain, Nov. 2002, pp. 491–496.

[56] C. S. Edrington, B. Fahimi, and M. Krishnamurthy, "An autocalibrating inductance model for switched reluctance motor drives," *IEEE Trans. on Industrial Electronics*, vol. 54, no. 4, pp. 2165–2173, Aug. 2007.

[57] M. Krishnamurthy, B. Fahimi, and C. S. Edrington, "On the measurement of mutual inductance for a switched reluctance machine," in *Proc. IEEE Power Electronics Specialists Conference*, Jeju, South Korea, Jun. 2006, pp. 1–7.

[58] X. Ding, M. Rashed, C. I. Hill, and S. Bozhko, "Analytical modelling approach for switched reluctance machines with deep saturation," in *Proc. International Conference on Electrical Systems for Aircraft, Railway, Ship Propulsion and Road Vehicles International Transportation Electrification Conference*, Toulouse, France, Nov. 2016, pp. 1–6.

[59] H. Gao, F. R. Salmasi, and M. Ehsani, "Inductance model-based sensorless control of the switched reluctance motor drive at low speed," *IEEE Trans. on Power Electronics*, vol. 19, no. 6, pp. 1568–1573, Nov. 2004.

[60] J. Mahdavi, G. Suresh, B. Fahimi, and M. Ehsani, "Dynamic modeling of non-linear SRM drive with Pspice," in *Proc. IEEE Industry Applications Conference*, New Orleans, LA, USA, Oct. 1997, pp. 661–667.

[61] B. Fahimi, G. Suresh, J. Mahdavi, and M. Ehsami, "A new approach to model switched reluctance motor drive application to dynamic performance prediction, control and design," in *Proc. IEEE Annual Power Electronics Specialists Conference*, Fukuoka, Japan, May 1998, pp. 2097–2102.

[62] F. R. Salmasi and M. Ehsani, "A novel approach to auto-calibrating sensorless switched reluctance motor drive," in *Proc. IEEE Industrial Electronics Society Conference*, Roanoke, VA, USA, Nov. 2003, pp. 2471–2476.

[63] X. Zhang, F. Wang, and X. Wu, "Low-speed direct-driven sensorless control including zero-speed for switched reluctance motor based on dynamic inductance model," in *Proc. IEEE International Conference on Electrical Machines and Systems*, Hangzhou, China, Oct. 2014, pp. 763–767.

[64] S. Kuai, V. Rallabandi, and D. M. Ionel, “Sensorless control of three phase switched reluctance motor drives using an approximate inductance model,” in *Proc. International Electric Machines and Drives Conference*, Miami, FL, USA, May 2017, pp. 1–6.

[65] A. Nirgude, M. Murali, N. Chaithanya, S. Kulkarni, V. B. Bhole, and S. R. Patel, “Nonlinear mathematical modeling and simulation of switched reluctance motor,” in *Proc. International Conference on Power Electronics, Drives and Energy Systems*, Trivandrum, India, Dec. 2016, pp. 1–6.

[66] C. S. Edrington and B. Fahimi, “An auto-calibrating model for an 8/6 switched reluctance motor drive: application to design and control,” in *Proc. IEEE Conference on Power Electronics Specialist*, Acapulco, Mexico, Jun. 2003, pp. 409–415.

[67] S. S. Ramamurthy, R. M. Schupbach, and J. C. Balda, “Artificial neural networks based models for the multiply excited switched reluctance motor,” in *Proc. Applied Power Electronics Conference and Exposition*, vol. 2, Anaheim, CA, USA, Mar. 2001, pp. 1109–1115.

[68] M. A. Preston and J. P. Lyons, “A switched reluctance motor model with mutual coupling and multi-phase excitation,” *IEEE Trans. on Magnetics*, vol. 27, no. 6, pp. 5423–5425, Nov. 1991.

[69] V. Vujicic and S. N. Vukosavic, “A simple nonlinear model of the switched reluctance motor,” *IEEE Trans. on Energy Conversion*, vol. 15, no. 4, pp. 395–400, Dec. 2000.

[70] D. S. Mihic, M. V. Terzic, and S. N. Vukosavic, “A new nonlinear analytical model of the SRM with included multiphase coupling,” *IEEE Trans. on Energy Conversion*, vol. 32, no. 4, pp. 1322–1334, Dec. 2017.

[71] H.-K. Bae, “Control of switched reluctance motors considering mutual inductance,” Ph.D. dissertation, Virginia Polytechnic Institute and State Universit, Blacksburg, USA, Aug. 2000.

[72] D. N. Essah and S. D. Sudhoff, “An improved analytical model for the switched reluctance motor,” *IEEE Trans. on Energy Conversion*, vol. 18, no. 3, pp. 349–356, Sept. 2003.

[73] M. Farshad, J. Faiz, and C. Lucas, “Development of analytical models of switched reluctance motor in two-phase excitation mode: extended miller model,” *IEEE Trans. on Magnetics*, vol. 41, no. 6, pp. 2145–2155, Jun. 2005.

[74] M. Boesing, M. Niessen, T. Lange, and R. D. Doncker, “Modeling spatial harmonics and switching frequencies in PM synchronous machines and their electromagnetic forces,” in *Proc. International Conference on Electrical Machines*, Marseille, France, Sept. 2012, pp. 3001–3007.

[75] J. Dong, B. Howey, B. Danen, J. Lin, J. W. Jiang, B. Bilgin, and A. Emadi, “Advanced dynamic modeling of three-phase mutually coupled switched reluctance machine,” *IEEE Trans. on Energy Conversion*, vol. 33, no. 1, pp. 146–154, Mar. 2018.

[76] J. D. Errico, “Understanding gridfit,” Accessed: Mar. 2016. [Online]. Available: http://www.mathworks.com/matlabcentral/fileexchange/8998.

[77] A. K. Jain and N. Mohan, "Dynamic modeling, experimental characterization, and verification for SRM operation with simultaneous two-phase excitation," *IEEE Trans. on Industrial Electronics*, vol. 53, no. 4, pp. 1238–1249, Jun. 2006.

[78] W. Uddin and Y. Sozer, "Modeling of mutually coupled switched reluctance motors for torque ripple minimization," in *Proc. International Electric Machines Drives Conference*, Coeur d'Alene, ID, USA, May 2015, pp. 1006–1010.

[79] M. Karacor, K. Yilmaz, and F. Erfan Kuyumcu, "Modeling MCSRM with artificial neural network," in *Proc. International Aegean Conference on Electrical Machines and Power Electronics*, Sept. 2007, pp. 849–852.

[80] S. Mehta, M. A. Kabir, I. Husain, and P. Pramod, "Modeling of mutually coupled switched reluctance motors based on net flux method," *IEEE Transactions on Industry Applications*, vol. 56, no. 3, pp. 2451–2461, 2020.

[81] W. Ding, D. Liang, and H. Sui, "Dynamic modeling and performance prediction for dual-channel switched reluctance machine considering mutual coupling," *IEEE Trans. on Magnetics*, vol. 46, no. 9, pp. 3652–3663, Sept. 2010.

[82] W. Ding, J. Lou, and L. Liu, "Improved decoupled model of mutually coupled dual-channel SRM with consideration of magnetic saturation in dual-channel operation," *IET Electric Power Applications*, vol. 7, no. 6, pp. 427–440, Jul. 2013.

[83] "JMAG-RT—JMAG: Simulation Technology for Electromechanical Design," Accessed: Jul. 6, 2019. [Online]. Available: https://www.jmag-international.com/products/jmag-rt/

[84] "Utilizing SABER with JMAG," Accessed: Jul. 6, 2019. [Online]. Available: https://powersys-solutions.com/2016/10/03/utilizing-saber-with-jmag/

[85] "Matlab: Third-Party Products & Services," Accessed: Jul. 6, 2019. [Online]. Available: https://www.mathworks.com/products/connections/product_detail/jmag/

[86] G. S. Buja and M. P. Kazmierkowski, "Direct torque control of PWM inverter-fed AC motors - a survey," *IEEE Trans. on Industrial Electronics*, vol. 51, no. 4, pp. 744–757, Aug. 2004.

[87] R. Krishnan, "Control Strategies for a Permanent Magnet Synchronous Machine," in *Permanent Magnet Synchronous and Brushless DC Motor Drives*, Boca Raton, Fl, USA: CRC, 2009.

[88] ——, "Permanent Magnets and Machines," in *Permanent Magnet Synchronous and Brushless DC Motor Drives*, Boca Raton, Fl, USA: CRC, 2009.

[89] G. Ellis, "Four types of controllers," in *Control System Design Guide*, Butterworth-Heinemann, 2012.

[90] J. Hwang and H. Wei, "The current harmonics elimination control strategy for six-leg three-phase permanent magnet synchronous motor drives," *IEEE Trans. on Power Electronics*, vol. 29, no. 6, pp. 3032–3040, Jun. 2014.

[91] C. Liu, F. Blaabjerg, W. Chen, and D. Xu, "Stator current harmonic control with resonant controller for doubly fed induction generator," *IEEE Trans. on Power Electronics*, vol. 27, no. 7, pp. 3207–3220, Jul. 2012.

[92] M. Liserre, R. Teodorescu, and F. Blaabjerg, "Multiple harmonics control for three-phase grid converter systems with the use of PI-RES current controller in a rotating frame," *IEEE Trans. on Power Electronics*, vol. 21, no. 3, pp. 836–841, May 2006.

[93] L. R. Limongi, R. Bojoi, G. Griva, and A. Tenconi, "Digital current-control schemes," *IEEE Industrial Electronics Magazine*, vol. 3, no. 1, pp. 20–31, Mar. 2009.

[94] R. L. de Araujo Ribeiro, C. C. de Azevedo, and R. M. de Sousa, "A robust adaptive control strategy of active power filters for power-factor correction, harmonic compensation, and balancing of nonlinear loads," *IEEE Trans. on Power Electronics*, vol. 27, no. 2, pp. 718–730, Feb. 2012.

[95] G. Escobar, A. M. Stankovic, and P. Mattavelli, "An adaptive controller in stationary reference frame for D-statcom in unbalanced operation," *IEEE Trans. on Industrial Electronics*, vol. 51, no. 2, pp. 401–409, Apr. 2004.

[96] A. Hamadi, S. Rahmani, and K. Al-Haddad, "A hybrid passive filter configuration for VAR control and harmonic compensation," *IEEE Transactions on Industrial Electronics*, vol. 57, no. 7, pp. 2419–2434, July 2010.

[97] R. Krishnan, "Dynamic Modeling of Permanent Magnet Synchronous Machines," in *Permanent Magnet Synchronous and Brushless DC Motor Drives*, Boca Raton, Fl, USA: CRC, 2009.

[98] Y. Kim, H.-T. Seo, S.-K. Kim, and K.-S. Kim, "A robust current controller for uncertain permanent magnet synchronous motors with a performance recovery

property for electric power steering applications," *Energies*, vol. 11, no. 5, p. 1224, 2018.

[99] S.-H. Kim, "Control of direct current motors," in *Electric Motor Control*, Amsterdam, The Netherlands: Elsevier, 2017.

[100] Y. Yang, H. Wen, and D. Li, "A fast and fixed switching frequency model predictive control with delay compensation for three-phase inverters," *IEEE Access*, vol. 5, pp. 17 904–17 913, 2017.

[101] R. Mikail, I. Husain, Y. Sozer, M. S. Islam, and T. Sebastian, "A fixed switching frequency predictive current control method for switched reluctance machines," *IEEE Transactions on Industry Applications*, vol. 50, no. 6, pp. 3717–3726, Nov 2014.

[102] Y. Wang, D. Ionel, D. G. Dorrell, and S. Stretz, "Establishing the power factor limitations for synchronous reluctance machines," *IEEE Transactions on Magnetics*, vol. 51, no. 11, pp. 1–4, Nov 2015.

[103] B. Bilgin, J. W. Jiang, and A. Emadi, "Electromagnetic principles in switched reluctance motors," in *Switched Reluctance Motor Drives: Fundamentals to Applications*, Boca Raton, FL, USA, CRC Press, 2019.

[104] ——, "Operational principles and modeling of switched reluctance machines," in *Switched Reluctance Motor Drives: Fundamentals to Applications*, Boca Raton, FL, USA, CRC Press, 2019.

[105] P. M. Azer, M. I. Marei, and A. A. Sattar, "A fault-tolerant strategy based on SMC for current-controlled converters," *International Journal of Electronics*, vol. 105, no. 5, pp. 817–835, 2018.

[106] M. Milosevic, "Hysteresis Current Control in Three-Phase Voltage Source Inverter," Accessed: May 15, 2020. [Online]. Available: http://citeseerx.ist.psu.edu/viewdoc/download?doi=10.1.1.567.3253&rep=rep1&type=pdf

[107] P. Azer, S. Ounie, and M. Narimani, "A new post-fault control method based on sinusoidal pulse width modulation technique for a neutral point clamped (NPC) inverter," in *2019 IEEE Applied Power Electronics Conference and Exposition (APEC)*, 2019, pp. 2499–2504.

[108] P. Azer, S. Ouni, and M. Narimani, "A new fault-tolerant method for 5-level active neutral point clamped inverter using sinusoidal PWM," in *2019 IEEE Energy Conversion Congress and Exposition (ECCE)*, 2019, pp. 2985–2990.

[109] ——, "A new fault-tolerant method for four-level neutral point clamped inverter based on sinusoidal PWM," in *2019 IEEE 28th International Symposium on Industrial Electronics (ISIE)*, 2019, pp. 2009–2014.

[110] ——, "A novel fault-tolerant technique for active-neutral-point-clamped inverter using carrier-based PWM," *IEEE Transactions on Industrial Electronics*, vol. 67, no. 3, pp. 1792–1803, 2020.